

University of Windsor

Scholarship at UWindor

Electronic Theses and Dissertations

Theses, Dissertations, and Major Papers

4-10-2017

Development of a Post-Processing Algorithm for Accurate Human Skull Profile Extraction via Ultrasonic Phased Arrays

Mariam Luay Y. Al-Ansary
University of Windsor

Follow this and additional works at: <https://scholar.uwindsor.ca/etd>

Recommended Citation

Al-Ansary, Mariam Luay Y., "Development of a Post-Processing Algorithm for Accurate Human Skull Profile Extraction via Ultrasonic Phased Arrays" (2017). *Electronic Theses and Dissertations*. 5925.
<https://scholar.uwindsor.ca/etd/5925>

This online database contains the full-text of PhD dissertations and Masters' theses of University of Windsor students from 1954 forward. These documents are made available for personal study and research purposes only, in accordance with the Canadian Copyright Act and the Creative Commons license—CC BY-NC-ND (Attribution, Non-Commercial, No Derivative Works). Under this license, works must always be attributed to the copyright holder (original author), cannot be used for any commercial purposes, and may not be altered. Any other use would require the permission of the copyright holder. Students may inquire about withdrawing their dissertation and/or thesis from this database. For additional inquiries, please contact the repository administrator via email (scholarship@uwindsor.ca) or by telephone at 519-253-3000ext. 3208.

Development of a Post-Processing Algorithm for Accurate Human Skull Profile Extraction via Ultrasonic Phased Arrays

By

Mariam Luay Y. Al-Ansary

A Thesis

Submitted to the Faculty of Graduate Studies
through the Department of Physics
in Partial Fulfillment of the Requirements for
the Degree of Masters of Science at the
University of Windsor

Windsor, Ontario, Canada

2017

©2017 Mariam Luay Y. Al-Ansary

**Development of a Post-Processing Algorithm for Accurate
Human Skull Profile Extraction via Ultrasonic Phased
Arrays**

By

Mariam Luay Y. Al-Ansary

Approved By:

M. Khalid, Outside Department Reader
Department of Electrical and Computer Engineering

W. Kedzierski, Department Reader
Department of Physics

E. Maeva, Advisor
Department of Physics

R. Maev, Advisor
Department of Physics

February 9th, 2017

Declaration of Originality

I hereby certify that I am the sole author of this thesis and that no part of this thesis has been published or submitted for publication.

I certify that, to the best of my knowledge, my thesis does not infringe upon anyone's copyright nor violate any proprietary rights and that any ideas, techniques, quotations, or any other material from the work of other people included in my thesis, published or otherwise, are fully acknowledged in accordance with the standard referencing practices. Furthermore, to the extent that I have included copyrighted material that surpasses the bounds of fair dealing within the meaning of the Canada Copyright Act, I certify that I have obtained a written permission from the copyright owner(s) to include such material(s) in my thesis and have included copies of such copyright clearances to my appendix.

I declare that this is a true copy of my thesis, including any final revisions, as approved by my thesis committee and the Graduate Studies office, and that this thesis has not been submitted for a higher degree to any other University or Institution.

Abstract

Ultrasound Imaging has been favored by clinicians for its safety, affordability, accessibility, and speed compared to other imaging modalities. However, the trade-offs to these benefits are a relatively lower image quality and interpretability, which can be addressed by, for example, post-processing methods. One particularly difficult imaging case is associated with the presence of a barrier, such as a human skull, with significantly different acoustical properties than the brain tissue as the target medium. Some methods were proposed in the literature to account for this structure if the skull's geometry is known. Measuring the skull's geometry is therefore an important task that requires attention. In this work, a new edge detection method for accurate human skull profile extraction via post-processing of ultrasonic A-Scans is introduced. This method, referred to as the Selective Echo Extraction algorithm, SEE, processes each A-Scan separately and determines the outermost and innermost boundaries of the skull by means of adaptive filtering. The method can also be used to determine the average attenuation coefficient of the skull. When applied to simulated B-Mode images of the skull profile, promising results were obtained. The profiles obtained from the proposed process in simulations were found to be within $0.15\lambda \pm 0.11\lambda$ or $0.09 \pm 0.07mm$ from the actual profiles. Experiments were also performed to test SEE on skull mimicking phantoms with major acoustical properties similar to those of the actual human skull. With experimental data, the profiles obtained with the proposed process were within $0.32\lambda \pm 0.25\lambda$ or $0.19 \pm 0.15mm$ from the actual profile.

I dedicate my thesis to my loving family.

Acknowledgments

First and foremost, I would like to thank my parents for always putting my interests before theirs. They are the ones who instilled in me the much needed human values, which schools or the academia were not necessary able to teach me. Their sacrifices - through life - for my siblings and I were inspiring. They taught me that happiness stems from selfless acts. I hope my achievements will make their sacrifices worthwhile.

To my advisors Dr. Elena Maeva and Dr. Roman Maev, thank you for believing in my academic abilities and providing me with the tools and wisdom to excel in my academic life. You have continuously encouraged my progress with your insightful advises, kind words, and sweet smiles.

To my exceptional mentor Dr. Kiyanoosh Shapoori, thank you for your guidance, patience, support, and motivation. You gave me your undivided attention and made yourself available during the busiest days to help with my research while allowing it to be my work. Without your guidance and positive attitude, I would not have been able to stay focused and reach my full potential. Having had you as a mentor throughout my undergraduate and masters research, I am ever so grateful, and I believe that one day you will be a distinguished advisor for very lucky students.

I would like to thank my colleagues Dr. Jeff Sadler, Dr. Eugene Malyarenko, and Master of Science Andrew Ouellette, who have given me their valuable advises on various aspects during my research. I would also like to thank members of the department, especially Dr. Steve Rehse and Mrs. Kimberly Lefebvre, for having an open door and attentive ears to help me with their insights in academia and in life. I would like to extend my gratitude to members of my committee, Dr. Wladyslaw Kedzierski and Dr. Mohammed Khalid for putting in the time and effort to evaluate my work.

To my wonderful aunt Iman, thank you for caring about me and for being an amazing role model. You have shown me that the sky is the limit and that I can do whatever I want if I set my mind to it. You have encouraged me to be myself and I can say without doubt, that without you I wouldn't be where I am today. Thank you Amma.

To my siblings, Laith, Abdulrahman, and Asmaa, and my sisters-in-law Eman and Fatima you have all been so supportive throughout my research to finish my masters. You paid attention to my research ideas when it did not make sense and listened to my complaints with an open heart. Your support and love made my life as graduate student much easier. Not to mention, thank you for making feel wise when using me as your physics reference.

Last but not least, my dearest Sara, there are no words to describe how thankful I am to you. You are my rock and the fresh breeze in the midst of distress. You are the person I look for when I am happy, excited, angry, or sad. You have seen me through my toughest days, shared with me my happiest moments, and was there for everything in between. Seeing your smile makes my struggles bearable. I love growing and sharing milestones with you. Thank you for being my friend.

Table of Contents

Declaration of Originality	iii
Abstract	iv
Dedication	v
Acknowledgments	vi
List of Tables	x
List of Figures	xi
List of Abbreviations	xiv
List of Symbols	xv
1 Introduction: an overview of medical imaging modalities	1
1.1 X-Ray Imaging and X-Ray Computer Tomography	2
1.2 Positron Emission Tomography	3
1.3 γ -Ray Computer Tomography	4
1.4 Magnetic Resonance Imaging	5
1.5 Ultrasonic Imaging	5
1.5.1 Transcranial ultrasonic imaging	7
1.6 Purpose statement and thesis organization	8
2 Ultrasonic imaging and post-processing: a review	10
2.1 Ultrasonic phased arrays	11
2.2 The convolution model	13
2.2.1 PSF estimation via statistical modeling: the ARMA Process	15
2.2.2 Homomorphic estimation of PSF: the Cepstrum Model . . .	16

2.2.3	Adaptive filtering tool and its application for non-blind deconvolution	18
2.2.4	Blind-deconvolution via Single Input Multiple Output Model (SIMO)	20
2.2.5	Blind-deconvolution via Inverse Filtering	21
2.3	Conclusion: post-processing methods' compatibility for ultrasonic skull imaging	23
3	Theory and simulations	25
3.1	The Selective Echo Extraction algorithm	26
3.1.1	Simulation of SEE for single A-Scans	38
3.2	Applying SEE to determine the curvature of the skull from simulated B-Scans	46
3.3	Using SEE to determine the attenuation coefficient of the skull. . .	56
3.4	Conclusion	60
4	Experiments and results	63
4.1	Experimental setup	64
4.1.1	The human skull mimicking phantoms	64
4.1.2	The IMASONIC array transducer	67
4.1.3	The data acquisition system	67
4.2	Experimental Data and Results	68
4.3	Discussion	78
5	Conclusion	81
	Bibliography	86
	Vita Auctoris	94

List of Tables

3.1	Accuracy of detection method with SEE vs with SEE and curve fitting	55
4.1	Properties of phantom bone materials	66
4.2	Properties of the phantoms	67
4.3	Accuracy of detection method with SEE vs with SEE and curve fitting using experimental data	79

List of Figures

1.1	A typical X-Ray radiographic geometry [1]	2
1.2	PET scan event detection. [1]	3
1.3	Flat Bone Anatomy in the skull [2]	6
2.1	Conventional Beamforming Illustration	12
2.2	Determining PSF using Cepstrum Domain	16
2.3	Basic Adaptive Filter for System Identification[3]	19
3.1	Geometry defining the coordinate system for the Fraunhofer ap- proximation for a rectangular transducer.[4]	31
3.2	One transducer element used to image a simple two media sample. .	32
3.3	Cross-Correlation example for a hypothetical simple case of A-Scans with a Gaussian PSF	36
3.4	Cross-Correlation example for a hypothetical complex case of A- Scans constructed with a Gaussian PSF and added uniformly dis- tributed random error	37
3.5	The point spread function in 3.5a convoluted with the reflectivity function in 3.5b produce the A-Scan shown in 3.5c.	39
3.6	Processing an A-Scan with no added noise.	40
3.7	Processing a noisy A-Scan with additive Gaussian noise correspond- ing to $12dB/sample$ SNR in the A-Scan.	41
3.8	Processing a noisy A-Scan with additive Gaussian noise correspond- ing to $6dB/sample$ SNR in the A-Scan.	42
3.9	Processing a noisy A-Scan with convoluted Gaussian noise corre- sponding to $12dB/sample$ SNR in the reflectivity function.	43
3.10	Processing a noisy A-Scan with convoluted Gaussian noise corre- sponding to $12dB/sample$ SNR in the reflectivity function.	44

3.11	Processing a noisy A-Scan with convoluted Gaussian noise corresponding to $12dB/sample$ SNR in the reflectivity function and additive Gaussian noise corresponding to $12dB/sample$ SNR in the A-Scan.	45
3.12	Noiseless B-Scan of a skull geometry.	47
3.13	Processing a noisy B-Scan with Additive Gaussian noise corresponding to $12dB/sample$ SNR in each A-Scan.	48
3.14	Processing a noisy B-Scan with Additive Gaussian noise corresponding to $6dB/sample$ SNR in each A-Scan.	51
3.15	Processing a noisy B-Scan with convoluted Gaussian noise corresponding to $12dB/sample$ SNR in each reflectivity function.	52
3.16	Processing a noisy B-Scan with convoluted Gaussian noise corresponding to $6dB/sample$ SNR in each reflectivity function.	53
3.17	Processing a noisy B-Scan with convoluted Gaussian noise corresponding to $12dB/sample$ SNR in each reflectivity function and added Gaussian noise resulting to $12dB/sample$ SNR in each A-Scan.	54
3.18	Testing Algorithm 2 for different types of B-Scans to determine the optimal attenuation coefficient value. In each sub figure, the y axis represents the effectiveness E as discussed in equations 3.33 and the x axis represents attenuation coefficient	59
4.1	Experimental Setup showing OmniScan acquisition system, 64 element 5MHz IMASONIC linear phased array, delay line, and a skull phantom	64
4.2	Skull Phantom Curvatures.	65
4.3	3-D Skull Phantom structure.	65
4.4	Human Skull mimicking phantoms	66
4.5	The raw B-Scans acquired from the acquisition system	69

4.6	The Effectivity factor of SEE with respect to varying attenuation coefficient values acquired from raw B-Scans. The dashed box represents the actual attenuation coefficient value range for the specific phantom	72
4.7	Attenuation coefficient value for each skull sample	74
4.8	The analyzed Effectivity factor of SEE with respect to varying attenuation coefficient values acquired from raw B-Scans. The dashed box represents the actual attenuation coefficient value range for the specific phantom	75
4.9	The processed B-Scans using SEE and the custom curve fitting algorithm	76

List of Abbreviations

A-Scan	Amplitude Scan
ARMA	AutoRegressive Moving Average
B-Scan	Brightness Scan
γ -Ray CT	γ -Ray Computer Tomography
i.i.d	Independent and Identically Distributed
MRI	Magnetic Resonance Imaging
PET	Positron Emission Tomography
PSF	Point Spread Function
RF	Radio-Frequency
SEE	Selective Echo Extraction
SIMO	Single Input Multiple Output
X-Ray CT	X-Ray Computer Tomography

List of Symbols

α	Attenuation Coefficient [$\frac{dB}{cm}$]
c	Speed of sound [$\frac{m}{s}$]
d	Pitch of the transducer [mm]
$h(n)$	Tissue Response Function in time domain [Pa]
$h_b(n)$	Reflectivity function of the skull's innermost and outermost boundaries in time domain [Pa]
$h_d(n)$	Reflectivity function of diploe in time domain [Pa]
$h_\eta(n)$	Noise in the reflectivity function of the skull's in time domain [Pa]
λ	The wavelength of the pressure wave in the target medium [m]
$\eta(n)$	Additive Gaussian Noise in time domain [Pa]
ω	Angular frequency [$\frac{rad}{s}$]
p	Pressure [Pa]
ρ	Density [$\frac{Kg}{m^3}$]
σ_ω	Pulse width of the excitation signal at frequency ω [s]
$x(n)$	Point Spread Function in time domain [Pa]
$y(n)$	Radio-Frequency line in time domain [Pa]
Z	Acoustic impedance [$MRayl$]

Chapter 1

Introduction: an overview of medical imaging modalities

Non-invasive medical imaging is a necessity of modern medicine as most diseases are diagnosed through different medical imaging equipment. In the last century, many types of medical imaging devices have emerged, ranging in complexity, cost, size, and image quality. The most common medical imaging techniques used nowadays are X-Ray, X-Ray Computer Tomography (X-Ray CT), Positron Emission Tomography (PET), γ -Ray Computer Tomography (γ -Ray CT), Magnetic Resonance Imaging (MRI), and Ultrasonography. Each of these techniques offers advantages that give it a preference depending on the condition.

All of the above non-invasive medical imaging modalities rely on observing wave disturbances that have been sent into the body and have interacted with the internal anatomy[1]. Those wave disturbances can be of electromagnetic nature as in X-Ray, γ -Ray, and MRI, or of high frequency acoustic nature as in Ultrasonography. In all cases, the wave disturbances are created artificially with distinct characteristics such as frequency, intensity, and polarization. While passing through

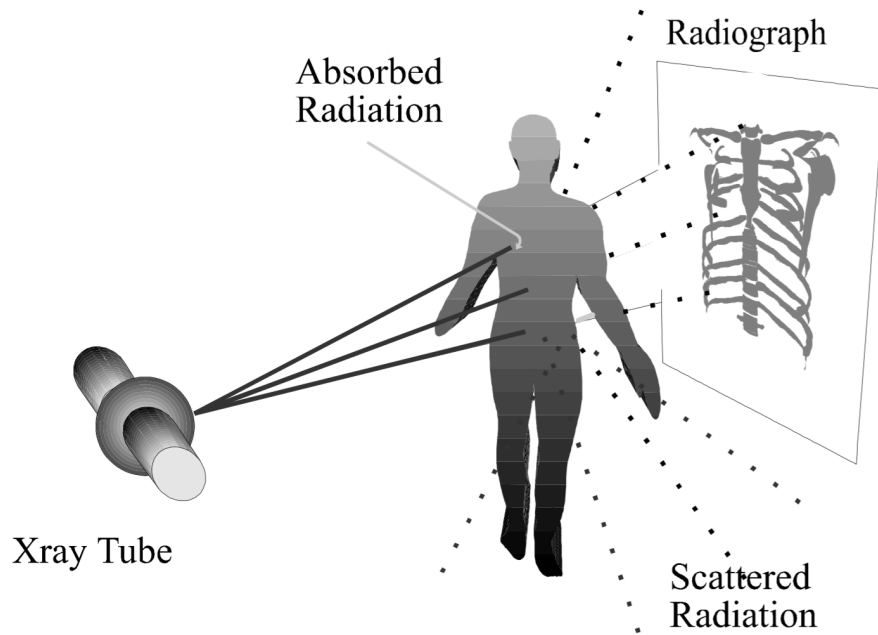


FIGURE 1.1: A typical X-Ray radiographic geometry [1]

the body, the waves change in nature or intensity and are observed and decoded outside the body to determine physical properties of the internal anatomy.

1.1 X-Ray Imaging and X-Ray Computer Tomography

X-Ray was first used in 1896, making it the first medical imaging technique to be developed[5]. X-Ray Images are obtained by firing X-Ray photons into the body, and observing the photons that have not been absorbed or scattered by the different types of tissue it passes through, as shown in Figure 1.1. The value of X-Ray absorption coefficient varies depending on the type of tissue. At each cross-section of the body, different types of tissue absorb varying amounts of the rays, creating a shadow: the X-Ray image is an overlap of those shadows. This is considered a limitation of X-Ray as it does not provide enough information

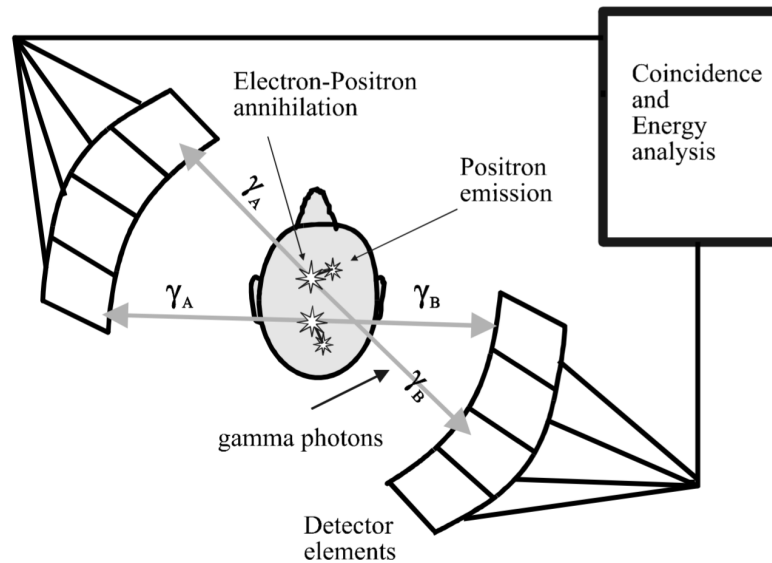


FIGURE 1.2: PET scan event detection. [1]

to diagnose illnesses. Moreover, although X-Ray provides appropriate contrast between bone tissue and soft tissue, it fails to provide contrast between different types of soft tissues. These limitations were improved upon after the development of X-Ray CT scan, which acquires X-Ray images at different angles of the body. By using computer generated tomography, a three dimensional description of the body can be acquired, increasing the diagnostic information dramatically. The drawback of this method stems from the fact that each X-Ray CT scans requires an average of 200 X-Ray scans. This results in a large dosage of radiation being absorbed by the body after the procedure.

1.2 Positron Emission Tomography

Similar to X-Ray CT, Positron Emission Tomography relies on sending a positron beam towards the body and projecting the after effects on a detector. The positron beam is able to travel for approximately 5 mm before annihilation occurs, at that point, two γ -Rays are produced and travel in opposite directions, as shown in

Figure 1.2. By detecting the γ -Rays, the event location can be pin-pointed. After a sufficient number of events are collected, a series of projections are combined to produce 2D images of isotope concentrations. PET scan is able to produce clear images of the target organ as the number of events occurring in a region can be used to identify the type of tissue. However, PET equipment is rather large and a working cyclotron has to be available to produce the required short-lived positron emitting radionuclide. In addition, when annihilation occurs between an electron and a positron, a substantial amount of ionizing energy is released into the surrounding tissue, which is harmful to the body.

1.3 γ -Ray Computer Tomography

Another γ -Ray utilized medical imaging technique relies on the idea of using molecules that are known to interact with the target tissue to create an image of it. For example, iodine is highly reactive in the thyroid gland and not reactive in other areas of the body. Other molecules, such as glucose, are important for the function of tissue and can be used to identify metabolic processes. γ -Ray CT is based on injecting patients with radio-active labeled compounds and observing the movement of those compounds as they pass through the blood stream. The radio-active labeled compounds continue to release γ -Rays as they travel through the body without affecting the interaction of the compounds they are attached to. In the case of radioactive labeled iodine, the molecules will be localized in the thyroid gland. This movement or location detection is done by obtaining images from a γ -Ray camera at different angular positions, similar to X-Ray CT. This process produces tomographic images of the organ where the compounds are being utilized. Limitations of γ -Ray CT include the inability to inject patients with a substantial dose of radio-active labeled compounds, which limits the image quality. Gamma-Ray CT, like X-Ray CT, and PET, produces ionizing radiation, which is

not free of health risks. Long or frequent exposure to ionizing radiation may cause cellular damage or cancerous cellular mutations.

1.4 Magnetic Resonance Imaging

Unlike X-Ray, γ -Ray, and PET, which comes at the cost of radiation exposure, Magnetic Resonance Imaging (MRI) relies on no ionizing radiation and provides clear images. MRI uses three parameters for observation: the ‘free water density’, longitudinal relaxation time, T_1 , and transverse relaxation time, T_2 . The water proton resonance allows for observation of fluid flow and tissue magnetic susceptibility. Nuclear magnetic resonance technique can be expanded to observe other nuclei when necessary for diagnostics. Thus, MRI provides more information than other techniques with no association to health risks. Although MRI provides high contrast between different types of soft tissue, the equipment is usually over-sized and the process is slow and expensive. For these reasons, MRI is only available in large hospitals and is used to diagnose specific conditions.

1.5 Ultrasonic Imaging

Unlike all other medical imaging techniques, Ultrasonography is arguably the safest, most affordable, and most portable method. Although these benefits come at a trade off of image quality, Ultrasonography still remains a favorite for physicians. Most commonly, Ultrasound imaging systems rely on sending acoustic waves through the body and observing reflections off each boundary between different types of tissue. Ultrasound provides an effective contrast between different types of tissue if uninterrupted by bone.

When bone tissue is present, the significant difference in acoustical properties between bone tissue and soft tissue causes high reflections, phase aberration, and

absorption at those boundaries, thereby limiting the quality of images beyond the bone. Regardless of this physical phenomenon, researchers have been encouraged to improve imaging through bone. If an ultrasonic device is capable of scanning the brain through the skull is introduced to the medical community, it will have the potential benefits of affordability, safety, and portability that other imaging devices lack.

For over four decades, researchers have sought to develop ultrasonic trans-skull imaging in order to upgrade conventional imaging. To be able to image through the skull, it is important to understand the skull's anatomy.

There are four classification of bones: long bone, short bone, flat bone, and Irregular bone[2, 6]. Long bones are rod shaped and, as the name suggests, are longer in one direction than the other two. They are primarily present in limbs. Short bones are also rod shaped; however, their length is about the same as their width and they can be found in the wrist and ankle. Flat bones, unlike the other classifications, extend in two dimensions, such as in the skull, shoulders, and ribs.

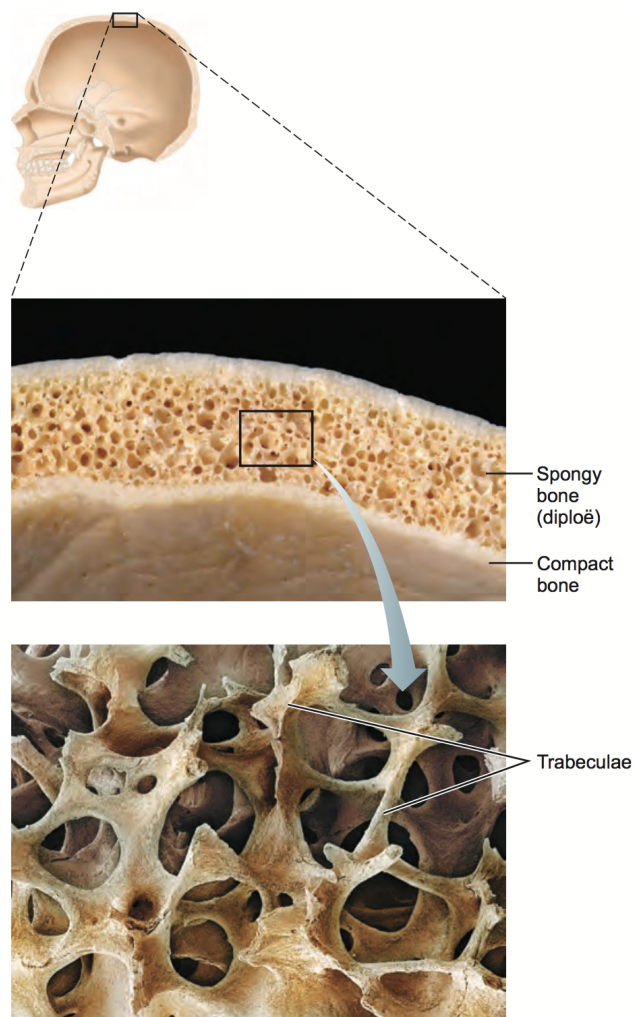


FIGURE 1.3: Flat Bone Anatomy in the skull [2]

Finally, the irregular bone, includes any bones that do not fit in other descriptions such as hip bone.

Skull bone belongs to the flat bone type and consists of three major layers, as shown in figure 1.3. The name “Flat bone” is only meant to imply the extension of this type of bone in two dimensions and it does not necessarily mean any of the layers are flat. In the skull, flat bone is curved with a large radius that gives it the spherical shape, while small curvatures exist in the inner/outer compact layer and the spongy (diploe) layer.

Unlike the outer compact bone layer, which is relatively smooth, the inner compact bone layer is rough and curvy. It is responsible for refraction and phase aberrations in trans-skull imaging. The diploe layer, however, is responsible for other distortions, such as scattering and attenuation. The diploe layer is a network of bone fragments that are aligned to support the stress points in the skull. Since those fragments are small, they can only be observed at high frequencies in ultrasonic imaging ($> 10\text{MHz}$). For the purpose of imaging the brain through the skull, though, using high frequency is not recommended. At high frequencies, the diploe layer is more attenuative and since the wavelength of the transmitted field become comparable in size to the fragments in the diploe layer, non-negligible scattering effects are present. To avoid this, trans-skull imaging is generally limited to a central frequency of no more than 5MHz .

1.5.1 Transcranial ultrasonic imaging

Ultrasonic imaging techniques that are created for trans-skull imaging have been suggested since the 1960s [7–9]. Since then, many types of approaches have been proposed. Some methods limit imaging to the temporal window, at which there is no diploe layer and the skull is the flattest [10–13]. Some suggest imaging using shear mode [14, 15], where better axial target localization is provided at the cost

of inferior lateral resolution. Others focus through the skull using time-reversal technique[16–19]. Although time-reversal has been very successful at imaging the brain, it requires a hemispherical transducer array surrounding the entire head which can be difficult to manage. The most success has been achieved using adaptive beamforming technique [20–26] which uses a small hand held ultrasonic transducer for imaging. The time-reversal and adaptive beamforming technique show the most promising results. Thus, perfecting this method gives physicians the freedom to expand imaging to areas other than the temporal window, acquire higher quality images than using shear mode, for instance, all with a small hand held device. However, for adaptive beamforming to work, an accurate skull profile has to be available as an inaccuracy of $0.1mm$ could result in imaging error of up to $1mm$ in $12cm$ depth [27].

In order to account for the skull curvature using adaptive beamforming, it is necessary to have an accurate measurement of the skull geometry, especially the curvature of the inner compact bone. The presence of curvature in thick diploe bone also distorts the image and makes it impossible to observe the curvature of the inner compact bone with minimal processing and, as a result, failing to image the brain. Having an accurate measurement of the skull geometry can dramatically enhance the quality of brain imaging of the brain via ultrasonography.

1.6 Purpose statement and thesis organization

The purpose of this thesis is to develop a signal processing technique applied to acoustic signals to accurately extract the curvature of the skull's inner compact bone boundary such that it lies within $\pm 0.5mm$ of the actual value. The method can also be used to determine the averaged attenuation coefficient of the skull.

The method is applied to six types of skull phantoms with varying diploe layer thickness and curvatures. In general, the proposed technique is comprised of three

major steps. In the first step, the method is used to determine the attenuation coefficient of the skull. This value as well as the raw data are input into the developed Selective Echo Extraction (SEE) signal processing technique, to produce two reflections that show the skin/skull boundary and the skull/brain boundary. The results are then curve fitted to show a smooth curvature representing the inner compact bone boundary.

The thesis is divided into five chapters. Chapter 2 presents a complete literature review and explains the necessity of a reliable method for human skull profile extraction. Chapter 3 shows the Selective Echo Extraction signal processing algorithm, the simulation processes, the curve fitting process, and the attenuation coefficient determining algorithm. Chapter 4 illustrates the experimental setup, optimization of it, and results from the acquired experimental data. Chapter 5 discusses the conclusion.

Chapter 2

Ultrasonic imaging and post-processing: a review

Medical Ultrasonography is one of the leading non-invasive diagnostic imaging techniques. The cost-benefit ratio of Ultrasonic Imaging far exceeds other imaging techniques in terms of affordability, accessibility, safety, and promptness. However, the low spatial resolution has been one of the major limitations of ultrasonic imaging and cannot compete with the quality of other modalities, such as X-Ray CT, γ -Ray CT, or MRI. Low resolution is mainly caused by the finite bandwidth of the imaging transducer or the non-negligible width and duration of ultrasonic pulses [28]. As the demand of ultrasonography increased over the last few decades, efforts have been made to improve the quality of the hardware in ultrasonic devices and incorporate effective digital signal processing techniques in post-processing.

In this chapter, Section 2.1 briefly introduces Ultrasonic Phased Arrays. Section 2.2 explains signal post-processing techniques with an overview of the most commonly used post-processing methods to enhance ultrasonic scans. Finally, Section 2.3 discusses the applicability of those post-processing methods to the case of skull imaging, and explains the motivation for this study and the proposed method.

2.1 Ultrasonic phased arrays

Ultrasonic Imaging relies on sending an acoustic wave into a target system and observing the reflections that occur at each boundary between the different media in the system. Those reflections are collected to produce an Amplitude Scan (A-Scan), Brightness Scan (B-Scan), and other types of scans. A-Scans show the amplitude of the reflections as a function of time. When the amplitude is high, a boundary is postulated to exist at a distance $d = \frac{1}{2}v\tau$, where v is the velocity of sound wave in the medium and τ is the time at which the reflection occurs. A B-Scan is obtained by collecting a number of A-Scans at different transducer element displacements. The B-Scan is displayed as a brightness map that is produced by converting the amplitude at points in time of each A-Scan to brightness such that a two dimensional image is constructed.

It is the convention in ultrasonic imaging to focus the transducer into a specific point or depth in the target medium in order to receive high reflections, and therefore, a high contrast image. This can be done by varying the geometry of the transducer or by using an Ultrasonic Phased Array.

An Ultrasonic Phased Array is a collection of elements that can be driven individually to form an acoustic field [29]. Elements arranged in a 1-D array can be driven to focus or steer the acoustic field in the two dimensional plane perpendicular to the array. Focusing the acoustic field into a singular point can be done by exciting the elements with different time delays to account for the path differences to the focal point between each element and the center of the array. By doing this, the waves sent from every element in the array interfere constructively at the focal point. Figure 2.1 shows a one dimensional array that is focused at the focal point shown. The elements are excited with a delay parameter according to the following equation:

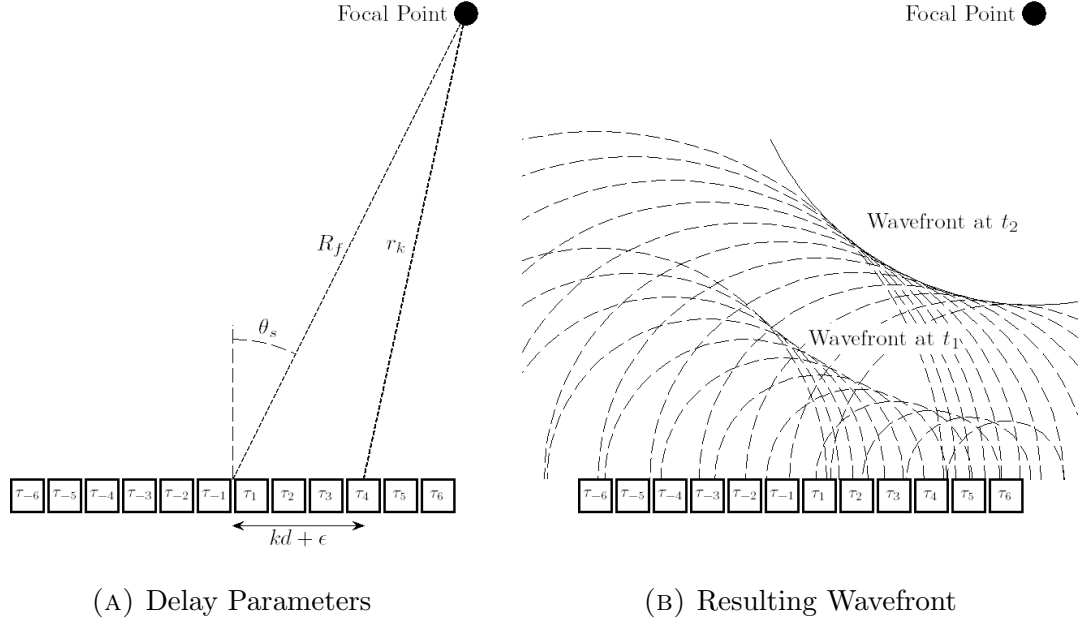


FIGURE 2.1: Conventional Beamforming Illustration

$$\tau_k = \frac{\sqrt{R_f^2 + (kd + \epsilon)^2 - 2R_f kd \sin(\theta_s)} - R_f}{c} \quad (2.1)$$

where τ_k is the time delay applied to the k^{th} element, R_f is the distance between the focal point and the center of the array as shown in Figure 2.1a, d is the pitch between the elements, θ_s is the angle between the normal to the array plane and the focal point as shown in Figure 2.1a, and c is the speed of sound in the target media.

Figure 2.1b shows the wavefront at times t_1 and t_2 after all elements have been excited, where $t_1 < t_2$. It is clear that the waves from all elements will intersect at a later time at the focal point.

Such time delay scenario can be generalized to focus a 2-D array in a 3-D volume and produce a three dimensional tomographic image of the target object.

Once the beam is focused onto a point in space, the energy of the constructively interfered waves is high enough that a noticeable reflection can be observed if a boundary is present. To image a volume, the ultrasonic array is focused at several points in the target media, and the reflections are collected to compose a 2-D image or a volume tomography.

In many cases this image needs further processing to clarify it in order for a physician to make a diagnosis. This process is referred to as post-processing and has been tackled since the advent of ultrasonic imaging.

2.2 The convolution model

One of the major advancements in the field of post-processing in medical ultrasonography is the introduction of a convolution model from the standard wave equation using the first-order Born approximation [30–36].

The convolution model states that the acquired B-Scan, which contains many Radio-Frequency lines (RF-lines), $y(n)$ can be displayed as:

$$y(n) = x(n) * h(n) + \eta(n) \quad (2.2)$$

where $x(n)$ is the Point Spread Function (PSF) that is produced by the transducer, $h(n)$ is the tissue response function representing the reflections at each boundary, and $\eta(n)$ is any additive white noise present in the system. In many cases, $\eta(n) \approx 0$ and the noise in the system is convoluted noise present in $h(n)$.

This model has been revolutionary in the field of ultrasonic digital signal processing as solving for $h(n)$ with the least amount of error results in a clear image of the target organ. It is important to note that the convolution model is a generalized expression that cannot simply be solved using conventional deconvolution.

The Point Spread function cannot be assumed to be the original transmitted signal. In ultrasonic imaging, the PSF exhibits a spatial dependency due to the non-uniformity of focusing, diffraction effects, dispersive attenuation, and phase aberrations [37–40]. Thus, the PSF has to be estimated in each B-scan in order to acquire the tissue response function. In fact, in some cases PSF has to be estimated in each section of the B-scan to accommodate for the spatial dependency it exhibits.

The generalized convolution model also assumes a linear relation between the acoustic field and the targeted biological tissue, which is not true as the linear relation can only occur on conditions of weak scattering [41].

Even in the presence of the limitations to the Convolution Model mentioned above, it can still provide a relatively accurate estimation. In order to solve for $h(n)$, advanced digital signal processing techniques have to be applied instead of applying conventional deconvolution.

Because of the nature of PSF in ultrasonography, the most effective way to extract the tissue response function in post-processing is through blind-deconvolution [42]. Blind deconvolution can be achieved by either estimating the PSF first then applying non-blind deconvolution[43], or by directly finding the tissue response function.

In upcoming sections, the most commonly used post-processing techniques in ultrasonography are introduced. Section 2.2.1 and 2.2.2 follow the approach that relies on finding an accurate estimation of the PSF, then applying non-blind deconvolution. Section 2.2.3 explains the adaptive filtering tool, which many non-blind and blind deconvolution methods use. Finally, Sections 2.2.4 and 2.2.5 show two blind methods that rely on finding $h(n)$ directly or simultaneously with $x(n)$.

2.2.1 PSF estimation via statistical modeling: the ARMA Process

The convolution model can be solved by means of system identification [44, 45]. More specifically, PSF can be estimated statistically through the autoregressive moving average (ARMA) model [46, 47]. This approach considers the PSF $x(n)$ to be the impulse response of a linear time-invariant system that is defined by the generic difference equation as follows:

$$y(n) = \sum_{k=1}^p a(k)y(n-k) + \sum_{k=0}^q b(k)h(n-k) \quad (2.3)$$

In the context of the theory of system identification, equation 2.3 is known as the ARMA model. This method is a generalization of autoregressive (AR) and moving average (MA) models. AR is obtained by setting $q = 0$, and MA by setting $p = 0$.

Using the ARMA model in ultrasonography means that the PSF can be calculated by estimating the ARMA parameters $\{a(k)\}_{k=1}^p$ and $\{b(k)\}_{k=0}^q$. After those parameters are estimated, the tissue response function can be found by means of non-blind deconvolution.

Since the z-transform $X(z) \equiv \sum_{n=0}^{\infty} x(n)z^{-n}$ of $x(n)$ is given by:

$$X(z) = \frac{B(z)}{A(z)} = \frac{1 + \sum_{k=0}^q b(k)z^{-k}}{1 + \sum_{k=0}^p a(k)z^{-k}} \quad (2.4)$$

Estimating ARMA parameters can be done through maximum likelihood estimation [45]. When the number of data points is relatively small, as is the case in ultrasonography, this method proves inefficient. Other solutions that have been proposed suggest minimizing the sum of squares of the one-step-forward prediction error within the sampling range. The estimates are referred to as the Least square Estimates [48].

It is important to note that although the ARMA process proves successful in many cases in ultrasonic application, it assumes that the system is time-invariant. This leads ARMA model to be susceptible to noise, and so it is important to either filter the noise beforehand or restrict the use of the ARMA model to non-noisy data.

2.2.2 Homomorphic estimation of PSF: the Cepstrum Model

The most common way to find PSF is using Homomorphic signal processing [49], or more specifically, the cepstrum based methods for estimating PSF [35, 38, 46, 50–52].

The method applies a Non-linear mapping to the cepstrum domain in which a linear filter (referred to as a lifter) is applied and then a non-linear mapping is applied to return the signal to the original domain.

The cepstrum model, unlike the ARMA model, is a non-parametric model that is used to extract PSF from RF-line or B-scan. The procedure is shown in Figure 2.2.

Consider the convolution model stated in equation 2.2 in the Fourier Domain:

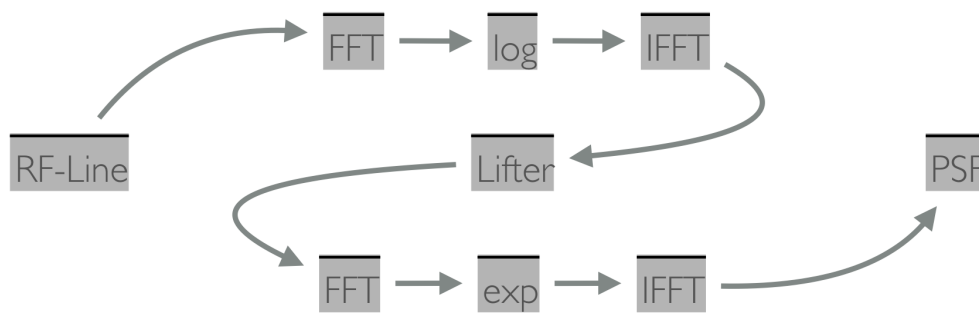


FIGURE 2.2: Determining PSF using Cepstrum Domain

$$Y(f) = X(f) \cdot H(f) \tag{2.5}$$

where upper case denotes their lower case counterparts after applying a Discrete Fourier Transform[43]. In this case the pulse spectrum is convoluted with the reflection spectrum. In order to separate the two, the logarithm is taken:

$$\begin{aligned} \log(Y(f)) &= \log(X(f) \cdot H(f)) \\ &= \log(X(f)) + \log(H(f)) \\ &= \log|X(f)| + j\arg(X(f)) + \log|H(f)| + j\arg(H(f)) \end{aligned}$$

In some simple cases, minimum phase can be assumed in $X(f)$ and in $H(f)$, and so, only the amplitude of those spectra are taken into consideration when performing the following operations. This type of cepstrum analysis is referred to as real cepstrum [50]. However, in ultrasonography, phase cannot be avoided due to the non-negligible effects it has on the signal[35]; this is referred to as complex cepstrum. To convert to the cepstrum domain, one must apply an inverse fourier transform to the logarithm of the Fourier transform of the RF-line:

$$\begin{aligned} \mathcal{IFFT}(\log(Y(f))) &= \mathcal{IFFT}(\log|X(f)| + j\arg(X(f)) + \log|H(f)| + j\arg(H(f))) \\ &= \mathcal{IFFT}(\log|X(f)|) + \mathcal{IFFT}(j\arg(X(f))) + \mathcal{IFFT}(\log|H(f)|) \\ &\quad + \mathcal{IFFT}(j\arg(H(f))) \end{aligned}$$

or

$$y_c(n) = x_c(n) + x_{c,arg}(n) + h_c(n) + h_{c,arg}(n) \tag{2.6}$$

where the subscript c refers to the mapping of each of the variable in the spectrum domain to the cepstrum domain. Moreover, the subscript c, arg represents the phase contribution.

In the cepstrum domain, the PSF spectrum and the response function spectrum are added instead of being convoluted. Thus, since the nature of the cepstrum leaves the components of $x_c(n)$ at the lower portion of the cepstrum and the components of $h_c(n)$ scattered across the sample, a simple low-pass lifter can be applied to extract the signal $x_c(n)$ and its phase $x_{c,arg}(n)$.

Since a B-scan has multiple RF-lines, it is recommended to average all of the results acquired after applying the lifter and before performing the mapping back to the spectrum domain.

The conversion to the spectrum domain can be done by taking the Fourier transform, applying the natural exponential, and taking the inverse Fourier transform.

Once PSF is acquired, deconvolution can be applied to reconstruct $h(n)$. At that point, the image is restored to a high quality. Deconvolution approaches that can be used are ones acquired from a stable model, such as Lucy-Richardson deconvolution and Weiner deconvolution.

2.2.3 Adaptive filtering tool and its application for non-blind deconvolution

Adaptive filtering is a signal processing tool designed to converge on a solution for an Unknown System given an input and the Desired Response as shown in Figure 2.3[3]. This tool relays on minimizing a cost function $e(n)$, which is defined as the deference between the System Output and the “guessed” Network Response. When $e(n)$ is minimized, the Unknown System is identified.

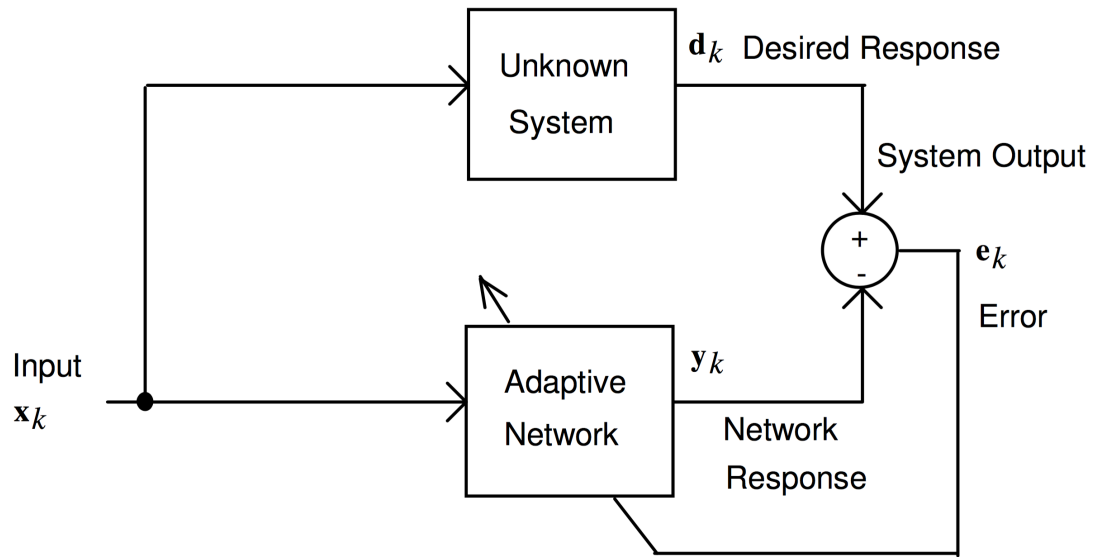


FIGURE 2.3: Basic Adaptive Filter for System Identification[3]

For example, in the case of non-blind deconvolution, x_k can be considered the estimation of the PSF, d_k can be considered the RF-line $y(n)$, and $h(n)$ is the unknown system.

To Identify the system, this process is taken:

1. x_k is convoluted with some initial guess to produce the first Network Response
2. The Error function is calculated by subtracting the Network Response from the Desired Response and is inputted into the Adaptive Network
3. If the cost function has a large value, another guess is made. The new guess is made using a learning algorithm that depends on both the value of the cost function as well as other parameters
4. If the error function is small, then the Network Response is approximately equal to the desired response, and so the guessed system is the unknown system.

There are many variables that can be changed to tailor the adaptive filter to one's needs. One of the main variables is the learning algorithm that is responsible of changing the adaptive network in every iteration. The learning algorithm is most commonly an intensive equation which takes into account the cost function, the previous estimation of the network response, and many other variables. Chapter 3 shows that the learning algorithm is linear and the error function is not calculated by simple arithmetic; rather, it is calculated after a mapping to a different domain is done.

2.2.4 Blind-deconvolution via Single Input Multiple Output Model (SIMO)

SIMO-based blind deconvolution is based on treating the echo response as a black box whose input is the PSF and whose output is a collection of RF-lines[28]. In this approach:

$$y_k(n) = x(n) * h_k(n) \quad (2.7)$$

$$Y_k(f) = X(f) \cdot H_k(f) \quad (2.8)$$

$$X(f) = \frac{Y_k(f)}{H_k(f)} \quad (2.9)$$

where the subscript k refers to the k^{th} A-scan and the upper-case letters in 2.8 refer to the DFT of their lower-case counterparts in 2.7. In this case, we do not need information about $X(n)$; we only need to solve for $H_k(n)$. Thus, assuming $X(f)$ is a common variable for all A-scans:

$$\frac{Y_i(f)}{H_i(f)} = \frac{Y_k(f)}{H_k(f)}$$

$$Y_i(f) \cdot H_k(f) = Y_k(f) \cdot H_i(f)$$

For N A-scans and N variables, this process produces $\frac{N(N-1)}{2}$ equations. Since PSF may have spatial dependency, one can use only consecutive scans to estimate the tissue response function.

2.2.5 Blind-deconvolution via Inverse Filtering

A popular Blind-deconvolution model is based on using the inverse filtering approach[53, 54]. Inverse filtering is based on restructuring the convolution model, then solving for both the echo response and the inverse of PSF simultaneously. The convolution model can be restructured as follows:

$$\begin{aligned} y(n) &= x(n) * h(n) \\ Y(f) &= X(f) \cdot H(f) \\ H(f) &= \frac{1}{X(f)} \cdot Y(f) \\ H(f) &= S(f) \cdot Y(f) \end{aligned}$$

and so the restructured convolution model is:

$$h(n) = s(n) * y(n) \tag{2.10}$$

This restructured convolution model comes with two problems: the scale ambiguity problem and phase ambiguity problem. The scale ambiguity arises from the fact that the convolution model is

$$y(n) = \frac{1}{a} x(n) * ah(n) \tag{2.11}$$

where a is arbitrary scalar, and the phase problem arises from the fact that

$$y(n) = x(n - n_o) * h(n + n_o) = x(n + n_o) * h(n - n_o) \quad (2.12)$$

where n_o is an arbitrary constant. Those two problems can be solved by changing the assumption of the restructured model to be

$$\gamma h(n - n_o) \approx s(n) * y(n) \quad (2.13)$$

Estimating $s(n)$ requires the assumption that $h(n)$ is independent and identically distributed (i.i.d) and non-Gaussian random variable. This is essential as the estimation method takes advantage of this assumption and builds on it.

Taking the central limit theorem into account, and because the PSF must be Gaussian, the convolution between the Gaussian PSF and non-Gaussian $h(n)$ is always more Gaussian. The optimal inverse filter can then be determined using this property to restore the non-Gaussianity of the data. To achieve this task, one must minimize the entropy of the deconvolved result. This idea was first proposed in [55] and implemented in [56].

In [55], maximizing the non-Gaussianity is done by the following:

$$s_{opt}(n, m) = \operatorname{argmax}_s \left[\frac{\sum_n \sum_m |(s(n, m) * y(n, m))|^4}{\sum_n \sum_m |(s(n, m) * y(n, m))|^2} \right] \quad (2.14)$$

where m represents the m^{th} RF-line and the corresponding tissue response function. Although it has been proven to be an effective measure of non-Gaussianity, using the forth moment in this manner may be problematic because of its inability to account for large and unsuccessful data samples.

To improve the robustness of 2.14, [57] suggests generalizing the equation to find an optimal filter using the following equation:

$$s_{opt}(n, m) = \operatorname{argmax}_s \left[\frac{\sum_n \sum_m |(s(n, m) * y(n, m))|^p}{\sum_n \sum_m |(s(n, m) * y(n, m))|^{p/2}} \right] \quad (2.15)$$

Another approach is the Claerbout's measure and the resulting Claerbout's parsimonious deconvolution [58], which is based on inverse filtering with s_{opt} defined as:

$$s_{opt}(n, m) = \operatorname{argmax}_s \left[\frac{1}{NM} \sum_n \sum_m \left(\frac{NM |(s(n, m) * y(n, m))|^2}{\sum_n \sum_m |(s(n, m) * y(n, m))|^2} \times \log \left(\frac{NM |(s(n, m) * y(n, m))|^2}{\sum_n \sum_m |(s(n, m) * y(n, m))|^2} \right) \right) \right] \quad (2.16)$$

Regardless which method is used from Equation 2.14, 2.15, or 2.16 the procedure is always the same. An adaptive filter is used to carry out the calculation using the steepest decent algorithm [59].

2.3 Conclusion: post-processing methods' compatibility for ultrasonic skull imaging

Methods mentioned in Section 2.2 are all outstanding approaches to the convolution model in ultrasonography. However, in the case of skull imaging, these methods encounter several difficulties. For example, the presence of the diploe layer physically distorts the path of the beams. Thus, in the case of SIMO (Sections 2.2.4) and Inverse Filtering (Section 2.2.5), which rely on adjacent scans for estimating $h(n)$, the results will be misleading.

The most reliable approach for skull profile extraction is, therefore, to tackle each RF-line separately, and filter out non-conclusive results. For this case, in order to estimate $h(n)$ as accurately as possible, a precise estimation of the PSF is critical. Estimating the PSF can be done either through the ARMA Model (Section 2.2.1) or through homomorphic estimation using cepstrum (Section 2.2.2). After estimating PSF it is necessary to perform deconvolution to acquire $h(n)$. Adaptive filtering shown in Section 2.2.3 is one of the most stable methods to perform Non-blind deconvolution to acquire an accurate estimation of $h(n)$. However, the deconvolution process proves more accurate for the cases where consecutive reflections are separated by a time delay larger than the pulse length. In skull imaging, Adaptive filtering based deconvolution fails to locate the boundaries of the skull since most of the reflections from the skull overlap.

In this study, a reliable and robust novel signal-processing technique, referred to as the Selective Echo Extraction algorithm (SEE), is developed for the specific case of ultrasonic skull imaging and accurate profile extraction. SEE does not rely on an accurate pre-measurement of the PSF for clear results eliminating the effects of the spatial dependence of PSF. In fact, only the acquisition system specifications and a rough estimate of the skull's acoustical properties are essential for the process. The method is capable of disregarding the distortions caused by the diploe layer, reviving reflections off of the skull-brain boundary, and accurately measuring the skull's inner boundary and its variable thickness across the examination area. Additionally, a proposed method that utilizes SEE is shown to be able to measure the averaged attenuation coefficient of the skull.

Chapter 3

Theory and simulations

Acquiring skull profile from a distorted ultrasonic B-Scan proves quite difficult using conventional signal processing techniques. This chapter introduces a novel method for blind-deconvolution to acquire a clear image of the skull's innermost curvatures. The suggested Selective Echo Extraction Algorithm (SEE) can be used to accurately detect both inner and outer curvatures of the skull. Furthermore, SEE can be utilized to attain the average attenuation coefficient of the skull.

Chapter 3 is divided into four sections: Section 3.1 introduces the algorithm and thoroughly discusses its details, Section 3.2 shows simulation results of B-Scans processed through SEE and the custom-designed curve fitting method used to acquire a correct curvature of the skull, Section 3.3 shows how SEE can be utilized to determine the attenuation coefficient in the skull, and Section 3.4 discusses the importance of SEE and the potential for its applications in ultrasonic post-processing.

3.1 The Selective Echo Extraction algorithm

For the case of ultrasonic skull profile extraction, current conventional methods for post-processing of RF data from the probed skull segment do not produce accurate results as discussed in Chapter 2. For this reason, the Selective Echo Extraction (SEE) algorithm has been developed and reported in this thesis. The skull structure by nature, as discussed in Section 1.5, has three layers. The middle layer which is referred to as “diploe” causes first and second strong reflections that could be mistaken for the second boundary of the skull structure when using conventional methods. SEE is a signal processing technique that is based on extracting only useful information from a noisy ultrasound scan obtained from a skull geometry.

The convolution model discussed in Chapter 2 states that:

$$y(n) = x(n) * h(n) \quad (3.1)$$

where $y(n)$ is the collected A-Scan, $x(n)$ is the point spread function, and $h(n)$ is the tissue response function. The convolution model in the skull portion of the A-Scan can be further expanded as follows.

$$y(n) = x(n) * (h_b(n) + h_d(n) + h_\eta(n)) \quad (3.2)$$

where $h_b(n)$ represents the portion of the reflectivity function representing the inner most and the outer most boundaries of the skull, $h_d(n)$ represents the reflections caused by diploe, and $h_\eta(n)$ represents the noise in the response function.

The goal of the SEE is to extract $h_b(n)$ and disregard all unnecessary information included in the reflectivity function. In order to do so, SEE is created as per the adaptive filter model and is tailored to the needs of the proposed convolution model shown in equation 3.2. In this section, the process of SEE is implemented

in Algorithm 1 and each step in the Algorithm is thoroughly discussed to show the physics and calculations performed to achieve the desired results.

Algorithm 1 The Selective Echo Extraction Algorithm

Input: $y, F_c, BW, N, z_f, d, W, c_s, \rho_s, \alpha, d_{min}, d_{max}$

▷ y : Normalized RF-line in time domain.

▷ F_c, BW : The central frequency and bandwidth of the transducer [MHz]

▷ N, z_f : The number of elements used to focus. and the focal distance [m]

▷ d, W : The pitch and element size of the transducer [m]

▷ c_s, ρ_s, α : The speed of sound [$\frac{m}{s}$], density [$\frac{kg}{m^3}$], and attenuation coefficient [$\frac{Np}{mMHz}$] of the skull

▷ d_{min}, d_{max} : The minimum and maximum thicknesses of the skull.

Output: h_b

▷ h_b : The reflectivity function corresponding to outer boundaries of the skull

```

1:  $\sigma_\omega = \frac{1}{2.67BWf_c}$ 
2:  $\hat{x} = e^{-\frac{t^2}{2\sigma_\omega^2}}$ 
3:  $t_1 = \text{argmax}(y)$  ▷ the skull's outermost boundary
4: for  $t = t_1 + (d_{min} : d_{max})/c_{skull}$  do
5:   reset  $\hat{h}$ 
6:    $\hat{h}(t_1) = 1$ 
7:    $\hat{h}(t) = \frac{1}{N} \sum_{n=1}^N \left[ \text{sinc} \left( \frac{W|\frac{N+1}{2}-n|df_c}{t_2^2 c_s^2} \right) e^{-2\alpha\sqrt{(|\frac{N+1}{2}-n|d)^2 + (t-t_1)^2 c_s^2}}$ 
      $e^{-\left(t - \left(\sqrt{(|\frac{N+1}{2}-n|d)^2 - t_2^2 c_s^2 - z_f}\right)/c}\right)^2 / (2\sigma_\omega^2)} \right] \left( \frac{2c_s \rho_s}{c_s \rho_s + c_w \rho_w} \right)^2 \frac{c_s \rho_s - c_t \rho_t}{c_s \rho_s + c_t \rho_t}$ 
8:    $\hat{y} = \hat{x} * \hat{h}$ 
9:    $c_{y\hat{y}} = y * \hat{y}$ 
10:   $c_{y\hat{y}}(n) = c_{y\hat{y}}(n - \text{argmax}(c_{y\hat{y}}))$ 
11:   $e(t) = \max|c_{y\hat{y}}(t) - c_{y\hat{y}}(-t)|$ 
12:  if  $e$  contains a global minimum then
13:     $t_2 = t_1 + \text{argmin}(e)$  ▷ skull's innermost boundary
14:    reset  $\hat{h}$ 
15:     $\hat{t}_1 = 1$ 
16:     $\hat{h}(t_2) = \frac{1}{N} \sum_{n=1}^N \left[ \text{sinc} \left( \frac{W|\frac{N+1}{2}-n|df_c}{t_2^2 c_s^2} \right) e^{-2\alpha\sqrt{(|\frac{N+1}{2}-n|d)^2 + (t_2-t_1)^2 c_s^2}}$ 
      $e^{-\left(t_2 - \left(\sqrt{(|\frac{N+1}{2}-n|d)^2 - t_2^2 c_s^2 - z_f}\right)/c}\right)^2 / (2\sigma_\omega^2)} \right] \left( \frac{2c_s \rho_s}{c_s \rho_s + c_w \rho_w} \right)^2 \frac{c_s \rho_s - c_t \rho_t}{c_s \rho_s + c_t \rho_t}$ 
17:    break
18:  end if
19: end for

```

In order for SEE to commence, only elementary information is needed along side the A-Scan. Mainly, information related to experimental setup such as the transducer's central frequency, bandwidth, pitch, element size, the number of elements used for focusing, and the focal distance. Additionally, information is needed about the target media, in this case the skull, such as the attenuation coefficient, the speed of sound, and a rough estimation of the skull's minimum and maximum thicknesses. These properties, except the speed of sound, can be roughly estimated and will not reduce the accuracy of the method. The speed of sound, however, is a key property that is used to convert the samples from time based to distance based via the basic formula $d = ct$, thus, must be provided with the least amount of error.

The behavior of the point spread function (PSF) is well known in ultrasound to be a Gaussian modulated sinusoidal waveform [4]. The waveform of PSF is produced by the vibration of a piezoelectric element as a response to an applied square electric pulse.

In a blind deconvolution problem, as discussed in Chapter 2, it is essential to estimate the PSF before applying deconvolution or to estimate the PSF simultaneously with the reflectivity function. However, Since SEE is a numeric method rather than deterministic, it is unnecessary to estimate both aspects of the PSF: Gaussian and sinusoidal. Therefore, additional processing can be avoided by only estimating the portion of PSF with the dominant effect: the Gaussian portion. The variance of the Gaussian portion of PSF can be calculated directly from the frequency and bandwidth of the transducer as follows:

$$\sigma_\omega = \frac{1}{2.67BW f_c} \quad (3.3)$$

then the estimated PSF \hat{x} , in line 2 of algorithm 1 is proposed to be a Gaussian function as follows:

$$\hat{x} = e^{-\frac{t^2}{2\sigma_\omega^2}} \quad (3.4)$$

where σ_ω is the pulse width of the excitation signal. It is important to note that the estimated PSF is not claimed to fully represent the original PSF, rather is used only for calculations inside the algorithm.

In an ideal experimental or clinical setup, reflections are expected to occur at the following boundaries: the coupling medium and scalp boundary, the scalp and skull boundary, the different layers of the skull, and the skull and brain boundary. An estimation of the reflection at each boundary is described by the reflection coefficient formula for normal incidence:

$$R = \frac{Z_1 - Z_2}{Z_1 + Z_2} \quad (3.5)$$

where Z_1 and Z_2 represent the acoustic impedance of the first and second media at a specific boundary, respectively. The transmission coefficient, on the other hand, is:

$$T = \frac{2Z_2}{Z_1 + Z_2} \quad (3.6)$$

such that the $R + T = 1$. The acoustic impedance, Z , is defined as:

$$Z = \rho c \quad (3.7)$$

where ρ is the density in the medium, and c is the speed of sound in the medium.

In medical application, transducers are mostly designed to be water or tissue coupled. Thus, at the coupling medium-scalp boundary, the impedance difference between the two media is minimal and the reflection coefficient is small; therefore,

most of the wave is transmitted. At the scalp-skull boundary, however, the reflection coefficient is rather high since the difference between the acoustic impedances is high ($Z_{tissue} \approx 1.6 \times 10^6 \left[\frac{kg}{m^2s} \right]$ while $Z_{bone} \approx 6.2 \times 10^6 \left[\frac{kg}{m^2s} \right]$)[65, 69]. Thus, it is fair to state that the reflection with the highest amplitude in the A-Scan occurs at the scalp-skull boundary. This fact is utilized in the algorithm at line 3, where the first boundary of the skull is shown to be at the location of the highest peak. Additionally, since the y is normalized, the amplitude of the first peak in the reflectivity function must be unity as shown in line 6.

To find the outermost boundary of the skull, the algorithm loops through various proposed second boundary locations ranging from the minimum to the maximum possible thickness provided. Thereafter, the algorithm performs calculations to determine the most accurate estimation of the location of the second boundary. The loop is performed in line 4 of Algorithm 1. Since in any given A-Scan the acquired data is in units of time rather than distance, the loop is performed in the time domain.

For each proposed location of the outermost boundary, the amplitude of the reflection must be calculated to properly perform comparison between the original A-Scan and the proposed A-Scan. The amplitude of this reflection is dependent on the distance from the first reflection, the nature of the skull, and the nature of the wave. Each of these factors which contribute to the amplitude of the reflection are discussed bellow.

Although the diploe layer of the skull is not considered to be a homogeneous medium, the compact bone layers is composed from a dense homogeneous material [2, 60]. Consider the propagation of a wave in a solid lossy medium [4, 61]. The pressure, p , wave propagation in a homogeneous medium is expressed as follows:

$$\nabla^2 p - \frac{1}{c^2} \frac{\partial^2 p}{\partial t^2} + L(t) * p = 0 \quad (3.8)$$

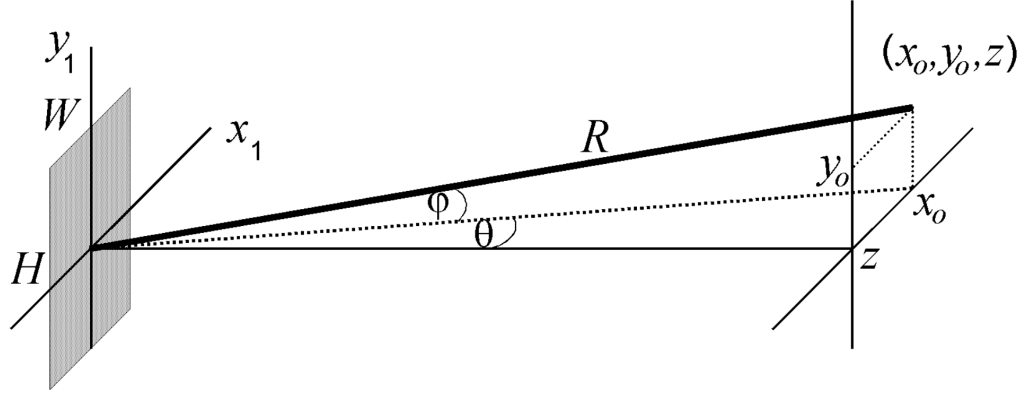


FIGURE 3.1: Geometry defining the coordinate system for the Fraunhofer approximation for a rectangular transducer.[4]

where c is the phase velocity at a reference frequency of ω , and $L(t)$ is the convolutional loss operator that guarantees causality and which accounts for the effects of dispersion and attenuation. The integral solution to this equation in the z direction can be expressed as:

$$p(z : t) = \frac{1}{2\pi} \int_{-\infty}^{\infty} \underline{p}(0 : \omega) e^{-i(\frac{\omega}{c} - i\alpha(\omega))z} e^{i\omega t} d\omega \quad (3.9)$$

where \underline{p} is the phasor pressure produced by the transducer and α is the attenuation coefficient as a function of angular frequency ω .

The phasor pressure can be calculated using the Fraunhofer Approximation [4].

For a rectangular transducer, The phasor pressure is given by:

$$\underline{p}(x_0, y_0, z : \omega) = \frac{\omega \rho_0 c_0}{2\pi R} e^{-ik \left[z + \frac{x_0^2 + y_0^2}{2z} \right]} W H \text{sinc} \left(\frac{W x_0}{\lambda z} \right) \text{sinc} \left(\frac{H y_0}{\lambda z} \right) \quad (3.10)$$

where W , H , R , x_0 , y_0 , and z are as shown in figure 3.1, and λ is the wavelength of the pressure wave in the target medium.

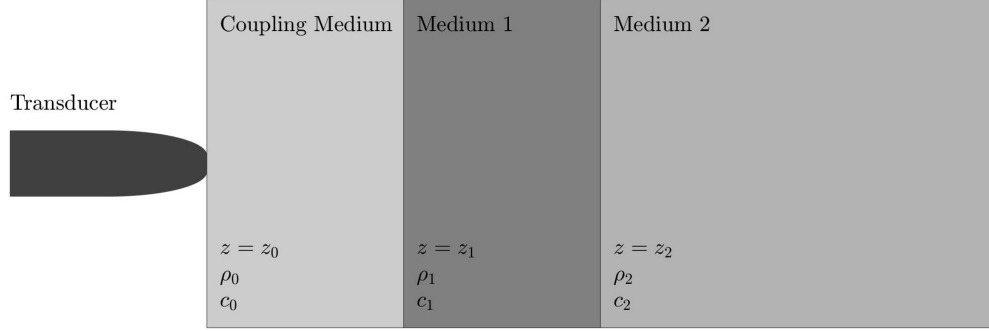


FIGURE 3.2: One transducer element used to image a simple two media sample.

Thus the pressure produced by one rectangular element in a lossy medium with attenuation coefficient $\alpha(\omega)$ is:

$$p(x_0, y_0, z : t) = \frac{\omega \rho_0 c_0}{4\pi^2 R} e^{-ik \left[z + \frac{x_0^2 + y_0^2}{2z} \right]} WH \operatorname{sinc} \left(\frac{Wx_0}{\lambda z} \right) \operatorname{sinc} \left(\frac{Hy_0}{\lambda z} \right) e^{-\alpha(\omega)z} \quad (3.11)$$

Equation 3.11 can be tailored to calculate the amplitude of peaks in A-Scans undergoing certain conditions. For example, in a simple case shown in figure 3.2, a transducer consisting of one rectangular element is used to acquire an A-Scan of a system consisting of two media. In a normalized A-Scan, the amplitude of the pressure at the first boundary is set to unity $p(z_1) = 1$ such that the reflectivity function at that location is 1: $h(z_1) = 1$. Thus, to calculate the amplitude at the boundary between Medium 1 and Medium 2 the following computations must be incorporated: the pressure at z_1 , the pressure at z_2 , the transmission coefficient at z_1 and the reflection coefficient at z_2 . The observed second boundary location corresponds to a reflection from normal incidence at $x_0 = 0$ and $y_0 = 0$. Since, the normalized pressure at $z_1 < z < z_2$ is:

$$p(z) = e^{-\alpha(\omega)(z-z_1)} \frac{2c_1\rho_1}{c_0\rho_0 + c_1\rho_1} \quad (3.12)$$

The amplitude of the reflectivity function from a normalized A-Scan at $z = z_2$ is:

$$h(z_2) = e^{-2\alpha(\omega)(z_2-z_1)} \left(\frac{2c_1\rho_1}{c_0\rho_0 + c_1\rho_1} \right)^2 \frac{c_2\rho_2 - c_1\rho_1}{c_1\rho_1 + c_2\rho_2} \quad (3.13)$$

The process discussed above can be extended to calculate the expected value of the reflectivity function of more complex cases. In the case of an A-Scan acquired from an N-element focused transducer, the pressure can be found by summing over the pressure produced by each element. Note that if N is even, the x position of the focal point at which the reflection is observed is between the central two element, alternatively, if N is odd, the x position of the focal point is at the center of the central element. Thus, the x_0 displacement between each element and the observed point is:

$$x_n = \left| \frac{N+1}{2} - n \right| d \quad (3.14)$$

where d is the pitch of the transducer. x_n is substituted in equation 3.11 as x_0 for each transducer element. Additionally, it's worth mentioning, that each element is excited at different excitation time to produce a focal point as discussed in Section 2.1. The pressure of each element is also dependent on time of arrival and the pulse width. Thus the pressure produced from N elements at a distance $z_1 < z < z_2$ and time t is given by:

$$p(z : t) = \frac{1}{N} \sum_{n=1}^N \left[\text{sinc} \left(\frac{W x_n}{\lambda z} \right) e^{-2\alpha(\omega)\sqrt{x_n^2 + (z-z_1)^2}} e^{-\frac{(t-t_n)^2}{2\sigma_\omega^2}} \right] \frac{2c_1\rho_1}{c_0\rho_0 + c_1\rho_1} \quad (3.15)$$

where the time delay is given by:

$$t_n = \frac{\sqrt{x_n^2 + z^2} - z_f}{c} \quad (3.16)$$

where z_f is the distance at which the transducer is focused. If $z = z_2$ then the reflection coefficient has to be considered as well a second transmission coefficient. Thus, the amplitude of the reflectivity function from a normalized A-Scan at $z = z_2$ is:

$$h(z_2) = \frac{1}{N} \sum_{n=1}^N \left[\text{sinc} \left(\frac{W x_n}{\lambda z} \right) e^{-2\alpha \sqrt{x_n^2 + (z-z_1)^2}} e^{-\frac{(\frac{z_2}{c_1} - t_n)^2}{2\sigma_\omega^2}} \right] \left(\frac{2c_1\rho_1}{c_0\rho_0 + c_1\rho_1} \right)^2 \frac{c_2\rho_2 - c_1\rho_1}{c_1\rho_1 + c_2\rho_2} \quad (3.17)$$

Line 7 of Algorithm 1, corresponds to an expanded form of equation 3.17 in terms of the variables available in the algorithm. Line 7 states:

$$\hat{h}(t) = \frac{1}{N} \sum_{n=1}^N \left[\text{sinc} \left(\frac{W \left| \frac{N+1}{2} - n \right| df_c}{tc_s^2} \right) e^{-2\alpha \sqrt{\left(\left| \frac{N+1}{2} - n \right| d \right)^2 + (t-t_1)^2 c_s^2}} \right. \\ \left. e^{-\left(t - \left(\sqrt{\left(\left| \frac{N+1}{2} - n \right| d \right)^2 - t^2 c_s^2} - z_f \right) / c \right)^2 / (2\sigma_\omega^2)} \right] \left(\frac{2c_s\rho_s}{c_s\rho_s + c_w\rho_w} \right)^2 \frac{c_s\rho_s - c_t\rho_t}{c_s\rho_s + c_t\rho_t} \quad (3.18)$$

This completes the estimation of h_b which is referred to as \hat{h} in the algorithm. The estimate of the A-Scan corresponding to the two skull boundaries, \hat{y} , is calculated in line 8 as the convolution of \hat{x} and \hat{h} . In line 9, the cross correlation between the original and the proposed signals is calculated and in line 10 the cross correlation function is centered about its maximum point. The centering is important to ensure that the first reflections in the original and proposed A-Scans are perfectly aligned.

The cross-correlation function between two arbitrary functions $f(t)$ and $g(t)$ describes the general dependence of the values of $f(t)$ at one time on the values of

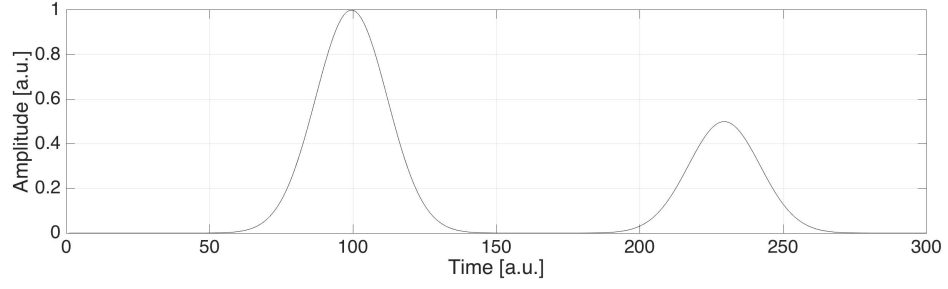
$g(t)$ at another time. Therefore, Cross-Correlation in line 9 provide a description of the similarity between the estimated signal and the original. Cross-correlation is calculated as follows[3]:

$$r_{fg}(\tau) = \lim_{T \rightarrow \infty} \frac{1}{T} \int_0^T f(t)g(t + \tau)dt \quad (3.19)$$

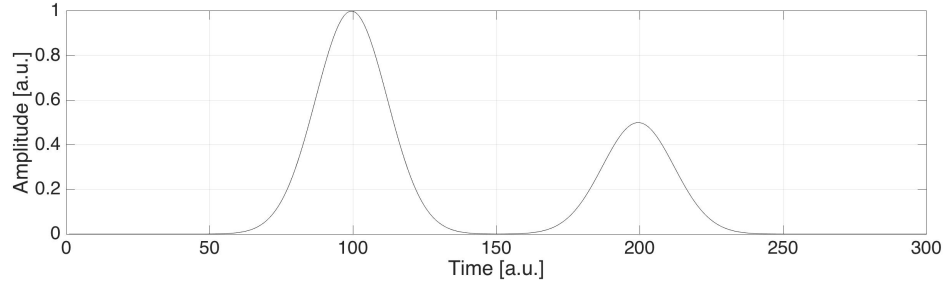
where $r_{fg}(\tau)$ is the cross correlation between the functions f and g at time τ , and T is the total observation time. To show the necessity of using cross correlation to compare the original A-Scan and the proposed A-Scan two cases are shown bellow.

Consider a hypothetical A-Scans with a PSF of Gaussian nature and two distinct reflections as shown in figure 3.3a. Assume the proposed estimation of the A-Scan is as shown in figure 3.3b. Then the Cross-Correlation between the original and the proposed A-Scan is given in figure 3.3c. The high peak in the center of the cross-correlation is a product of the first reflection from each A-Scans added to the product of the second reflections from each A-Scans. This is because the highest correlation between the two A-Scans happens at zero shift. The peak on the right side in the correlation, however, represents the product between the first reflection of the proposed A-Scan and the second reflection of the original A-Scan thus representing the behavior of the original A-Scan post the first peak. Similarly, the peak on the left side represents the correlation between the first reflection of the original with the second reflection of the proposed A-Scan.

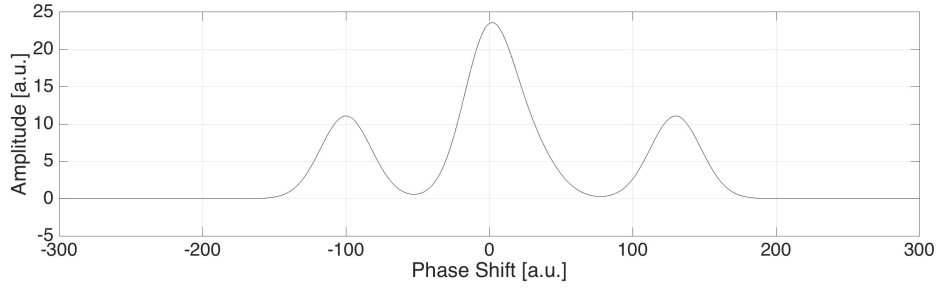
This convention is also shown in figure 3.4, where figure 3.4a contains the original A-Scan including many reflections and uniformly distributed error, and figure 3.4b contains the proposed A-Scan including only two reflections. It is safe to assume from these two cases that the right hand side of the correlation represents the original A-Scan behavior post first peak while the left hand side represents the proposed's A-Scan's behavior post first peak. Moreover, the cross-correlation produces results with no error which is essential in scans with low signal to noise ratio.



(A) Original A-Scan



(B) Proposed A-Scan



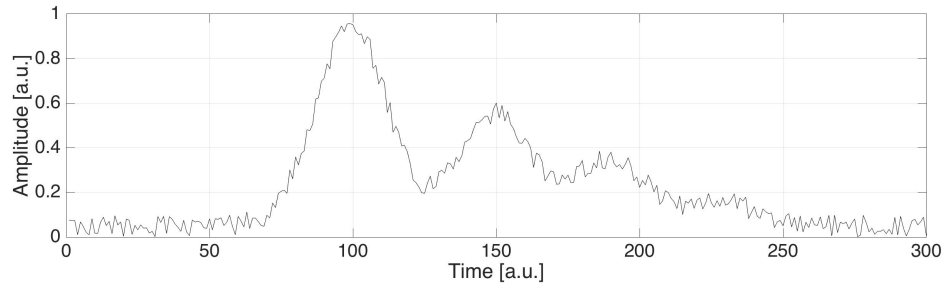
(C) Cross-Correlation between the original A-Scan and the proposed A-Scan

FIGURE 3.3: Cross-Correlation example for a hypothetical simple case of A-Scans with a Gaussian PSF

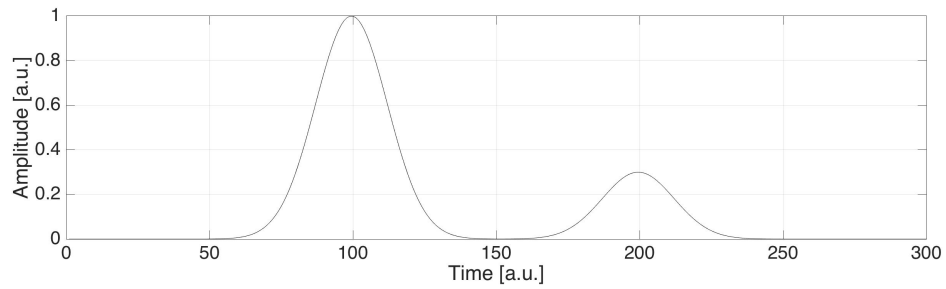
It is important to note that the similarity between the two sides of the correlation is maximum when \hat{y} best describes the h_b portion of the A-Scan. Therefore, the two sides of the correlation can be effectively used to produce an error factor between the proposed A-Scan and the Original. The error factor $e(\tau)$ is defined in line 11 as:

$$e(\tau) = \max |c_{y\hat{y}}(t) - c_{y\hat{y}}(-t)| \quad (3.20)$$

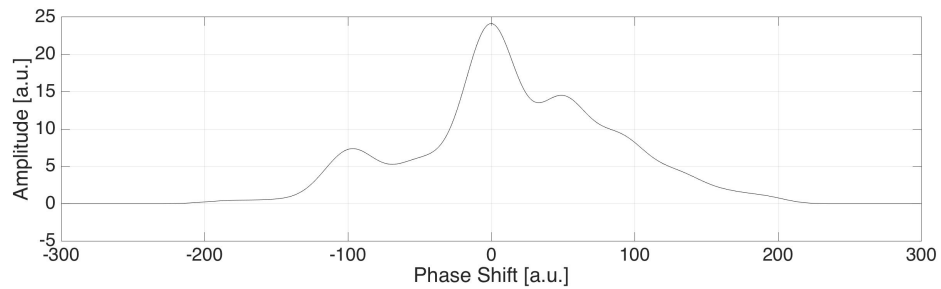
where $c_{y\hat{y}}$ is the cross correlation between the original A-Scan y and the proposed



(A) Original A-Scan



(B) Proposed A-Scan



(C) Cross-Correlation between the original A-Scan and the proposed A-Scan

FIGURE 3.4: Cross-Correlation example for a hypothetical complex case of A-Scans constructed with a Gaussian PSF and added uniformly distributed random error

A-Scan \hat{y} . $e(\tau)$ provides an illustration of the difference between the the original A-Scan and a proposed A-Scan where the proposed A-Scan contains only two peaks separated by time shift τ .

In every iteration shown in line 4 of the algorithm, a new A-Scan is proposed and the error for the time shift is calculated. After a few alterations, the process of detecting the highest similarity (lowest error) starts.

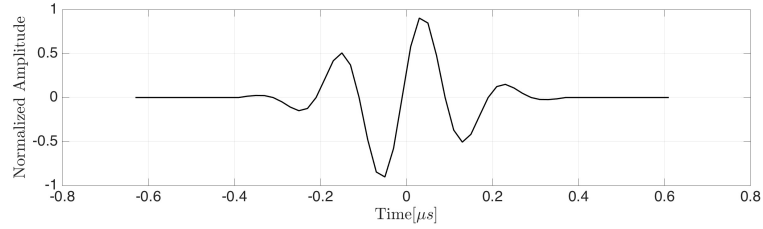
Highest similarity occurs when the error value reaches the global minimum. When

$e(\tau)$ contains a minimum of certain criteria that corresponds to the global minimum as stated in line 12, the algorithm fixates the location of the second peak at that minimum as shown in line 13, and exits the loop as shown in line 17. If the algorithm reaches the iteration that corresponds to the maximum thickness of the skull and is yet to detect a minimum, no second boundary will be included in the result. Although not detecting a second boundary may seem like a drawback to the algorithm, it is in fact an advantage: in sections of the skull that contain highly irregular second boundary, the ultrasound beam may deflect causing no second boundary echo in the A-Scan. By excluding the absolute minimum which does not behave as a global minimum in the error function as the second boundary, SEE ensures that any reflections that do not conform to the physical properties and conditions specified by the user are not mistaken to be the second boundary of the skull guaranteeing no false positives are detected.

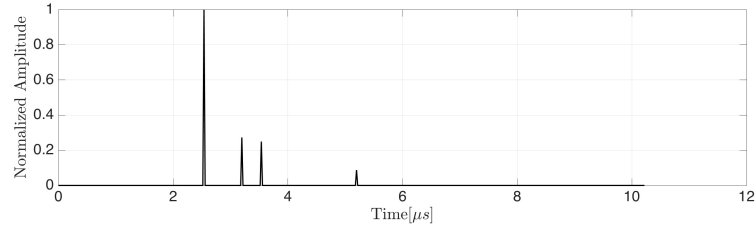
3.1.1 Simulation of SEE for single A-Scans

As a proof of concept, simulations of A-Scans with the same reflectivity function and different types of noise are carried out to test SEE. The reflectivity function is constructed to mimic the response from a skull sample containing diploe. Therefore, the reflectivity function contains four reflections: the first reflection occurs at a water-skull boundary, the porous layer introduces two separate reflections at $2mm$ and $3mm$ away from the first boundary. Finally, the inner most boundary of the skull produces a reflection $8mm$ away from the first boundary.

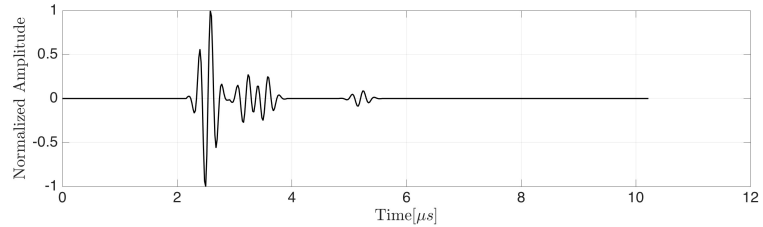
The PSF, the reflectivity function, and the original A-Scan with no additive noise are shown in figure 3.5. After processing the A-Scan using SEE, the portions of the A-Scan corresponding to the outer boundaries of the skull are retrieved as shown in figure 3.6a. The error function produced by SEE is shown in 3.6b, where the location of the minimum represents the location of the outermost boundary. It is worth noting that SEE exits as soon as a minimum is found, however, for



(A) The point spread function (PSF)



(B) The Reflectivity Function



(C) The A-Scan

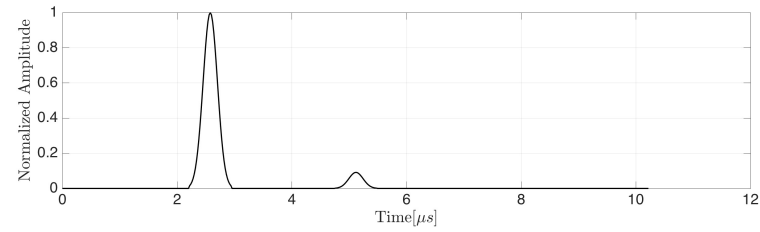
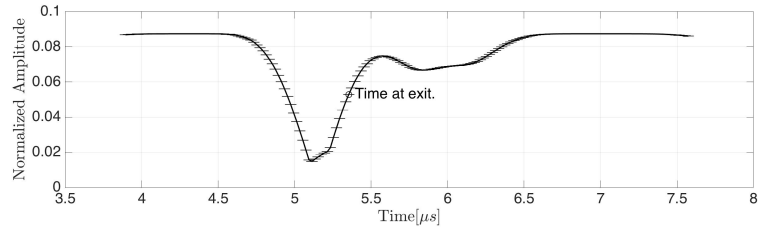
FIGURE 3.5: The point spread function in 3.5a convoluted with the reflectivity function in 3.5b produce the A-Scan shown in 3.5c.

the sake of this study the entire error function is shown and the location at which SEE would normally exit is noted on the figures of the error functions.

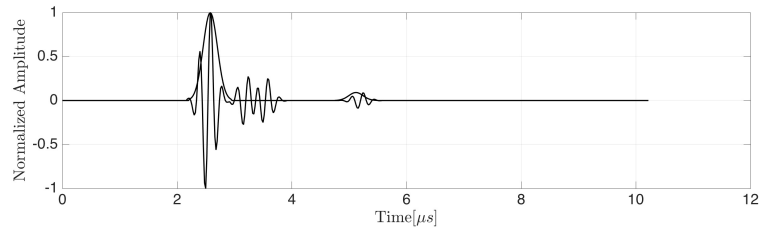
To clarify the SEE results, the original A-Scan and the A-Scan acquired from SEE are plotted on the same figure as shown in figure 3.6c. It is clear that SEE has successfully found the second peak of the A-Scan for the simplest case possible, in fact, SEE detected the peak within $0.36mm$ from the real value. More importantly, it has detected the peak within 0.6λ .

Consider a case where additive noise is present in the A-Scan, mainly:

$$y(n) = x(n) * h(n) + \eta(n) \quad (3.21)$$

(A) The Estimated A-Scan corresponding to $h_b(n)$ 

(B) The error function generated in SEE



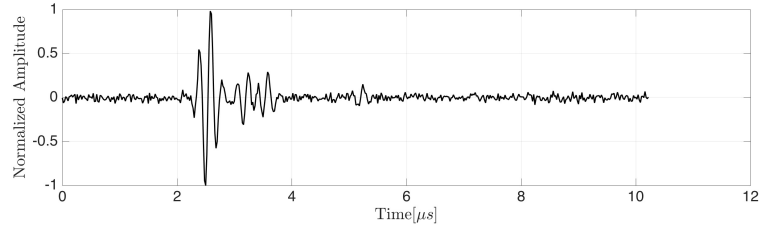
(C) Original A-Scan vs Processed A-Scan

FIGURE 3.6: Processing an A-Scan with no added noise.

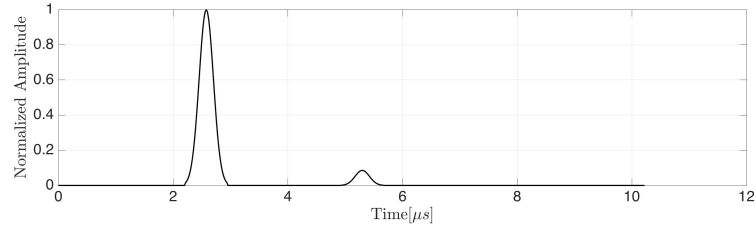
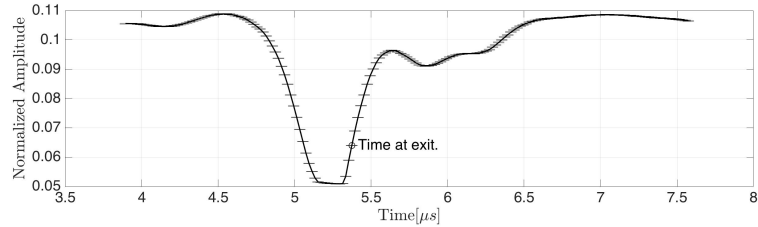
where $\eta(n)$ is white Gaussian noise. For this case, an A-Scan with a relatively high signal-to-noise ratio of 12dB/sample is shown in figure 3.7a. Note that the value of SNR is proportional to the amplitude of the signal, thus, the value of SNR is an average over the A-scan. It is clear that although the signal to noise ratio in the region of the second reflection is quite high, SEE is able to detect the location with an accuracy of 0.18mm or 0.3λ .

In the next simulation, the signal to noise ratio is reduced to a 6dB.sample SNR. The simulation is shown in figure 3.8. At this level of noise, the second reflection is comparable in amplitude to the additive noise. However, SEE is able to detect the location of the second peak with an accuracy of 0.12mm or 0.2λ .

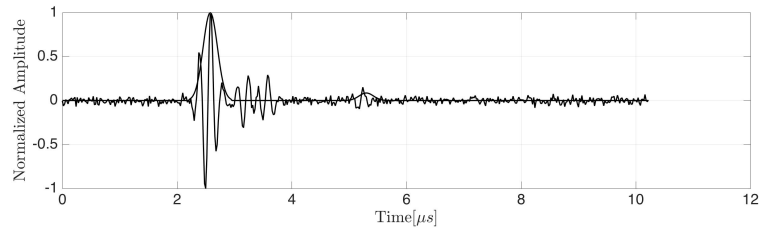
Another type of noise SEE is tested with is convoluted noise, mainly:



(A) The noisy A-Scan.

(B) The extracted A-Scan corresponding to h_b .

(C) The error function generated in SEE



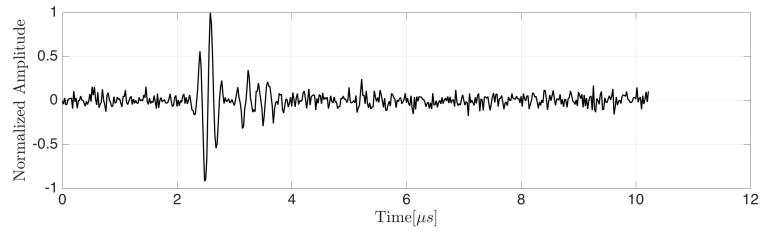
(D) Noisy A-Scan vs processed A-Scan.

FIGURE 3.7: Processing a noisy A-Scan with additive Gaussian noise corresponding to 12dB/sample SNR in the A-Scan.

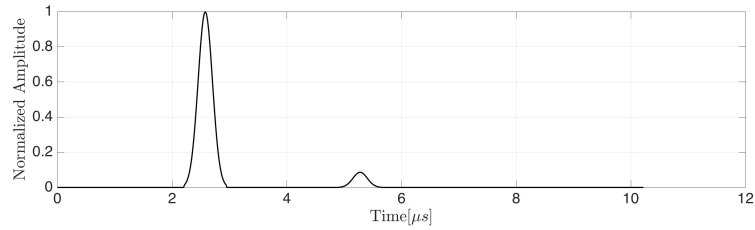
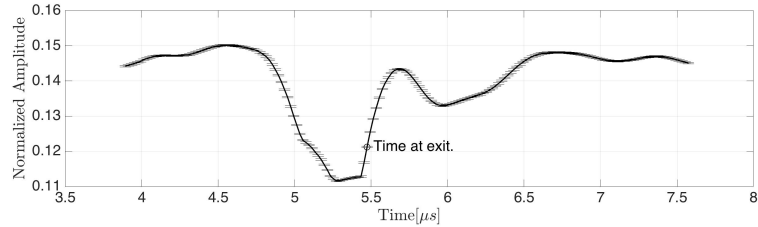
$$y(n) = x(n) * (h(n) + \eta_1(n)). \quad (3.22)$$

With this type of noise, the produced A-Scan will contain waveforms that are similar in nature to PSF. Convolved noise is especially hard to filter using conventional methods since it is present inside the reflectivity function.

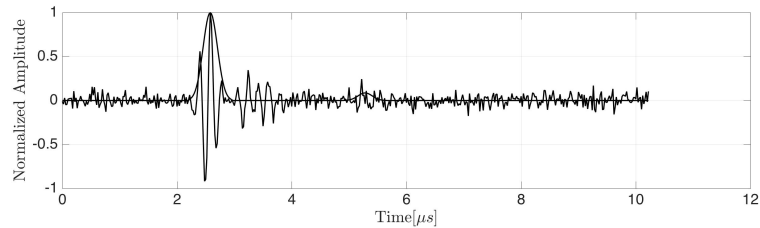
The first simulation carried out with this type of noise is with additive Gaussian



(A) The noisy A-Scan.

(B) The extracted A-Scan corresponding to h_b .

(C) The error function generated in SEE

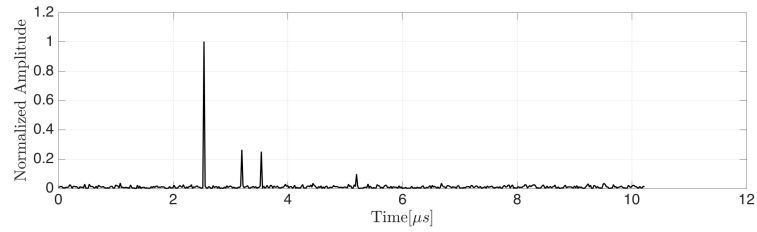


(D) Noisy A-Scan vs processed A-Scan.

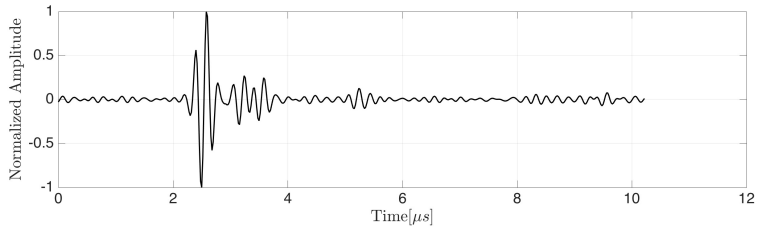
FIGURE 3.8: Processing a noisy A-Scan with additive Gaussian noise corresponding to $6dB/sample$ SNR in the A-Scan.

noise in the reflectivity function that corresponds to $12dB/sample$ SNR as shown in Figure 3.9. In this simulation, the peak location is detected with an accuracy of $0.06mm$ or 0.1λ .

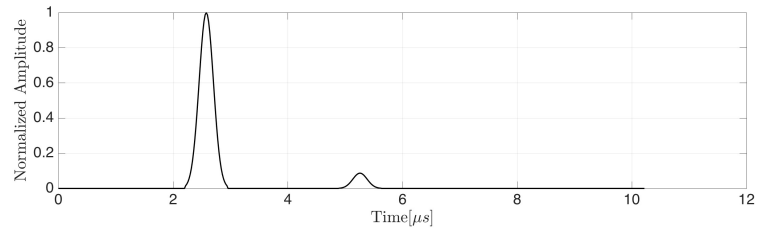
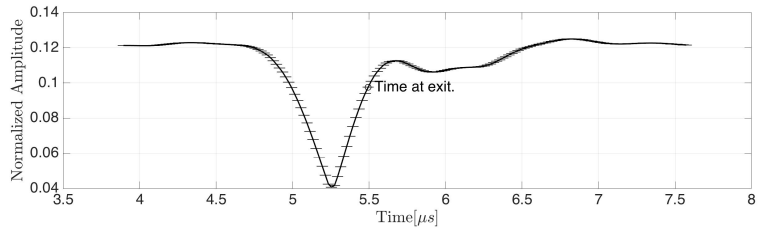
Similarly, another simulation is carried out with convoluted Gaussian noise which produces a reflectivity function with $6dB/sample$ SNR. The results from this simulation are shown in figure 3.10. The results show that the signal is detected with an accuracy of $0.06mm$ or 0.1λ .



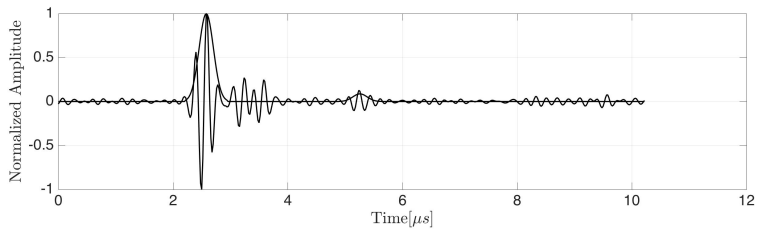
(A) The noisy reflectivity function.



(B) The noisy A-Scan.

(C) The extracted A-Scan corresponding to h_b .

(D) The error function generated in SEE

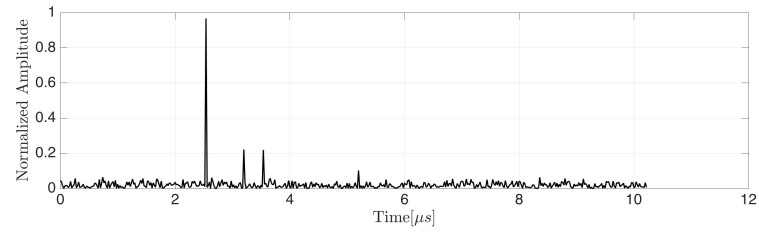


(E) The noisy A-Scan vs the processed A-Scan.

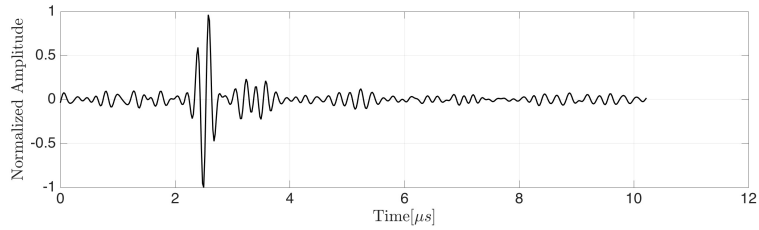
FIGURE 3.9: Processing a noisy A-Scan with convoluted Gaussian noise corresponding to $12dB/sample$ SNR in the reflectivity function.

Finally, a simulation with an A-Scan containing both types of noise is carried out as shown in figure 3.11. An A-Scan with both types of noise has the form:

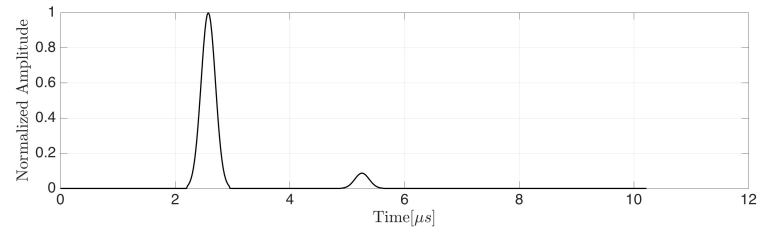
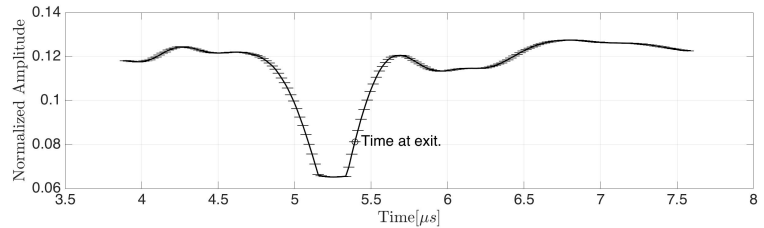
$$y(n) = x(n) * [h(n) + \eta_1(n)] + \eta_2(n) \quad (3.23)$$



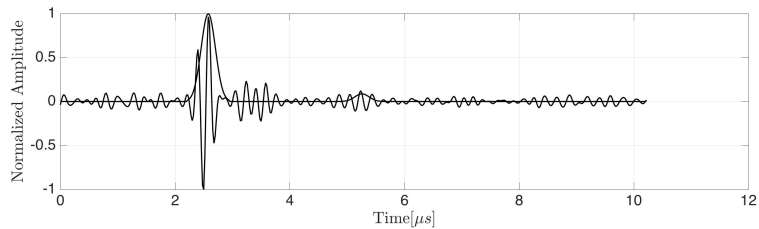
(A) The noisy reflectivity function



(B) The noisy A-Scan.

(C) The extracted A-Scan corresponding to h_b .

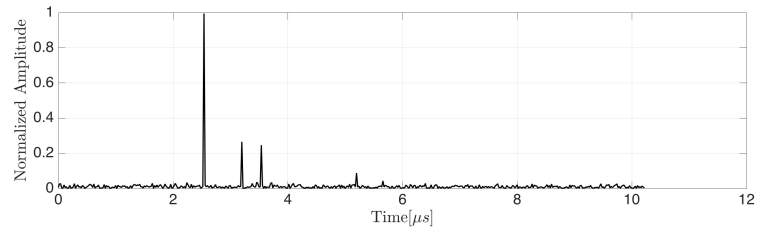
(D) The error function generated in SEE



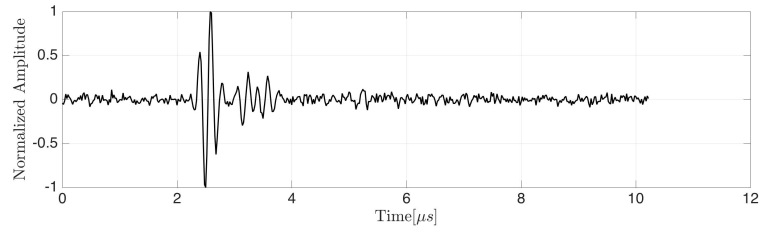
(E) The noisy A-Scan vs the processed A-Scan.

FIGURE 3.10: Processing a noisy A-Scan with convoluted Gaussian noise corresponding to $12dB/sample$ SNR in the reflectivity function.

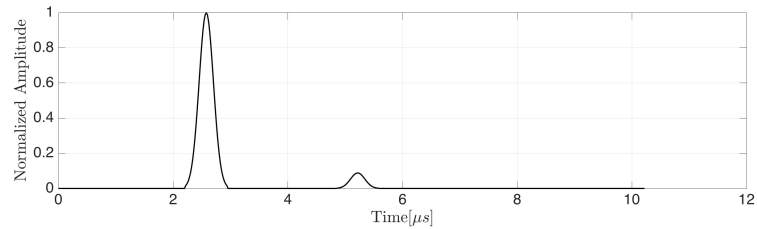
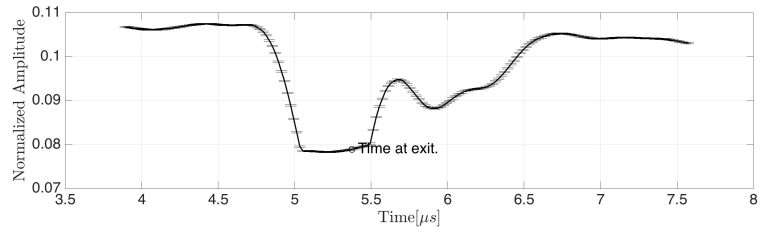
where η_1 produces convoluted noise which results in SNR of $12dB$ per sample in the reflectivity function and η_2 produces additive noise that results in SNR of $12dB$



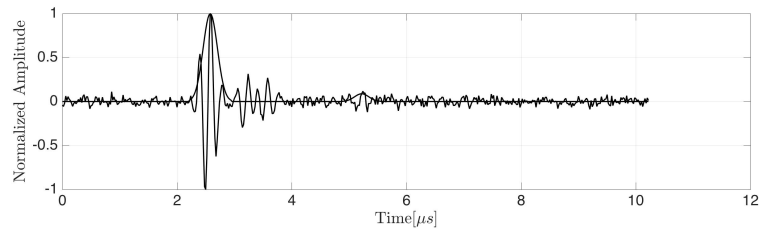
(A) The Noisy reflectivity function.



(B) The Noisy A-Scan

(C) The extracted A-Scan corresponding to h_b .

(D) The error function generated in SEE



(E) The Noisy A-Scan vs processed A-Scan.

FIGURE 3.11: Processing a noisy A-Scan with convoluted Gaussian noise corresponding to $12dB/sample$ SNR in the reflectivity function and additive Gaussian noise corresponding to $12dB/sample$ SNR in the A-Scan.

per sample in the A-Scan. The second boundary is detected with an accuracy of $0.06mm$ or 0.1λ .

In all of these simulations, SEE detected the reflectivity function corresponding to the two boundaries of the skull to an accuracy $0.23\lambda \pm 0.20\lambda$ or $0.14 \pm 0.12mm$. This shows that SEE has proven effective for scans with varying SNR and varying types of noise. The results are not surprising given the fact the SEE is not strictly mathematical nor does it depend strictly on Digital Signal Processing techniques: SEE relies heavily on the physics behind pressure wave propagation in the medium. Thus, the algorithm results in a more physically sound method than other methods that may detect false positives for the lack of incorporation of wave propagation, attenuation, beamforming, and the physical properties of the propagation media.

3.2 Applying SEE to determine the curvature of the skull from simulated B-Scans

In the case of skull imaging, two dimensional scans can be acquired using the full array and beamforming algorithms. Those B-Scans are composed of multiple A-Scans. To determine the curvature, SEE is applied to each A-Scan separately, and then, the information is combined to produce an accurate depiction of the curvature. Consider the B-Scan shown in figure 3.12. Each A-Scan in the proposed B-Scan is constructed similarly to the A-Scans shown in section 3.1.1. The first reflection is produced at the coupling medium-skull boundary, the second and third reflections are produced at $2 \pm 0.3[mm]$ and $3 \pm 0.3[mm]$ away from the first boundary, respectively. Those reflections mimic the porous layer present in the skull. Finally, a reflection is produced at the skull-brain boundary at varying distances as if the curvature of the skull has a sinusoidal form:

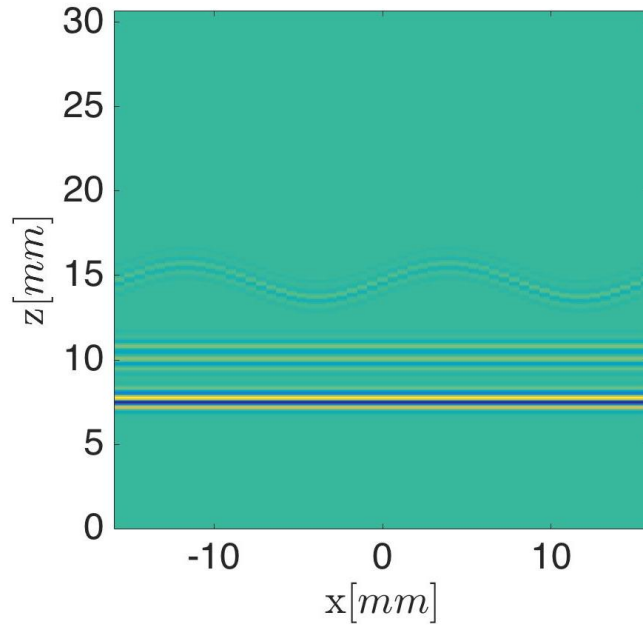


FIGURE 3.12: Noiseless B-Scan of a skull geometry.

$$z_2(x) = \sin\left(\frac{4\pi}{Mp}x\right) + 7 \quad (3.24)$$

where z_2 represents the location of the innermost boundary of the skull, M corresponds to the number of A-Scans acquired, p is the pitch of the transducer, and 7 is the average thickness of the skull. Note that all distances in equation 3.24 are in mm .

Similar to the process performed in section 3.1.1, SEE will be tested against different types of noise and noise levels incorporated into the B-Scan. Additive noise resulting in $12dB$ per sample SNR is applied to the B-Scan to produce the distorted B-Scan shown in figure 3.13a. The distorted B-Scan is then fed into SEE, one A-Scan at a time, to produce the curvature shown in 3.13b. The curve acquired from SEE is not considered the final output since it is irregular and could be inconclusive if outliers are present in certain complex cases. Therefore, curve fitting should be performed to produce a more reliable curvature.

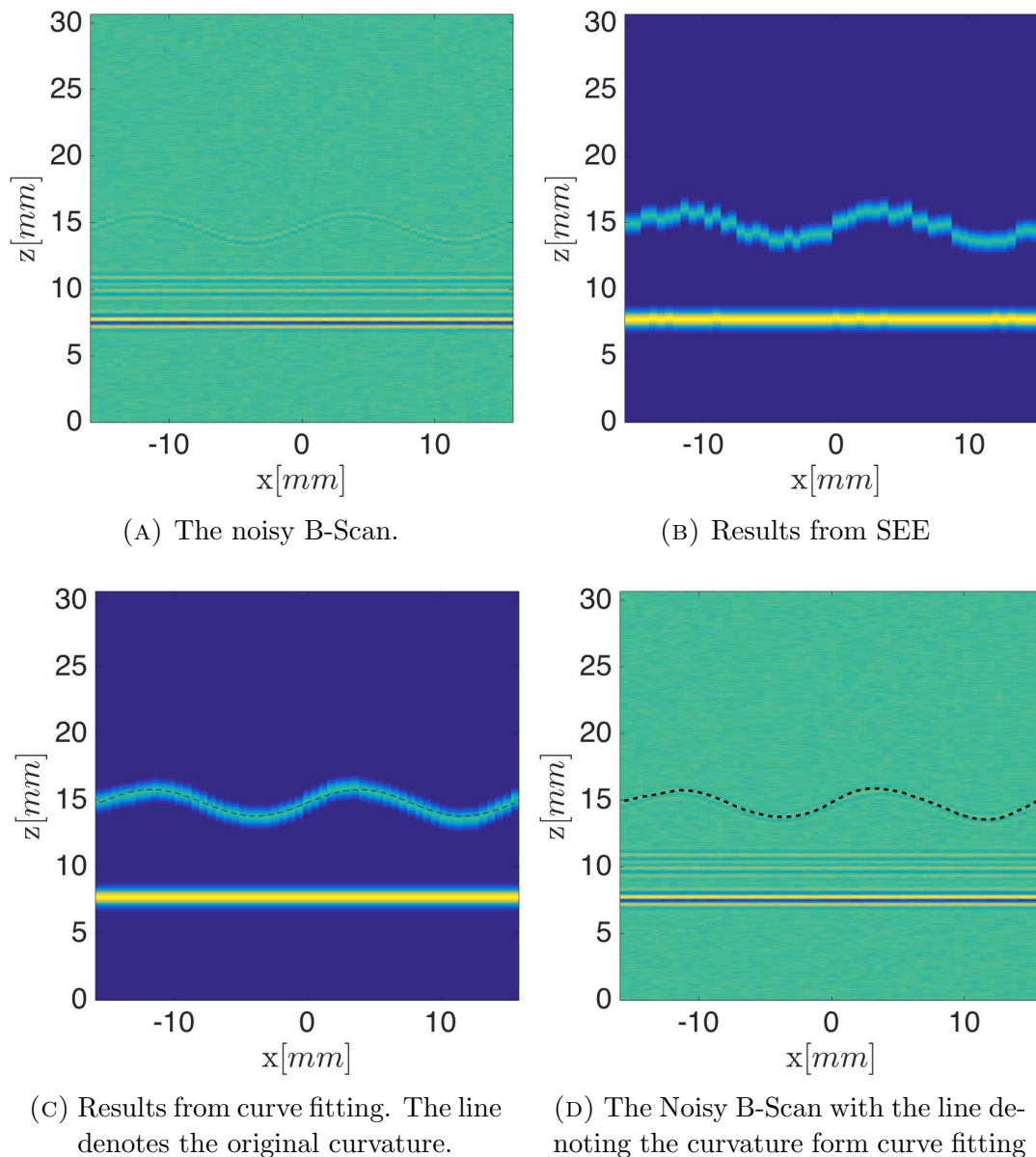


FIGURE 3.13: Processing a noisy B-Scan with Additive Gaussian noise corresponding to 12dB/sample SNR in each A-Scan.

Although applying a simple curve fitting algorithm using Fourier functions or polynomial functions seems to be a good approach, it is not an optimal method for this study. In more complex cases, the curvature of the skull does not exhibit a periodic behavior, therefore, those curve fitting methods are not optimal. To tackle this issue, the points acquired from SEE are segmented into smaller subsets, thereafter, curve fitting is applied to each subset, and points in overlapping subsets

are averaged to create an accurate depiction of the curvature.

The subsets in this study are chosen to be $10mm$ wide with a curve fitting algorithm using a third order polynomial. These parameters are chosen considering the fact that the skull, by nature, does not contain a high frequency of maxima and minima. It is postulated in this thesis that in a $10mm$ section there should not be more than one maximum and one minimum. Therefore the curve fit for each subset is calculated as follows:

$$z_{fit,k} = \begin{cases} fit(x, z(x), \sum_{n=0}^3 a_{kn}x^n) & (k - \frac{M-1}{2})p \leq x \leq ((k + N_{sub} - 1) - \frac{M-1}{2})p \\ 0 & else \end{cases} \quad (3.25)$$

where k represents the index of the subset ($k = 0, 1, \dots, M - N_{sub} + 1$), x is the location of the center of the elements at which the respective A-Scans are acquired: $x = (k - \frac{M-1}{2})p$, $z(x)$ is the location of the detected peak acquired from SEE, a_{kn} is the constant corresponding to the k^{th} curve fit and the n^{th} polynomial power, and N_{sub} is the number of A-Scans used for each subset. Note that if the boundary is not detected by SEE at any given A-Scan, that location will carry no weight in the curve fitting functions.

In the case where a subset contains a small number of detected points, N_{sub} is adjusted such that each subset contains no less than 10 A-Scans. This property proves more relative in chapter 4 where sections of the skull with a high slope fail to be detected since the transmitted waves deflect at a high angle.

The fit function is a standard Linear regression model created to minimize the deviation between the inputs (x and z) and the proposed curve fitting function.

The results from the curve fit for each subset are combined to produce a continuous curve as follows:

$$\hat{z} = \frac{\sum_{k=1}^{M-N_{sub}+1} f_k(x)u(f_k(x))}{\sum_{k=1}^{M-N_{sub}+1} u(f_k(x))} \quad (3.26)$$

where

$$f_k(x) = \sum_{n=0}^3 a_{kn}x^n \quad (3.27)$$

$$u(x) = \begin{cases} 1 & x > 0 \\ 0 & x \leq 0 \end{cases} \quad (3.28)$$

This allows for only non-zero values each curve fits to be averaged.

Results obtained from the curve fitting are referred to throughout the thesis as the final result. For the example given in figure 3.13, the results are shown in figure 3.13c. Another illustration is shown in figure 3.13d, where the image shows the original scan with a dashed line denoting the curve acquired from curve fitting post SEE.

Similarly, results from a B-Scan with additive noise corresponding to $6dB$ per sample SNR in each A-Scan are shown in figure 3.14. These results show that even when noise with comparable magnitude to the second boundary's amplitude is added to the B-Scan, SEE is able to detect the boundary to an excellent accuracy.

SEE is also tested with convoluted noise that corresponds to $12dB$ and $6dB$ per sample SNR in the reflectivity function of each A-Scan, as shown in figures 3.15 and 3.16, respectively.

To obtain a more realistic B-Scan, a simulation is carried out for a B-Scan using convoluted noise as well as additive noise. For this case, SEE is tested using a B-Scan containing Gaussian noise resulting in $SNR = 12dB/sample$ in the reflectivity function and Gaussian noise resulting in $SNR = 12dB/sample$ in each A-Scan. Results for this type of B-Scan are shown in figure 3.17.

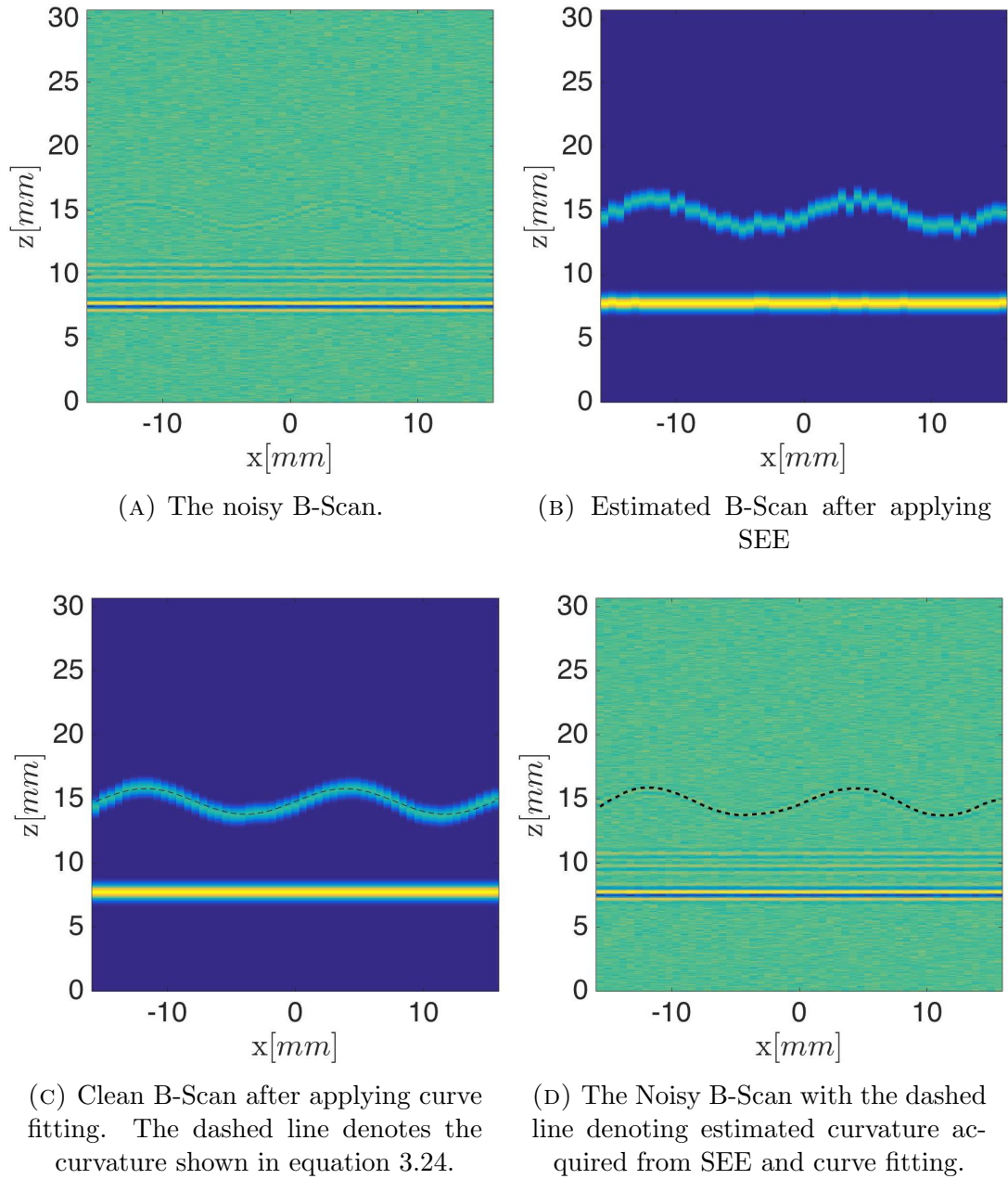


FIGURE 3.14: Processing a noisy B-Scan with Additive Gaussian noise corresponding to $6dB/sampel$ SNR in each A-Scan.

The accuracy of SEE and SEE with curve fitting can be calculates with respect to the original curve as follows:

$$\Delta z = mean(|\hat{z} - z|) \quad (3.29)$$

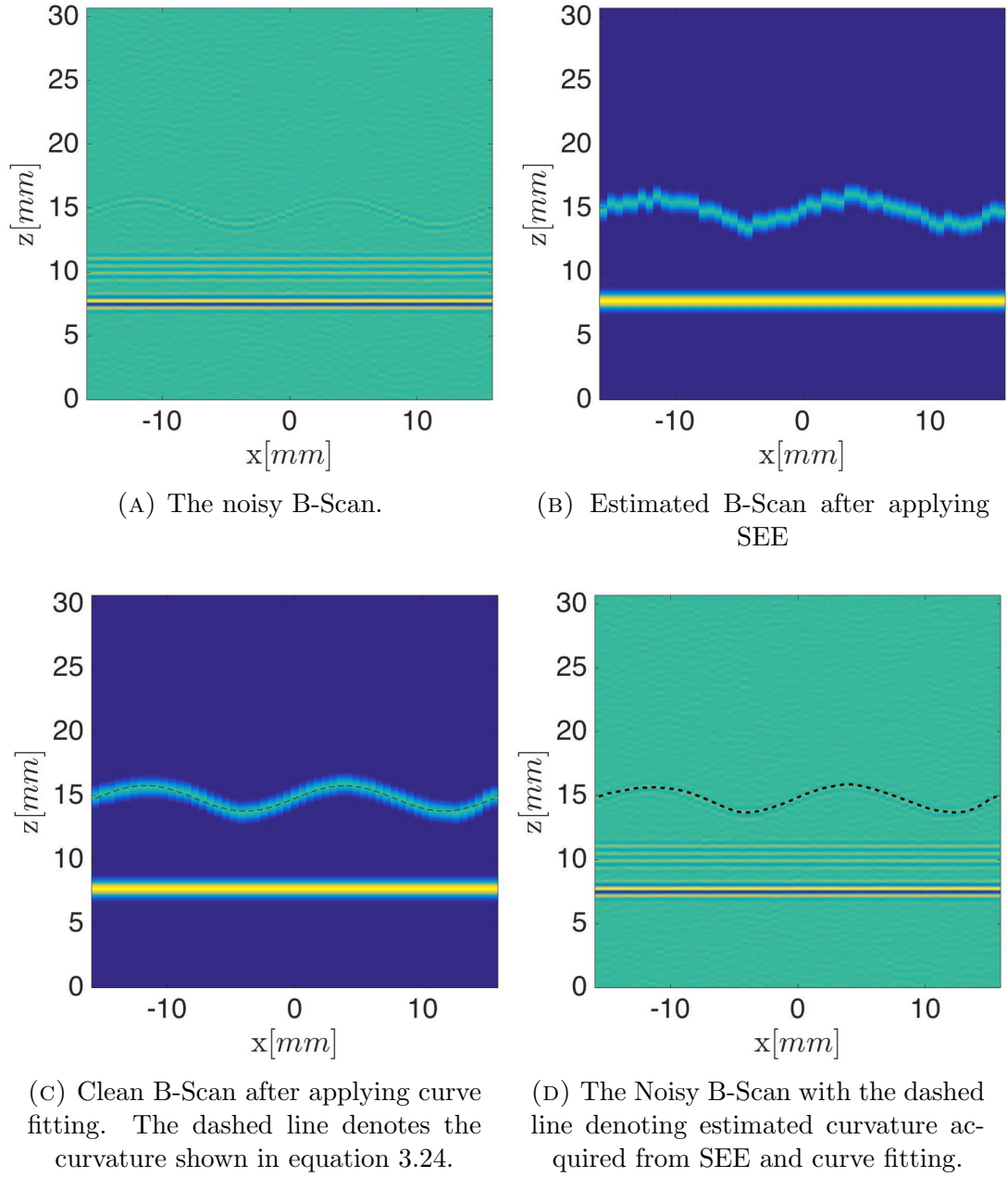


FIGURE 3.15: Processing a noisy B-Scan with convoluted Gaussian noise corresponding to $12dB/sample$ SNR in each reflectivity function.

and

$$\Delta z_\lambda = \frac{\Delta z f_c}{c_s} \quad (3.30)$$

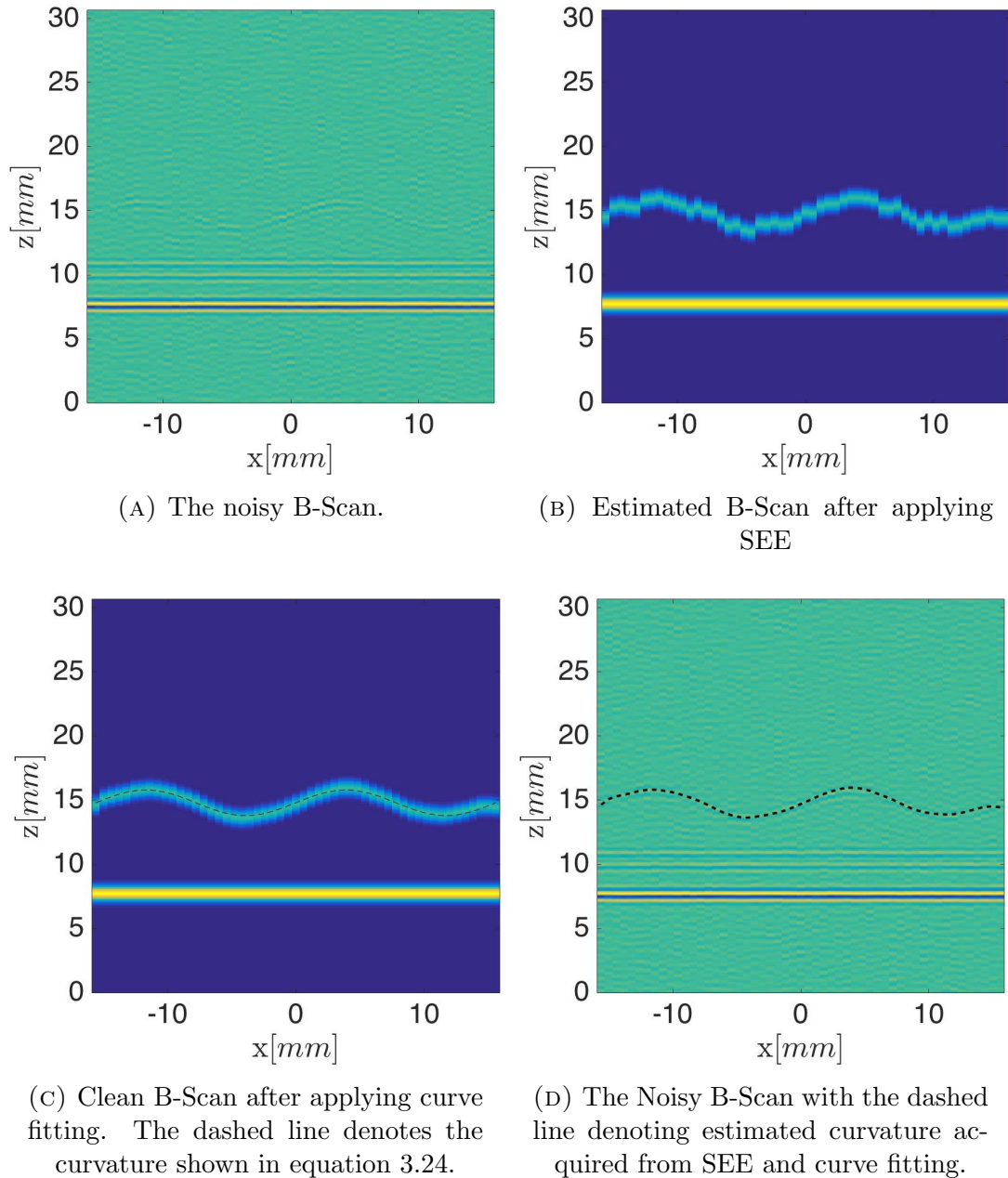


FIGURE 3.16: Processing a noisy B-Scan with convoluted Gaussian noise corresponding to $6dB/sample$ SNR in each reflectivity function.

The accuracy of SEE can be determined by substituting the values obtained directly from SEE for \hat{z} in equation 3.29. Alternatively, the accuracy of SEE with the additional step of curve fitting can be calculated by substituting the values from equation 3.26 as \hat{z} in equation 3.29. Since both methods are compared to

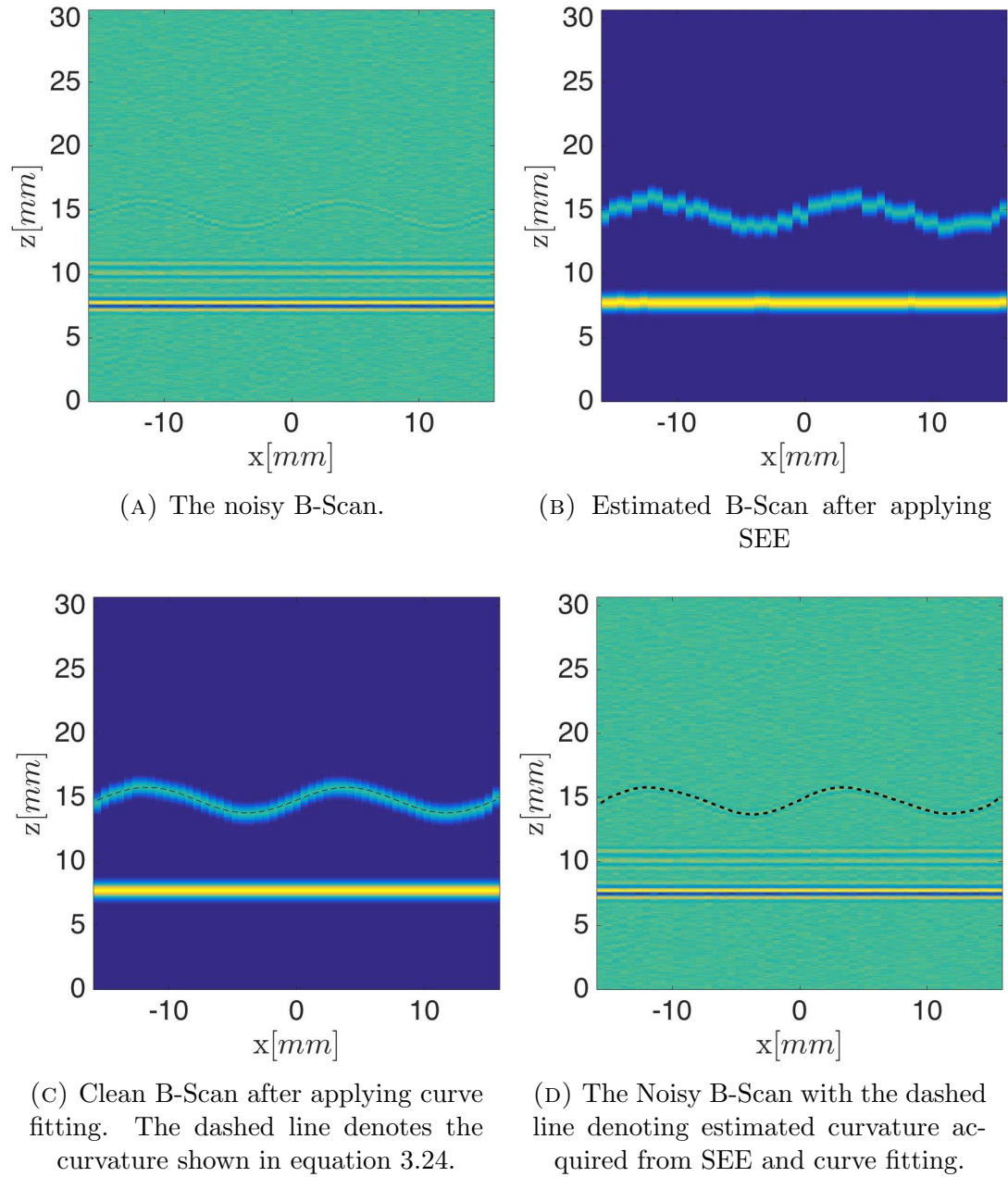


FIGURE 3.17: Processing a noisy B-Scan with convoluted Gaussian noise corresponding to $12dB/sample$ SNR in each reflectivity function and added Gaussian noise resulting to $12dB/sample$ SNR in each A-Scan.

the original curve from simulations, z is the same from both cases and is shown in equation 3.24.

TABLE 3.1: Accuracy of detection method with SEE vs with SEE and curve fitting

	SEE		SEE and curve fitting	
	Δz	Δz_λ	Δz	Δz_λ
$\eta_1 = \eta_2 = 0$	0.18 \pm 0.11	0.29 \pm 0.18	0.08 \pm 0.07	0.14 \pm 0.11
$20 \log \left(\frac{P(x^*h)}{P(\eta_2)} \right) = 12$	0.19 \pm 0.12	0.32 \pm 0.20	0.08 \pm 0.07	0.13 \pm 0.11
$20 \log \left(\frac{P(x^*h)}{P(\eta_2)} \right) = 6$	0.18 \pm 0.11	0.31 \pm 0.18	0.09 \pm 0.07	0.15 \pm 0.11
$20 \log \left(\frac{P(h)}{P(\eta_1)} \right) = 12$	0.20 \pm 0.11	0.33 \pm 0.18	0.08 \pm 0.06	0.14 \pm 0.09
$20 \log \left(\frac{P(h)}{P(\eta_1)} \right) = 6$	0.17 \pm 0.10	0.28 \pm 0.17	0.11 \pm 0.07	0.18 \pm 0.12
$20 \log \left(\frac{P(h)}{P(\eta_1)} \right) = 12$ and $20 \log \left(\frac{P(x^*(h+\eta_1))}{P(\eta_2)} \right) = 12$	0.19 \pm 0.12	0.33 \pm 0.19	0.11 \pm 0.07	0.18 \pm 0.12

Results of the accuracy of data acquired from SEE versus from SEE in addition to curve fitting are shown in Table 3.1. Results show that the accuracy of SEE is consistent regardless of the type of noise and noise level applied to the B-Scan. The accuracy of SEE is $0.19 \pm 0.11[mm]$ or $0.31\lambda \pm 0.18\lambda$. The accuracy is increased to $0.09 \pm 0.07[mm]$ or $0.15\lambda \pm 0.11\lambda$ after applying the curve fitting algorithm. With an accuracy well below one wavelength of sound in the target medium, and given the types of noise and noise levels applied to the original B-Scans in simulations, SEE proves to be a promising Algorithm for accurate human skull profile extraction.

3.3 Using SEE to determine the attenuation coefficient of the skull.

One of the parameters used to determine the curvature of the skull in SEE is the attenuation coefficient. This parameter is very important to produce accurate results and must be chosen to be as close to the actual value as possible. Selecting an attenuation coefficient that is inaccurate will result in no detection of the second peak or a measurement of an outlier. This disadvantage can be harnessed to determine the attenuation coefficient using SEE. Mainly, by varying the attenuation coefficient value and recording the behavior of SEE, the optimal attenuation coefficient value can be determined. There are two measurements of the behavior of SEE when applied to a B-Scan that can be used for this purpose: the number of detected points and the continuity of the detected curvature. The number of detected points at the various attenuation coefficient values gives a good estimation of the attenuation coefficient since at more accurate attenuation coefficient values more points are detected. However, the number of points is not enough to determine the attenuation coefficient since it accounts only for the number of peaks detected and not the detection accuracy. To determine the detection accuracy, a

measurement of continuity of the curvature of the second boundary is suggested to be made. The measurement of continuity is performed through the following process:

Given that SEE detected N_p points and that the location of the detected points are $x_p(n)$ and $y_p(n)$, where $n = 1, 2, \dots, N_p$, then:

$$\beta(k-1) = \left| \frac{y_p(k) - y_p(k-1)}{x_p(k) - x_p(k-1)} \right|; k = 2, 3, \dots, N_p \quad (3.31)$$

$$C = \sqrt{\frac{1}{N_p - 1} \sum_{i=1}^{N_p-1} (\beta(i) - \bar{\beta})^2} \quad (3.32)$$

where β represents the absolute value of the slope between consecutive detected points, and C is the continuity factor. In continuous functions, the absolute value of the slope between consecutive points is the absolute value of the derivative at those points. Therefore, when an outlier is introduced to the continuous function, it can only increase the absolute value of the slope between consecutive points. Thus, considering the standard deviation of the absolute value of the slope between consecutive points is a good measure of the continuity of the function: as the function becomes more continuous, C decreases.

When the attenuation coefficient value is close or equal to the actual value, the curvature obtained from SEE will contain maximum number of detected points and a minimum value of C , therefore:

$$E(\alpha) = \frac{N_d(\alpha)}{C(\alpha)} \quad (3.33)$$

$$\alpha_{optimal} = \operatorname{argmax}(E(\alpha)) \quad (3.34)$$

where E is the effectiveness of the algorithm as a function of the attenuation coefficient, $N_d(\alpha)$ is the number of points detected by SEE at the attenuation coefficient value α , and $C(\alpha)$ is the continuity factor of the curvature obtained

Algorithm 2 Attenuation determiner using SEE**Input:** $y, F_c, BW, N, z_f, d, W, c_s, \rho_s, \alpha, d_{min}, d_{max}$ ▷ y : Normalized RF-line in time domain.▷ F_c, BW : The central frequency and bandwidth of the transducer [MHz]▷ N, z_f : The number of elements used to focus. and the focal distance [m]▷ d, W : The pitch and element size of the transducer [m]▷ c_s, ρ_s, α : The speed of sound [$\frac{m}{s}$], density [$\frac{kg}{m^3}$], and attenuation coefficient [$\frac{Np}{mMHz}$] of the skull▷ d_{min}, d_{max} : The minimum and maximum thicknesses of the skull.▷ $\alpha_{min}, \alpha_{max}$: The minimum and maximum attenuation coefficient values of the skull.**Output:** α_{opt} ▷ α_{opt} : The optimal attenuation coefficient value corresponding to the averaged attenuation coefficient value in the skull.

```

1: for  $\alpha = \alpha_{min} : \alpha_{max}$  do
2:   reset  $x_p$  and  $y_p$ 
3:   for  $i = 1 : M$  do
4:      $h_i = \text{SEE}(\text{Bscan}(i), F_c, BW, N, z_f, d, W, c_s, \rho_s, \alpha, d_{min}, d_{max})$ 
5:     if  $h_i$  contains a boundary then
6:        $x_p = [x_p (i - \frac{M-1}{2})p]$ 
7:        $y_p = [y_p \text{find}(0 < h < 1)]$ 
8:     end if
9:   end for
10:   $N_p = \text{length}(x_p)$ 
11:   $\beta = \left| \frac{dy_p}{dx_p} \right|$ 
12:   $C = \sqrt{\frac{1}{M-2} \sum_{k=1}^{M-1} (\beta(k) - \bar{\beta})^2}$ 
13:   $E = [E \frac{N_p}{C}]$ 
14: end for
15:  $\alpha_{opt} = \text{argmax}(E')$ 

```

from SEE at the attenuation coefficient value α . The optimal value of attenuation coefficient $\alpha_{optimal}$ is when the ratio is maximized.

The process proposed to determine the attenuation coefficient is shown in Algorithm 2. In this algorithm, a for loop is conducted in line 1 to vary the value of the attenuation coefficient. In every iteration, SEE is applied to each A-Scan using a second loop as shown in line 3 and 4. In every iteration in the second loop, a condition is used to determine whether SEE has detected a boundary as shown in line 5; if it did, the coordinates of the second peak are recorded in lines

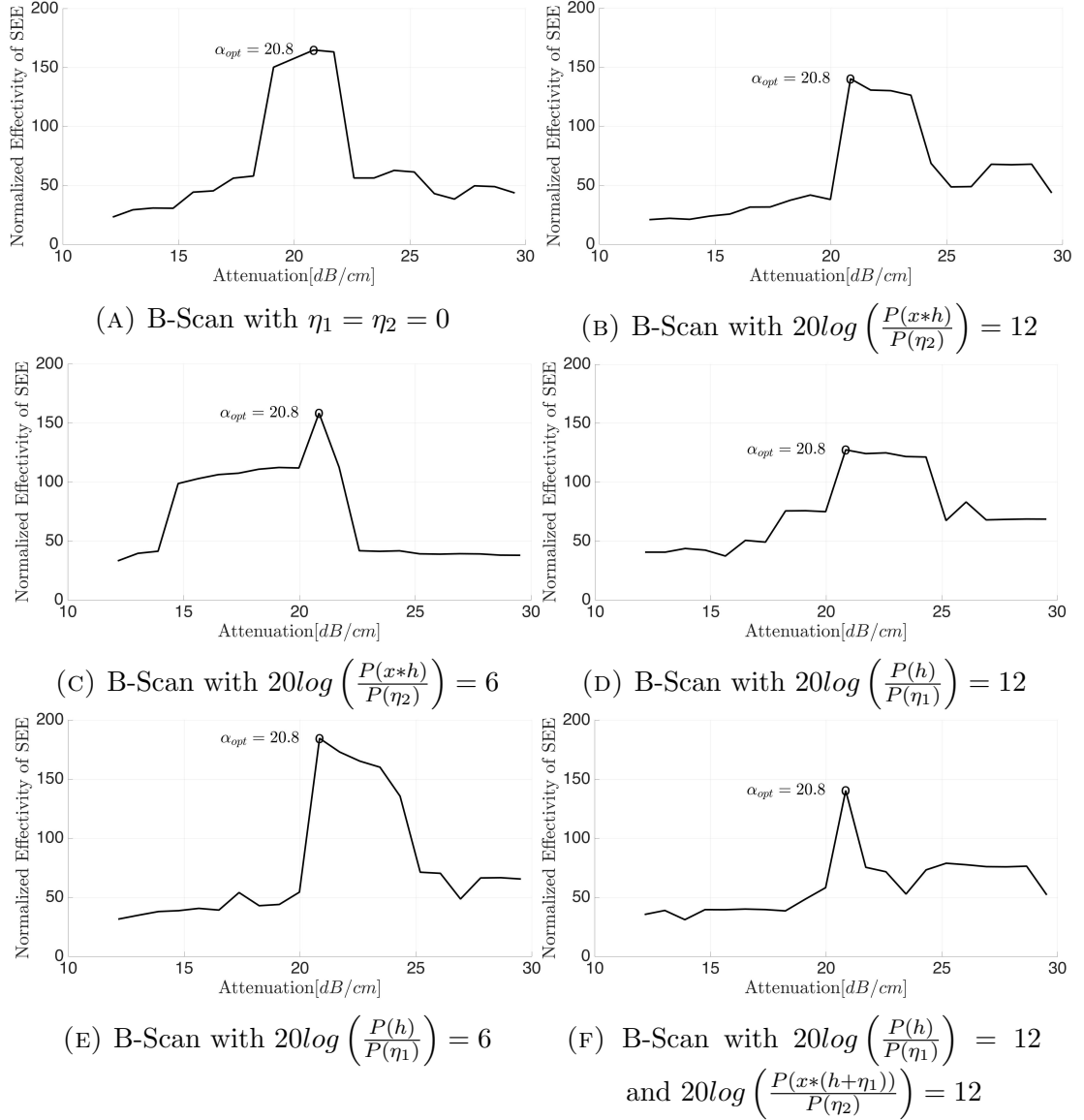


FIGURE 3.18: Testing Algorithm 2 for different types of B-Scans to determine the optimal attenuation coefficient value. In each sub figure, the y axis represents the effectiveness E as discussed in equations 3.33 and the x axis represents attenuation coefficient

7 and 7. After all points are detected, N_p is determined in line 10 as the length of the vector containing the x location of the points. β is calculated as the absolute value in the change in y_p with respect to the change in x_p as shown in Line 11. C is calculated to be the standard deviation of β as shown in line 12. Finally, the effectiveness of the algorithm in terms of the attenuation coefficient is calculated to be $\frac{N_d}{C}$ as shown in line 13.

The B-Scans discussed in Section 3.2 are used to test the effectiveness of Algorithm 2. The B-Scans are all constructed with the same base B-Scan built with an attenuation coefficient value of $\alpha = 20.8dB/cm$. The B-Scans experience different noise types and noise levels, thus, the B-Scans are an appropriate choice to test the algorithm. Figure 3.18 shows the effectiveness value as a function of attenuation coefficients from different B-Scans. In all the B-Scans, α_{opt} is consistently determined to be $20.8dB/cm$ proving the effectiveness of this modality.

3.4 Conclusion

Details of the proposed method for skull profile extraction via a post-processing adaptive-filtering algorithm, referred to as the Selective Echo Extraction algorithm (SEE) were discussed in Chapter 3. It was previously shown in Section 2.2 that the point spread function in biological tissues is spatially dependent; therefore, the averaged PSF from an entire B-Scan is not equal to the PSF from spatially localized segments of the B-Scan. In this case, processing the B-scan as a whole may lead to inaccuracy in the deconvolved signal; corresponding to the reflectivity function of the target media, and consequently inconclusive results. To avoid the effects of a spatially dependent PSF, the proposed method is based on independently processing A-Scans in a given skull profile B-scan. SEE is a blind algorithm in the sense it does not need previous information about PSF to process an A-Scan. The input requirements for SEE are limited to the acquisition system specifications and a rough estimate of major acoustical properties of the skull, as the target medium in this study.

When SEE is applied to an A-Scan, it extracts the portions which represent the innermost and the outermost boundaries of the skull by minimizing an error function as explained in section 3.1. The algorithm proposes various solutions to the A-Scan and compares each solution to the original A-Scan to produce an error

value. The correct solution results in a minimal error value and contains accurate locations of the innermost and outermost boundaries of the skull.

Results from simulations show that the algorithm is effective for noiseless A-Scan as well as A-Scans with the following types of noise and noise levels: additive noise $\approx 6dB/sample$ and $\approx 12dB/sample$ SNR in the A-scan, convoluted noise $\approx 6dB/sample$ and $\approx 12dB/sample$ SNR in the reflectivity function, and convoluted noise $\approx 12dB/sample$ SNR in the reflectivity function combined with additive noise $\approx 12dB/sample$ SNR in the A-Scan. The algorithm detects the innermost boundary of the skull to an accuracy of $0.23\lambda \pm 0.20\lambda$ or $0.14 \pm 0.12mm$.

When applied to skull profile B-Scans the algorithm proves effective for the same types of noise with an accuracy of $0.31\lambda \pm 0.18\lambda$ or $0.19 \pm 0.11mm$. A custom-designed curve fitting algorithm is used to further enhance the accuracy of the results and produce a continuous skull profile. The curve fitting algorithm is performed in three steps: results from SEE are divided into small segments, simple polynomial curve fitting is applied to each segment, then the results from all segments are combined to produce one skull profile. The application of curve fitting for the same simulated B-Scans result in an accuracy of $0.15\lambda \pm 0.11\lambda$ or $0.09 \pm 0.07mm$.

Another application of SEE is shown in section 3.3 which discusses how SEE can be used to determine the attenuation coefficient of the skull. Determination of the attenuation coefficient can be done by observing the effectiveness of SEE at different attenuation coefficient values: SEE is most effective when the attenuation coefficient value is closest to the actual value. The effectiveness of SEE can be calculated by maximizing the number of detected points and minimizing the discontinuity of the produced curvature.

The proposed attenuation coefficient estimation algorithm is applied to B-Scans with varying noise types and noise levels. The attenuation coefficients are consistently found to be equal to the actual attenuation coefficient values proving the

effectiveness of the algorithm. Skull profile extraction results and the attenuation coefficient estimation results discussed in this chapter showed great potential of the proposed method for accurate skull profile extraction. In chapter 4, experimental verification of SEE is presented.

Chapter 4

Experiments and results

To perform brain imaging through the skull, researchers have proposed a variety of methods to accommodate for the skull's distortive effects and topography. In some cases, such as adaptive beamforming methods [16–27], transcranial imaging requires an accurate measurement of the skull's profile. In Chapter 3, a novel signal processing algorithm capable of extracting the curvature of the skull using transducer's specifications and a rough estimate of the skull's acoustical properties was discussed. The algorithm uses the aforementioned parameters to numerically find the optimal location of the second boundary of the skull. In addition to finding the curvature of the skull, SEE can be used to find the average attenuation coefficient of the skull. The purpose of this chapter is to test SEE on adult human skull mimicking phantoms of known curvature to draw conclusions on the effectiveness of the algorithm in experiments.

The chapter is divided into three sections. Section 4.1 shows the experimental setup, the design and properties of the skull phantoms used for testing, the specifications of the transducer, and the specifications of the data acquisition system. Section 4.2 discusses the experimental data, the process used to obtain the skull profile, and the final results. Finally, Section 4.3, discusses the accuracy of the method and draws conclusions to the effectiveness of SEE in experiments.

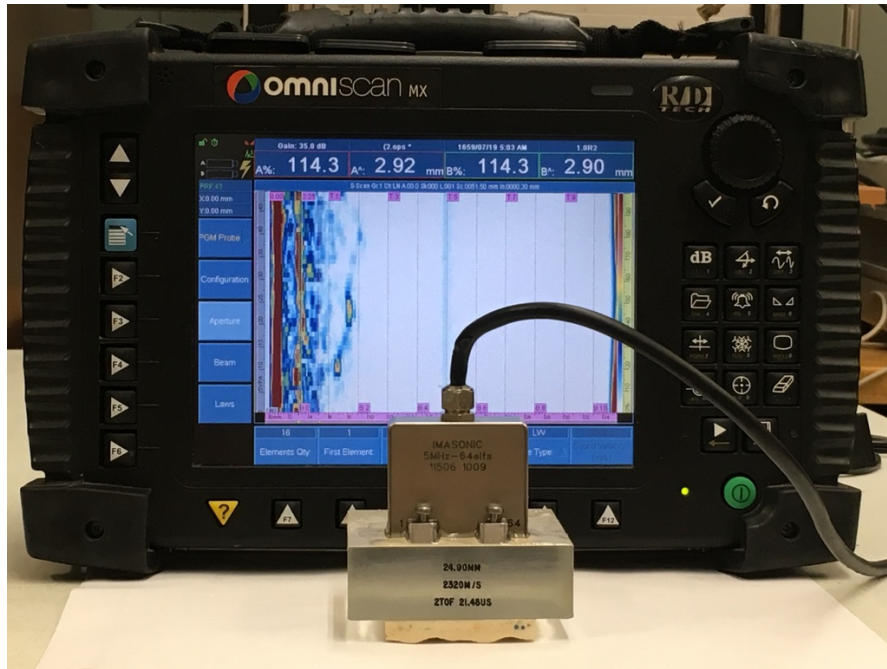


FIGURE 4.1: Experimental Setup showing OmniScan acquisition system, 64 element 5MHz IMASONIC linear phased array, delay line, and a skull phantom

4.1 Experimental setup

The experimental setup used to test SEE is composed of a data acquisition system, OmniScan MX, a 5 MHz IMASONIC transducer array, a delay line with known acoustical properties, and the sample as shown in figure 4.1. The data acquisition system is used to drive the transducer elements separately and collect data. The samples used in this setup are skull phantoms which mimic the acoustical properties of the human skull. The above major elements are discussed in the following sub-sections.

4.1.1 The human skull mimicking phantoms

In order to test SEE in experiments, skull phantoms of known curvatures and acoustic properties are designed, ordered, and tested. The skull phantoms were

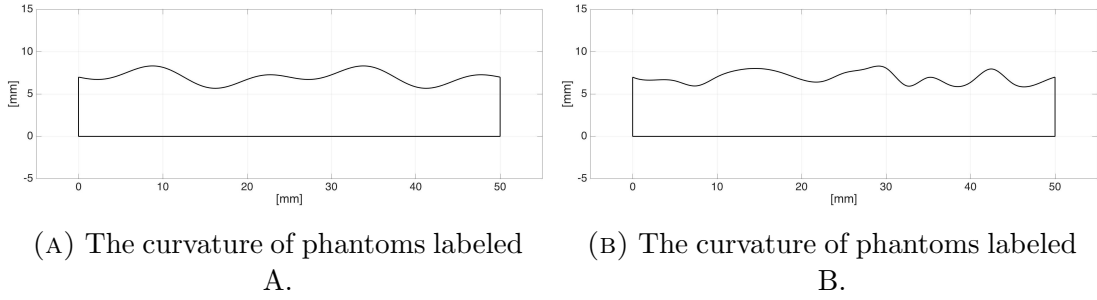


FIGURE 4.2: Skull Phantom Curvatures.

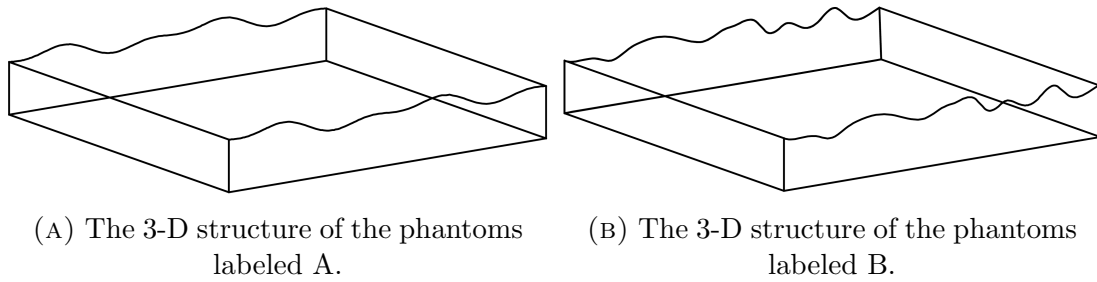


FIGURE 4.3: 3-D Skull Phantom structure.

designed using the softwares MATLAB[62] and AutoCAD [63] to create 3-D objects that are used to 3-D print a mold for production. Two types of curvature were designed and six phantoms were ordered from the manufacturer, True Phantom Solutions, exhibiting varying attenuation coefficient values. The materials used for production are thoroughly discussed in [60, 64]. The acoustical properties of the materials are outstandingly similar to human skull properties making the skull phantoms a perfect fit for testing in the laboratory before advancing to *in-vivo* clinical studies.

The phantoms are labeled either A or B to denote their curvature, and 1,2, or 3 to denote their diploe layer's thicknesses as 1mm, 2mm, or 3mm thick, respectively. The dimensions of the phantoms are 5cm by 5cm by 0.7cm. The innermost boundary of the phantoms labeled A have a sinusoidal form as follows:

$$y_A = 7 + 0.75\sin\left(\frac{4\pi}{50}x\right) - 0.50\sin\left(\frac{2\pi}{50}x\right) \quad (4.1)$$

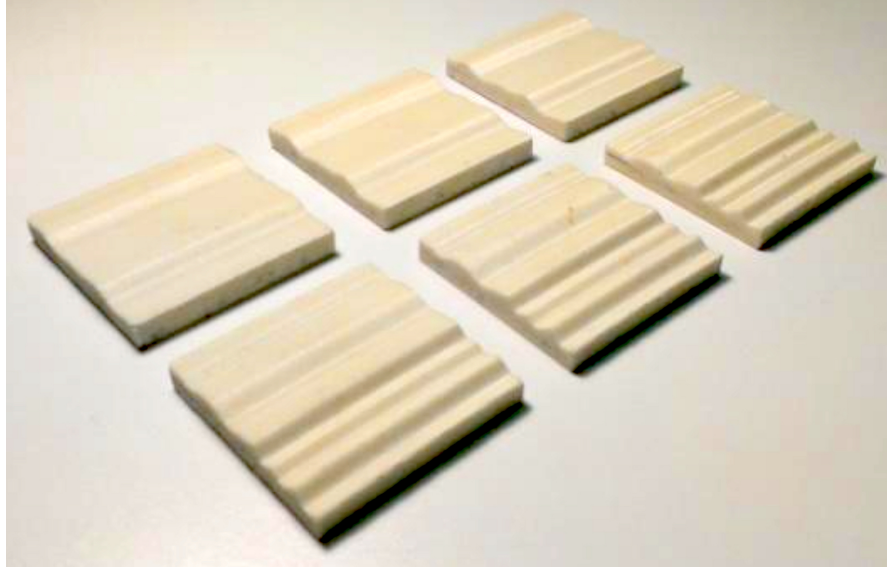


FIGURE 4.4: Human Skull mimicking phantoms

TABLE 4.1: Properties of phantom bone materials

Bone phantom type	Sound speed[m/s]	Density [g/m^3]	Attenuation at 5MHz in dB/cm
Cortical bone	3050 \pm 20	2.31	14.2 \pm 0.7
Trabecular bone	2800 \pm 50	2.03	47 \pm 4

where all the units are in mm . Alternatively, the innermost boundary of the phantoms labeled B is generated from a set of random points which are curve fitted to produce a randomized profile. The curvature for phantoms labeled A and phantoms labeled B are shown in Figure 4.2. The two curvatures created in MATLAB are exported to AutoCAD and a 3-D model is created and sent to the manufacturer for production. The models are shown in figure 4.3.

The final product received from True Phantom Solutions is shown in figure 4.4. The acoustical properties of the materials are shown in table 4.1, and the specifications of the phantoms are shown in table 4.2. Uniqueness of these phantoms can be realized by comparing their acoustical properties with human skull's *in-vivo* or *ex-vivo* measured counterparts reported in the literature [65–69].

TABLE 4.2: Properties of the phantoms

Sample	Average thickness [mm]	Diploe Thickness [mm]	Attenuation at 5MHz in dB/cm
A1	6.7 \pm 0.7	1.0 \pm 0.5	19 \pm 3
A2	6.2 \pm 0.7	2.0 \pm 0.5	25 \pm 3
A3	6.3 \pm 0.7	3.0 \pm 0.5	30 \pm 4
B1	6.9 \pm 0.7	1.0 \pm 0.5	19 \pm 3
B2	6.4 \pm 0.7	2.0 \pm 0.5	24 \pm 3
B3	6.2 \pm 0.7	3.0 \pm 0.5	30 \pm 4

4.1.2 The IMASONIC array transducer

The transducer used in this setup is a 64 element IMASONIC linear phased array with a central frequency of 5 MHz \pm 10% and a $-6dB$ bandwidth \geq 60%. The transducer has a pitch of 0.6mm and element size of 0.5mm \times 10mm. The traducer's matching layer is water coupled with acoustic impedance of 1.5 MRayl.

To avoid distortive reverberation effects at the surface of the transducer, a delay line was used as a buffer between the transducer's surface and the phantom. The delay line had a speed of sound of 2320m/s and was 24.90mm thick.

4.1.3 The data acquisition system

OmniScan system was used for data acquisition in the experiments. The system is portable, with 25 MHz sampling rate and 16 channels. The number of channels allow the system to excite and beamform using up to 16 elements of the transducer at a time. The number of elements used for focusing was chosen to be 12 element; having a larger number of elements results in higher imaging quality at the trade

of number of scanning area. Number of A-Scans that can be acquired are:

$$M = N_{app} - N_{subapp} + 1 \quad (4.2)$$

where M is the number of A-Scans, N_{app} is the number of elements in the transducer, and N_{subapp} is the number of elements used for focusing. In this setup, $N_{app} = 64$ therefore choosing the maximum number of elements for focusing (16) will result in only 49 A-Scans and a scanning area of $29.4mm$. Choosing $N_{subapp} = 12$ increases the number of A-Scans to 53 and the scanning area to $31.8mm$ while maintaining similar image quality.

The speed of sound of the delay line as well as the thickness of it were specified in the system to insure data acquisition is performed with the correct initial delay.

For the purpose of this study, no digital filters are applied to the A-Scans through the system and gain is kept at zero to insure external effects on the A-Scans are minimal and the attenuation calculations are conclusive.

The experiments were carried out by coupling the transducer to the delay line and the delay line to each sample using ultrasonic coupling gel. The data was then transferred to and processed in MATLAB on a PC.

4.2 Experimental Data and Results

Using the setup discussed in section 4.1 B-Scans are acquired from each phantom. Raw RF data from the experiments are shown in figure 4.5, where a faint innermost profile can be seen at $\approx 10mm$ in the y direction in every B-Scan. In order to process B-scans from different phantoms the following steps are taken:

1. SEE is used to determine the average attenuation coefficient of the phantom.

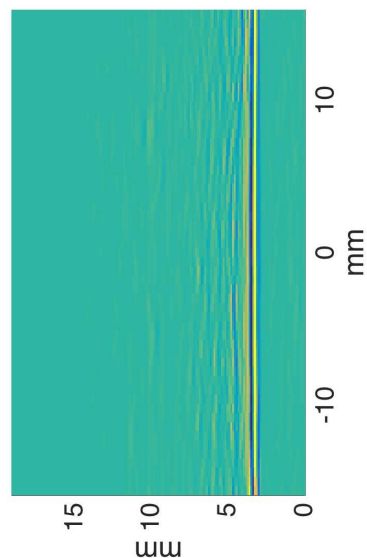
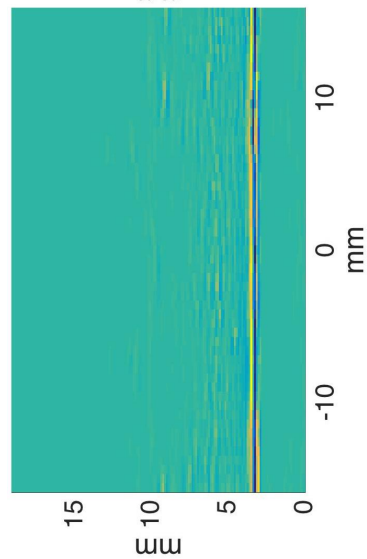
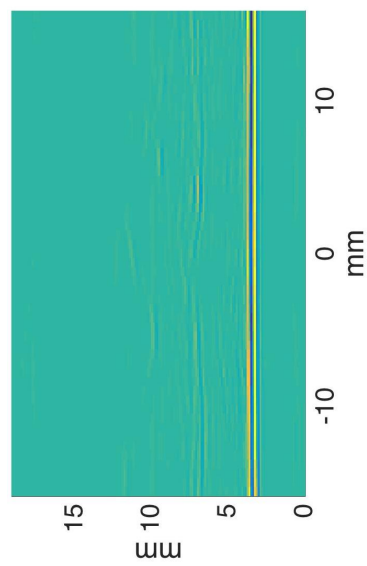
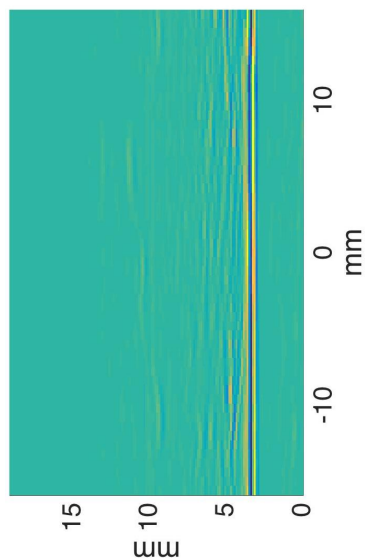
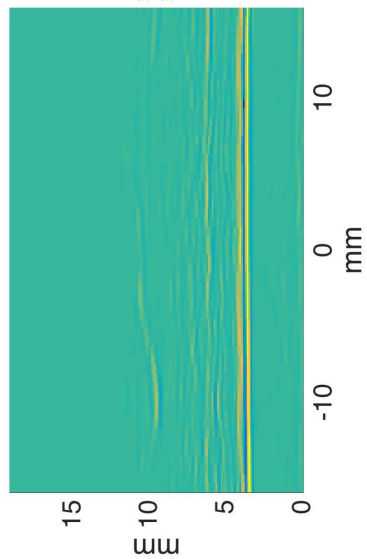
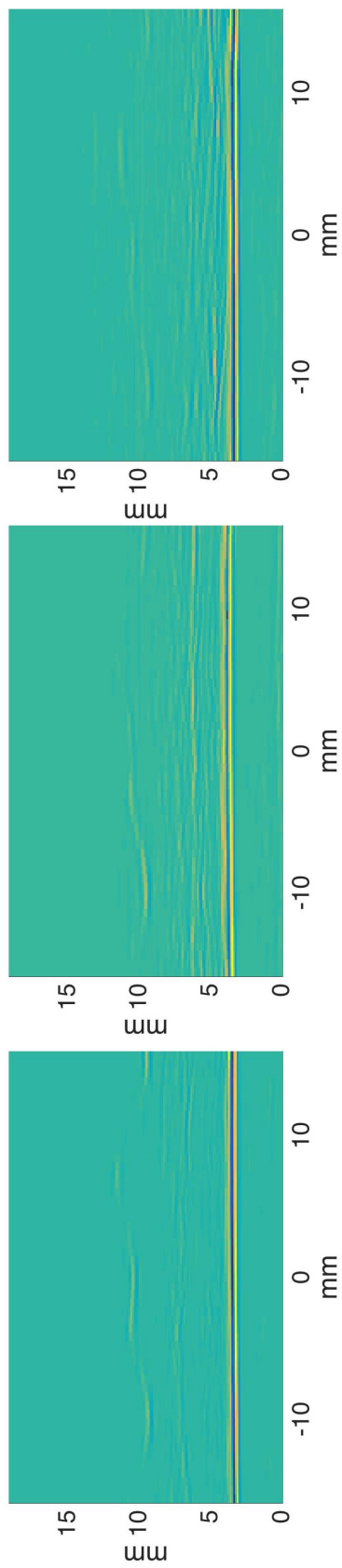


FIGURE 4.5: The raw B-Scans acquired from the acquisition system

2. SEE is used to extract points from the innermost and boundaries of the skull.
3. The custom-designed curve fitting method is used to process results from SEE and produce a continuous curvature.

In section 3.3, an algorithm was proposed to determine the attenuation coefficient of the skull. Algorithm 2 showed great results for simulations, however, since the skull is not an ideal medium, two additions were made to the algorithm to make it compatible with experiments. The changes are shown in Algorithm 3 and are explained below.

It is important to note that in experimentations, some reflections caused by impurities in the skull or reverberation from diploe occur around the area of the innermost boundary of the skull that behave similarly to the actual innermost boundary's reflections. Those reflections are sometimes detected by SEE instead of the actual boundary and are considered outliers that must be eliminated before calculating the Effectivity of SEE for the specified attenuation coefficient value.

The first addition to Algorithm 2 involves a process for removing outliers. In Algorithm 3, lines 11 to 17 discuss the steps taken to remove the outliers. In line 11, the rate of change of the detected skull curvature is calculated and noted as y'_p . In line 12, the custom curve fitting function discussed in section 3.2 is used to curve fit the points acquired from SEE. Since the outliers have a low chance of existing in the curve fitted data, then the curve fitted data value at an outlier's location must vary greatly from the SEE results. This is shown in lines 14 to 16 which state that if the difference of the curve fitted data and SEE data is higher than the acceptable range denoted by the standard deviation of the rate of change in SEE, then an outlier exists and is removed. The Effectivity factor of SEE at each attenuation value is calculated as discussed in section 3.3. The Effectivity factor shows the number of peaks detected by SEE and their continuity, mainly:

Algorithm 3 Attenuation determination algorithm using SEE with the removal of outliers

Input: $y, F_c, BW, N, z_f, d, W, c_s, \rho_s, \alpha, d_{min}, d_{max}$

▷ y : Normalized RF-line in time domain.

▷ F_c, BW : The central frequency and bandwidth of the transducer [MHz]

▷ N, z_f : The number of elements used to focus. and the focal distance [m]

▷ d, W : The pitch and element size of the transducer [m]

▷ c_s, ρ_s, α : The speed of sound $[\frac{m}{s}]$, density $[\frac{kg}{m^3}]$, and attenuation coefficient $[\frac{Np}{mMHz}]$ of the skull

▷ d_{min}, d_{max} : The minimum and maximum thicknesses of the skull.

Output: α_{opt}

▷ α_{opt} : The optimal attenuation coefficient value corresponding to the averaged attenuation coefficient value in the skull.

```

1: M= length(Bscan)
2: for  $\alpha = \alpha_{min} : \alpha_{max}$  do
3:   reset  $x_p$  and  $y_p$ 
4:   for  $i = 1 : M$  do
5:      $h_i = \text{SEE}(\text{Bscan}(i), F_c, BW, N, z_f, d, W, c_s, \rho_s, \alpha, d_{min}, d_{max})$ 
6:     if  $h_i$  contains a boundary then
7:        $x_p = [x_p (i - \frac{M-1}{2})p]$ 
8:        $y_p = [y_p \text{find}(0 < h < 1)]$ 
9:     end if
10:  end for
11:   $y'_p = \frac{dy_p}{dx_p}$ 
12:   $y_f = \text{segfit}(x_p, y_p, M, p)$ 
13:  for  $(x_i, y_i)$  in  $(x_p, y_p)$  do
14:    if  $\frac{|y_f(x_i) - y_i|}{x_{i+1} - x_i} > \text{std}(y'_p)$  then
15:      remove  $x_i, y_i$  from  $x_p, y_p$ 
16:    end if
17:  end for
18:   $N_p = \text{length}(x_p)$ 
19:   $\beta = \left| \frac{dy_p}{dx_p} \right|$ 
20:   $C = \sqrt{\frac{1}{M-2} \sum_{k=1}^{M-1} (\beta(k) - \bar{\beta})^2}$ 
21:   $E = [E \frac{N_p}{C}]$ 
22: end for
23:  $E' = A(E)p(E)w(E)$ 
24:  $\alpha_{opt} = \text{argmax}(E')$ 

```

$$E = \frac{N_p}{C} \quad (4.3)$$

where N_p the number of detected points and C is the continuity factor.

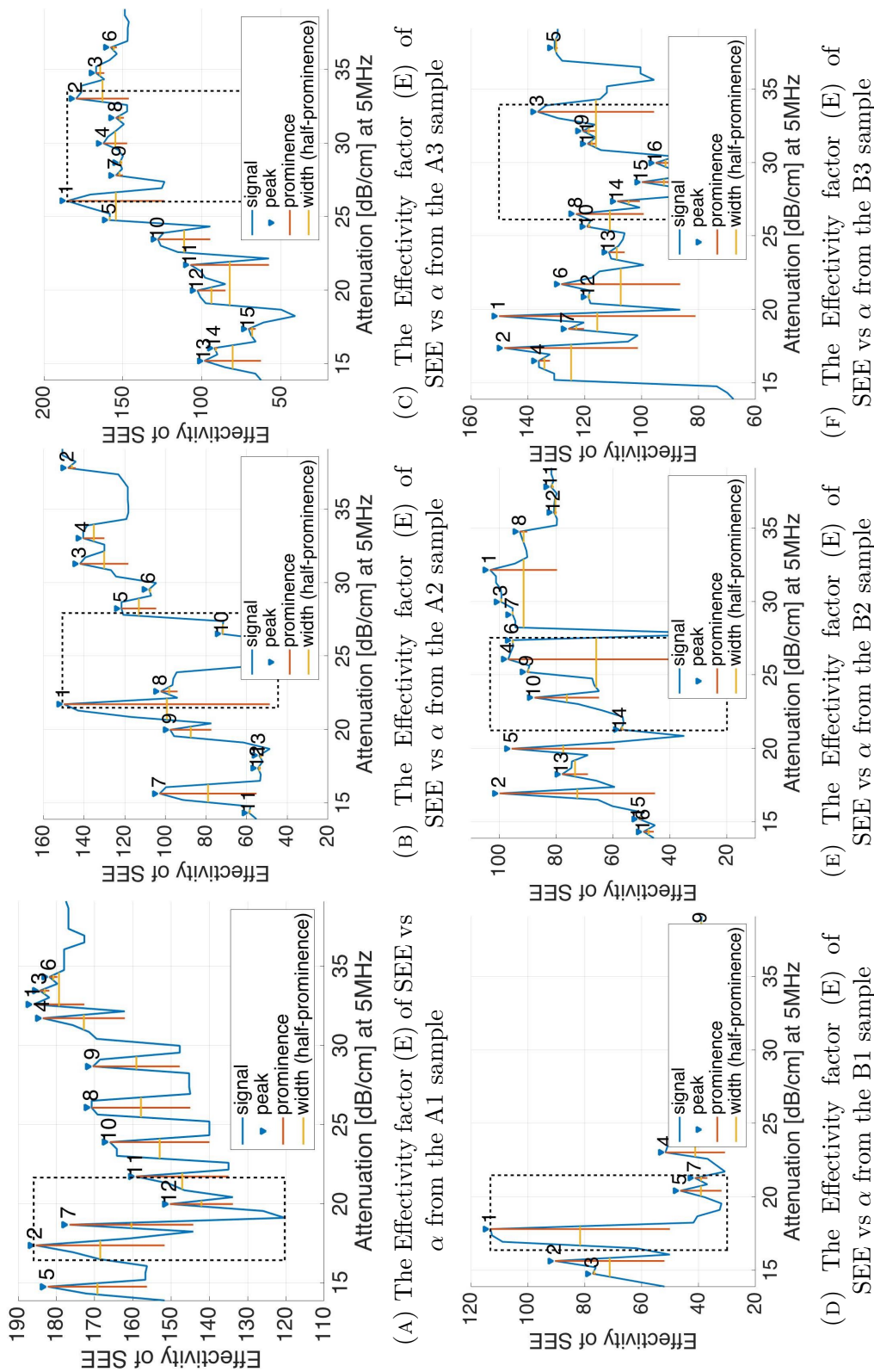


FIGURE 4.6: The Effectivity factor of SEE with respect to varying attenuation coefficient values acquired from raw B-Scans. The dashed box represents the actual attenuation coefficient value range for the specific phantom

At an optimal attenuation coefficient value, points acquired from SEE are postulated to be more continuous and larger in number than inaccurate attenuation coefficient value. In this chapter, the investigated attenuation coefficients range from $14dB/cm$ to $40dB/cm$ to cover all possible attenuation coefficient values that the phantoms may exhibit. The Effectivity calculated from the B-Scans are shown in figure 4.6. In each plot in figure 4.6, the dotted box encompasses the acceptable attenuation coefficient range which corresponds to the actual attenuation values shown in table 4.2. The peaks are each labeled in a descending order by height. The peaks' prominence and half prominence width are also shown in the plots.

In contrast with results from simulations shown in section 3.3, it is not enough to evaluate the peaks of the Effectivity function from their amplitude alone. To properly analyze the results from the algorithm, the peak amplitude, peak prominence, and peak width should be taken into account. A new Effectivity function is derived from the original Effectivity function as follows:

$$E'(\alpha) = A(E, \alpha)P(E, \alpha)W(E, \alpha) \quad (4.4)$$

where $A(E, \alpha)$, $P(E, \alpha)$, and $W(E, \alpha)$ are functions that extract the amplitude, prominence, and half prominence width of each peak in E , respectively. A maximum value of each peak, denoted by $A(E, \alpha)$ is now one of three factors considered in analyzing the peaks instead of being the only factor.

The prominence of the peaks, $P(E, \alpha)$, provides a depiction of how much the peak stands out due to its intrinsic height and its location relative to other peaks [62]. To illustrate the importance of prominence, consider peak 3 in figure 4.6a. This peak has a higher amplitude than most peaks in the Effectivity function, however, it is unlikely to represent the actual attenuation coefficient value since it is not very dominant compared to the points near it; where as peak 7 in the same figure has a higher chance of representing the actual value of attenuation since it dominates the region.

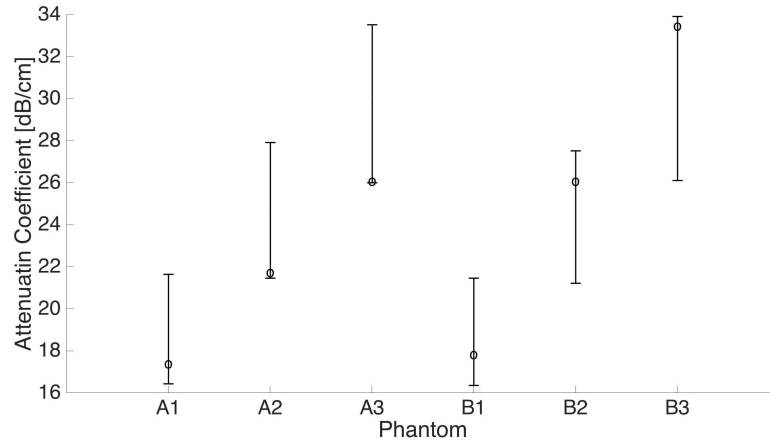


FIGURE 4.7: Attenuation coefficient value for each skull sample

Finally, the half prominence width of the peaks, $W(E, \alpha)$ will provide a final comparison between peaks with similar amplitude and prominence but different broadness: varying attenuation slightly should not change the Effectivity factor of SEE drastically, therefore, a peak with large width is more likely correlated to the actual attenuation coefficient value than a peak with small width. Results for calculated $E'(\alpha)$ for each phantom are shown in figure 4.8

Results in figure 4.8 show that the values of E' , which highlight the peaks' amplitude, prominence, high half prominence width, are much more distinctively related to the actual attenuation coefficient values than values of E . The values are more clearly seen in Figure 4.7 where they are shown to be found within error range of the actual attenuation coefficient values.

The attenuation coefficient values determined in the previous step are used to run SEE for each B-Scan. The values from SEE are then curve fitted using the custom curve fitting algorithm. Results from SEE and the curve fitting algorithm are plotted over the original B-Scans in figure 4.9 along side the original 3-D printed curvature.

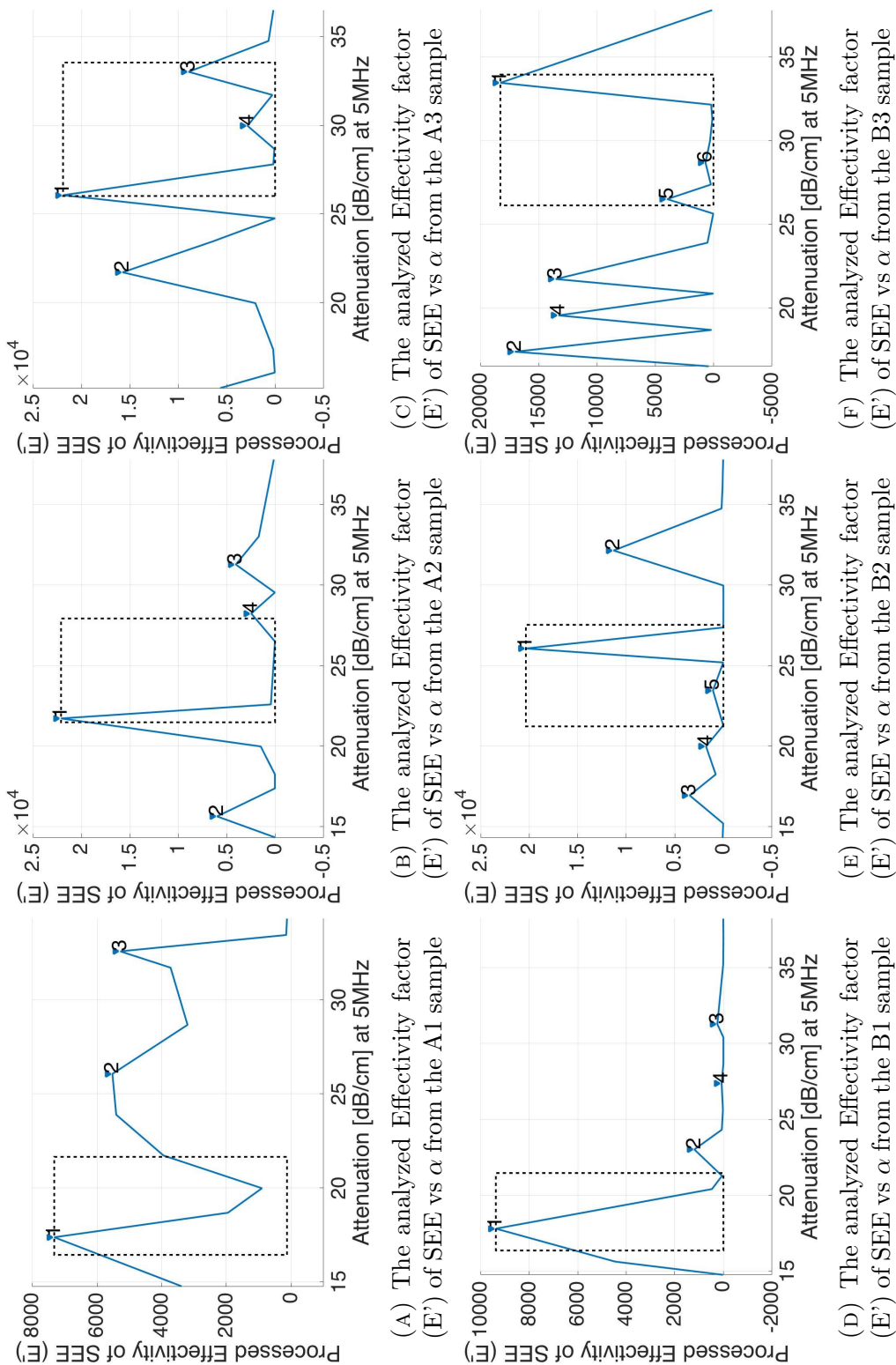
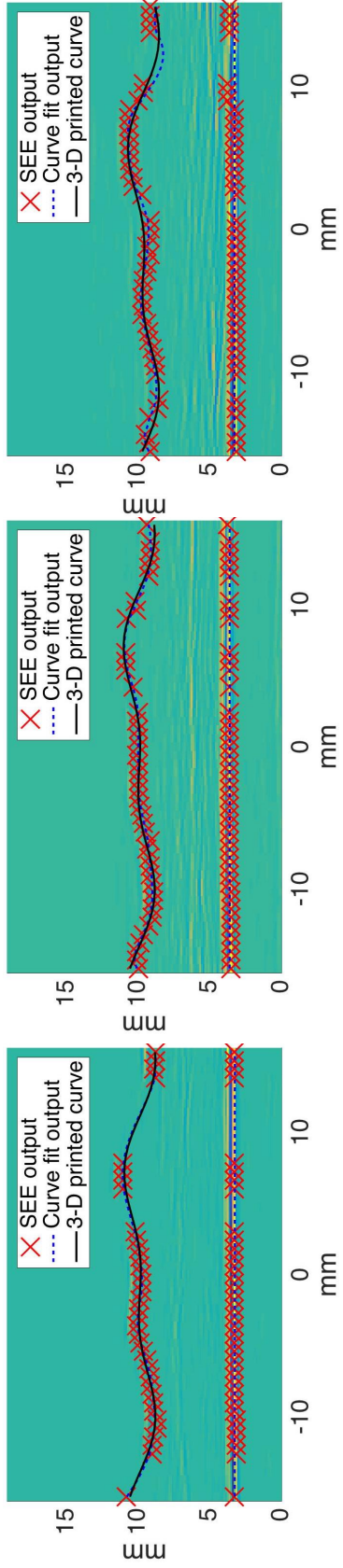
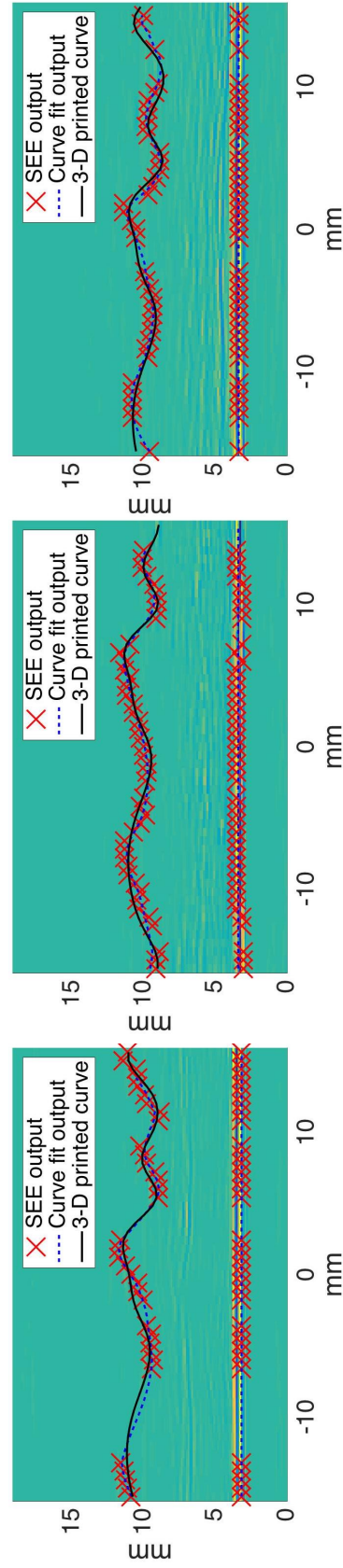


FIGURE 4.8: The analyzed Effectivity factor of SEE with respect to varying attenuation coefficient values acquired from raw B-Scans. The dashed box represents the actual attenuation coefficient value range for the specific phantom



(C) Processed B-Scan from phantom A3



(F) Processed B-Scan from phantom B3

FIGURE 4.9: The processed B-Scans using SEE and the custom curve fitting algorithm

Results from SEE show outstanding accuracy and continuity. Outliers do not exist in the final results since their detection is avoided inside the process of SEE as discussed in section 3.1 and they are tackled again outside SEE as shown in Algorithm 3. The empty sections in the B-Scans where no points are detected are present mostly in areas of high slope. In those areas, ultrasonic waves are reflected at a high angle causing no echo from the boundary to be present in the A-Scan, and therefore, they are not expected to be detected by SEE.

The plot from the curve fitted data is almost indistinguishable from the actual 3-D printed curve in most areas. The areas of the curve fitted data that are not perfectly aligned with the 3-D printed curve exist mostly in areas of high curvature and small number of detected points.

Figures 4.9a, 4.9b, and 4.9c show the results from the phantoms manufactured using the sinusoidal curve shown in equation 4.1 and figure 4.2a. Figure 4.9a shows the results from phantom A1 which contains $1mm$ diploe. This phantom contains 3 areas with no detected points. The missing points all exist in areas of high slope. Although SEE is unable to detect the points in that area, the curve fitting function fills in the space to an excellent quality since the points from SEE are detected to a high accuracy. Figure 4.9b shows the results from phantom A2 which contains $2mm$ diploe. Although this B-Scan is obtained from a sample with thicker diploe than the one in 4.9a, more points are detected by SEE. This is possible since diploe thickness is not the only factor in detection: other factors include the physical alignment of the probe with the sample and the quality of coupling. These factors vary from scan to scan and may result in more difficult phantoms to produce better data if aligned and coupled well. Figure 4.9c shows the results from phantom A3 which contains $3mm$ diploe. In this B-Scan, the area between $10mm$ and the end of the scan is not detected to a high accuracy. This might be caused by the slight inaccuracy of the last few detected points in the B-Scan. However, this inaccuracy is still insignificant since it is less than $0.5mm$.

Figures 4.9d, 4.9e, and 4.9f show the results from the phantoms manufactured using the randomized curvature shown in figure 4.2b. Figure 4.9d shows the results from the phantom B1 which contains $1mm$ diploe. The results from this phantom are the most inaccurate results in the set. Between $-13mm$ and $0mm$ the estimated curvature is continuously not consistent with the actual curvature and the flat region at $-3mm$ is not detected. Since the positive slopes in the profile are detected while negative slopes are not, the inaccuracy is most likely caused by the positioning of the probe. However, even with this inaccuracy, the results still meet the objective of the study. Figure 4.9e shows the results from phantom B2 which contains $2mm$ diploe. This phantom seems to be well aligned since many points are detected. However, reverberations from diploe layer may be affecting the results in the area from the beginning of the scan to $-10mm$. Finally, figure 4.9f shows the results from phantom B3 which contains $3mm$ diploe. This phantom is considered the most difficult phantom in the set since it contains the randomized curvature as well as thick diploe. Results from this phantom are still successful since the detected profile is within $0.5mm$ of the actual.

4.3 Discussion

Calculations of variation from the original data obtained in section 4.2 are performed similar to the calculations in section 3.2; i.e. results from SEE and results from curve fitting are compared to the original 3-D printed curvature as follows:

$$\Delta z = mean(|\hat{z} - z|) \quad (4.5)$$

$$\Delta z = std(|\hat{z} - z|) \quad (4.6)$$

where \hat{z} is the data obtained from the respective method and z is the original 3-D printed curvature. The results are also displayed as a ratio of the wavelength in

TABLE 4.3: Accuracy of detection method with SEE vs with SEE and curve fitting using experimental data

	SEE				SEE and curve fitting			
	Δz		Δz_λ		Δz		Δz_λ	
A1	0.08	± 0.06	0.14	± 0.10	0.07	± 0.05	0.12	± 0.08
A2	0.16	± 0.21	0.26	± 0.35	0.16	± 0.20	0.27	± 0.33
A3	0.19	± 0.15	0.32	± 0.26	0.20	± 0.13	0.33	± 0.22
B1	0.36	± 0.25	0.60	± 0.41	0.27	± 0.16	0.44	± 0.27
B2	0.24	± 0.18	0.40	± 0.30	0.21	± 0.15	0.35	± 0.25
B3	0.27	± 0.23	0.45	± 0.38	0.25	± 0.20	0.42	± 0.34

skull, $\Delta z_\lambda = \frac{\Delta z}{\lambda}$. Table 4.3 shows the results for all B-Scans.

The results show that although the transducer has a relatively low sampling rate compared to the central frequency and bandwidth, the profiles are detected to the desired accuracy. With SEE alone, the profiles are detected to be within $0.22 \pm 0.18mm$ or $0.36\lambda \pm 0.30\lambda$. After the curve fitting algorithm is applied, the profiles are detected to be within $0.19 \pm 0.15mm$ or $0.32\lambda \pm 0.25\lambda$. Although, in some cases, the curve fitting algorithm does not reduce the range as well as it did in simulations, it does however, interpolate the results in areas with no detected points to an outstanding accuracy.

Sources of error in the results stem from the experimental setup and the materials used. Highest error occurs from the positioning of the probe relative to the sample. Since the highest reflections occur at normal incidence, the more parallel the surface of the probe is to the sample, the more accurate the results. Another source of error stems from coupling the transducer to the delay line and the delay line to the sample. It is important that coupling is done properly and the coupling gel contains no air bubbles. It is assumed that for the scans presented in the previous section that the coupling is done successfully since an image is received in each scan. Other sources of error could rise from inaccuracy in the measured

acoustical properties of the skull and coupling medium used in the calculations. Those effects are minor except for the effect of the speed of sound. Since the speed of sound is the key property used to convert the units in the scans from temporal to spatial, inaccuracy in the speed of sound may cause the collective thickness of skull to be altered. For the purpose of this thesis, this effect is negligible since the properties of the phantoms are well known. Finally, the discretization of the received signal may cause slight variations in the results. The signal is sampled at a mere 25MHz, which is above the Nyquist frequency for the central frequency of 5MHz. With this sampling rate, the signal is segmented into 0.12mm sections, meaning the profile detection from SEE is limited to that accuracy.

Chapter 5

Conclusion

Medical Ultrasonic Imaging is an outstanding tool used by clinicians to image the body for diagnosis. Ultrasonic Imaging relies on the difference in acoustical properties in the target media to distinguish different types of tissue. This comes as a drawback when the imaging area of the body is covered by bone such as the brain. Bone tissue has significantly different acoustical properties than soft tissue causing a variety of distorting effects and limiting imaging in that area. Finding solutions for such limitation would bring tremendous benefits for trauma diagnosis and therefore has been a popular area of research in the ultrasonic imaging community.

Transcranial imaging has been a sought out application in ultrasound for decades. Many methods have been proposed over the years to accommodate for the skull's distortive effects and topography. In some cases, such as adaptive beamforming methods [16–27], transcranial imaging requires an accurate measurement of the skull's profile. The skull is composed of three layers, the innermost and outermost layers are composed of compact bone that can be considered a dense and homogeneous tissue. The middle layer, however, is composed of a highly porous and non-homogeneous material which causes scattering, phase aberration, and attenuation. Thus, conventional ultrasonic scans of human skull do not correlate directly to its actual structure.

A new post-processing technique referred to as the Selective Echo Extraction algorithm (SEE) has been developed and reported for accurate human skull profile extraction via ultrasonic phased arrays. The objective was to develop a technique applied to ultrasonic RF signals to accurately extract the curvature of the skull's inner boundary such that it lies within $\pm 0.5mm$ of the actual undulating thickness. The developed method can also be utilized to determine the averaged attenuation coefficient of the skull.

The proposed method is based on an adaptive filtering model. In order to extract the curvature of the skull from a B-Scan through SEE, each A-Scan is processed independently. Each A-Scan along with the transducer's specifications and a rough estimate of the major acoustical properties of the skull are input into SEE. The algorithm extracts the portions of the A-Scan which represents the innermost and the outermost boundaries of the skull by minimizing an error function as explained in section 3.1. The algorithm generates each value of the error function by proposing a solution to the A-Scan and comparing it to the original A-Scan. The solution, which produces a global minimum in the error function, is the correct estimation of the reflectivity function corresponding to the innermost and outermost boundaries. A custom-designed curve fitting algorithm was also developed to further enhance the accuracy of the results and produce a continuous skull profile. The curve fitting algorithm is performed in three steps: results from SEE are divided into small segments, simple polynomial curve fitting is applied to each segment, then the results from all segments are combined to produce a complete skull profile.

SEE can further be utilized to determine the attenuation coefficient of the skull using a secondary process. Since attenuation is a key factor for the accuracy of SEE, varying it will influence the results. By quantifying the accuracy of the results, SEE can be tested against different attenuation coefficient values to determine the one that most effectively produces accurate results. The attenuation value which

optimizes the results of SEE is postulated to be the actual attenuation coefficient value of the sample.

The proposed method is verified in simulations for single A-Scans with varying applied noise in section 3.1. It is also verified for skull curvature and attenuation coefficient determination in simulations in section 3.2 and section 3.3, respectively, and for skull curvature and attenuation detection in experiments in section 4.2.

Results from simulations show that the algorithm is effective for noiseless A-Scans as well as A-Scans with the following types of noise and noise levels: additive noise $\approx 6dB/sample$ and $\approx 12dB/sample$ SNR in the A-scan, convoluted noise $\approx 6dB/sample$ and $\approx 12dB/sample$ SNR in the reflectivity function, and convoluted noise $\approx 12dB/sample$ SNR in the reflectivity function combined with additive noise $\approx 12dB/sample$ SNR in the A-Scan. For single A-Scans, the algorithm detects the innermost boundary of the skull to an accuracy of $0.23\lambda \pm 0.20\lambda$ or $0.14 \pm 0.12mm$.

When applied to simulated skull profile B-Scans with an attenuation coefficient of $20.8dB/cm$ at 5MHz, the algorithm proves effective for the same types of noise mentioned above with an accuracy of $0.31\lambda \pm 0.18\lambda$ or $0.19 \pm 0.11mm$. The application of curve fitting for the same simulated B-Scans results in an accuracy of $0.15\lambda \pm 0.11\lambda$ or $0.09 \pm 0.07mm$. The noisy B-Scans are further used to verify the attenuation determination algorithm. The results are shown to converge to a value of $20.8dB/cm$ in every simulation.

The experimental setup used for verification was composed of the data acquisition system, OmniScan, a 5MHz 64-element IMASONIC linear phased array, a delay line, and custom ordered skull phantoms. The phantoms were made using two known curvatures which were 3-D printed into molds and used for precise manufacturing the phantoms.

In general, the proposed process to determine the skull's curvature from a B-Scan is comprised of three major steps. In the first step, the attenuation coefficient determination algorithm is used to find the attenuation coefficient of the skull. This value as well as each A-scan extracted from the B-Scan are inputted into SEE to produce two measurements that show the skin/skull boundary and the skull/brain boundary. The results are then curve fitted using a customized method to show a smooth curvature representing the inner compact bone boundary. It is worth noting that the original attenuation determination algorithm discussed in section 3.3 was further enhanced for better accuracy in the experiments. Enhancing the algorithm included adding a portion to remove outliers and considering more factors in the Effectivity function.

Results from experiments show that the attenuation coefficients of the phantoms are determined within the error range and the curvatures of the phantoms are detected to a better accuracy than proposed in the objectives of this thesis in section 1.6. The attenuation coefficient values are found to be within 9.6% of the actual attenuation values. With SEE alone, the curvatures are detected to be within $0.36\lambda \pm 0.30\lambda$ or $0.22 \pm 0.18mm$. After the curve fitting algorithm is applied, the curvatures are detected to be within $0.32\lambda \pm 0.25\lambda$ or $0.19 \pm 0.15mm$. Although the curve fitting algorithm does not reduce the range in experiments as well as it did in simulations, it does however, interpolate the results in areas with no detected points to an outstanding accuracy.

Sources of error in the experiments stem mostly from the experimental setup and instrumentation. Major error in the results is caused by the misalignment of the probe with the phantoms. This misalignment might cause maxima and minima of the phantom to not be detected to a high accuracy, thus, altering the results from curve fitting. Another source of error is caused by imperfections in coupling of the array to the delay line and the delay line to the sample. However, this source of error had negligible impact on the reported results in this study. The sampling frequency on the acquisition system is also a limitation to the observed data.

The sampling frequency was limited to 25MHz for the 5 MHz probe used in the experiments. This means the A-Scans are segmented to 0.12mm sections, limiting the resolution of acquisition. Ideally, the sampling frequency is much higher. Finally, the estimation of the acoustical properties of the media that are input to SEE can contribute to errors in the results. The density of the media will have minimal effects since it is not a major contributor to the equations determining the error function in SEE. However, variations in the speed of sound can cause the highest amount of error in the results. The speed of sound in the skull is used to convert the scaling in the A-Scan from time-based to spatially-based. Therefore, variations in the speed of sound will change the total thickness of the probed area. This source of error has been avoided in the thesis, since the speed of sound in the phantoms is well known but has to be further investigated for other applications.

In conclusion, the reported results from both simulations and experiments show that the proposed Selective Echo Extraction algorithm (SEE) is highly effective for human skull attenuation coefficient estimation and accurate profile extraction.

Recommendations for future work include further testing the algorithm's applicability with varying probe frequencies and bandwidths. Applying this method for C-Scans obtained from matrix array and 3-D skull phantoms; and finally, incorporating this method with *in-vivo* applications in transcranial imaging.

Bibliography

- [1] C. Guy and D. Flytche, *An introduction to the principles of medical imaging*. Imperial Coll., 1976.
- [2] E. N. Marieb, P. B. Wilhelm, and J. Mallatt, *Human anatomy*. Pearson, 2014.
- [3] A. Zaknich, *Principles of adaptive filters and self-learning systems*. Springer Science & Business Media, 2006.
- [4] R. S. Cobbold, *Foundations of biomedical ultrasound*. Oxford University Press, 2006.
- [5] W. C. Röntgen, “On a new kind of rays,” *Science*, pp. 227–231, 1896.
- [6] O. College, *Anatomy & Physiology*. OpenStax College, April 2013.
- [7] M. De Vlieger, “Evolution of echo-encephalography in neurology—a review,” *Ultrasonics*, vol. 5, no. 2, pp. 91–97, 1967.
- [8] D. Phillips, S. Smith, O. Von Ramm, and F. Thurstone, “Sampled aperture techniques applied to b-mode echoencephalography,” in *Acoustical Holography*, pp. 103–120, Springer, 1975.
- [9] S. Smith, D. Phillips, O. Von Ramm, and F. Thurstone, “Some advances in acoustic imaging through the skull,” *Ultrasonic tissue characterization II*, vol. 525, pp. 209–218, 1979.

-
- [10] U. Bogdahn, G. Becker, J. Winkler, K. Greiner, J. Perez, and B. Meurers, "Transcranial color-coded real-time sonography in adults.," *Stroke*, vol. 21, no. 12, pp. 1680–1688, 1990.
- [11] N. M. Ivancevich, J. J. Dahl, G. E. Trahey, and S. W. Smith, "Phase-aberration correction with a 3-d ultrasound scanner: Feasibility study," *ieee transactions on ultrasonics, ferroelectrics, and frequency control*, vol. 53, no. 8, pp. 1432–1439, 2006.
- [12] F. Vignon, J. Aubry, M. Tanter, A. Margoum, and M. Fink, "Adaptive focusing for transcranial ultrasound imaging using dual arrays," *The Journal of the Acoustical Society of America*, vol. 120, no. 5, pp. 2737–2745, 2006.
- [13] B. D. Lindsey and S. W. Smith, "Pitch-catch phase aberration correction of multiple isoplanatic patches for 3-d transcranial ultrasound imaging," *IEEE transactions on ultrasonics, ferroelectrics, and frequency control*, vol. 60, no. 3, pp. 463–480, 2013.
- [14] G. Clement, P. White, and K. Hynynen, "Enhanced ultrasound transmission through the human skull using shear mode conversion," *The Journal of the Acoustical Society of America*, vol. 115, no. 3, pp. 1356–1364, 2004.
- [15] A. Yousefi, D. E. Goertz, and K. Hynynen, "Transcranial shear-mode ultrasound: assessment of imaging performance and excitation techniques," *IEEE transactions on medical imaging*, vol. 28, no. 5, pp. 763–774, 2009.
- [16] M. Fink, "Time reversal of ultrasonic fields. i. basic principles," *IEEE transactions on ultrasonics, ferroelectrics, and frequency control*, vol. 39, no. 5, pp. 555–566, 1992.
- [17] F. Wu, J.-L. Thomas, and M. Fink, "Time reversal of ultrasonic fields. ii. experimental results," *IEEE transactions on ultrasonics, ferroelectrics, and frequency control*, vol. 39, no. 5, pp. 567–578, 1992.

- [18] D. Cassereau and M. Fink, “Time-reversal of ultrasonic fields. iii. theory of the closed time-reversal cavity,” *IEEE transactions on ultrasonics, ferroelectrics, and frequency control*, vol. 39, no. 5, pp. 579–592, 1992.
- [19] K. J. Haworth, J. B. Fowlkes, P. L. Carson, and O. D. Kripfgans, “Towards aberration correction of transcranial ultrasound using acoustic droplet vaporization,” *Ultrasound in medicine & biology*, vol. 34, no. 3, pp. 435–445, 2008.
- [20] K. Shapoori, E. Malyarenko, R. G. Maev, J. Sadler, E. Maeva, and F. Severin, “2d noninvasive acoustical image reconstruction of a static object through a simulated human skull bone,” in *2009 IEEE International Ultrasonics Symposium*, pp. 2279–2283, IEEE, 2009.
- [21] J. Sadler, K. Shapoori, E. Malyarenko, F. Severin, and R. G. Maev, “Locating an acoustic point source scattered by a skull phantom via time reversal matched filtering,” *The Journal of the Acoustical Society of America*, vol. 128, no. 4, pp. 1812–1822, 2010.
- [22] K. Shapoori, J. Sadler, E. Malyarenko, F. Severin, E. Boni, A. Ramalli, P. Tortoli, and R. G. Maev, “Adaptive beamforming for ultrasonic phased array focusing through layered structures,” in *2010 IEEE International Ultrasonics Symposium*, pp. 1821–1824, IEEE, 2010.
- [23] J. Sadler, K. Shapoori, E. Malyarenko, A. DiCarlo, J. Dech, F. Severin, and R. G. Maev, “Resolving the location of acoustic point sources scattered due to the presence of a skull phantom,” in *Acoustical Imaging*, pp. 271–278, Springer, 2011.
- [24] K. Shapoori, J. Sadler, A. Wydra, E. Malyarenko, A. Sinclair, and R. G. Maev, “Transmission mode adaptive beamforming for planar phased arrays and its application to 3d ultrasonic transcranial imaging,” in *SPIE Medical*

- Imaging*, pp. 86750P–86750P, International Society for Optics and Photonics, 2013.
- [25] K. Shapoori, J. Sadler, A. Wydra, E. V. Malyarenko, A. N. Sinclair, and R. G. Maev, “An ultrasonic-adaptive beamforming method and its application for trans-skull imaging of certain types of head injuries; part i: Transmission mode,” *IEEE Transactions on Biomedical Engineering*, vol. 62, no. 5, pp. 1253–1264, 2015.
- [26] R. Mirzania, K. Shapoori, E. Malyarenko, and R. G. Maev, “Ultrasonic imaging of static objects through an aberrating layer using harmonic phase conjugation approach,” *Ultrasonics*, vol. 58, pp. 11–21, 2015.
- [27] K. Shapoori, *Transcranial Adaptive Beamforming via Ultrasonic Phased Arrays and its Application to 3D Imaging of Certain Types of Head Injuries*. PhD thesis, University of Toronto, 2014.
- [28] C. Yu, C. Zhang, and L. Xie, “A blind deconvolution approach to ultrasound imaging,” *IEEE transactions on ultrasonics, ferroelectrics, and frequency control*, vol. 59, no. 2, pp. 271–280, 2012.
- [29] B. W. Drinkwater and P. D. Wilcox, “Ultrasonic arrays for non-destructive evaluation: A review,” *Ndt & E International*, vol. 39, no. 7, pp. 525–541, 2006.
- [30] E. E. Hundt and E. A. Trautenberg, “Digital processing of ultrasonic data by deconvolution,” *IEEE Transactions on Sonics and Ultrasonics*, vol. 27, no. 5, pp. 249–252, 1980.
- [31] W. Vollmann, “Resolution enhancement of ultrasonic b-scan images by deconvolution,” *IEEE Transactions on Sonics and Ultrasonics*, vol. 29, no. 2, pp. 78–82, 1982.

-
- [32] D. Iraca, L. Landini, and L. Verrazzani, "Power spectrum equalization for ultrasonic image restoration," *IEEE transactions on ultrasonics, ferroelectrics, and frequency control*, vol. 36, no. 2, pp. 216–222, 1989.
- [33] J. A. Jensen, J. Mathorne, T. Gravesen, and B. Stage, "Deconvolution of in vivo ultrasound b-mode images," *Ultrasonic Imaging*, vol. 15, no. 2, pp. 122–133, 1993.
- [34] U. R. Abeyratne, A. P. Petropulu, and J. M. Reid, "Higher order spectra based deconvolution of ultrasound images," *IEEE transactions on ultrasonics, ferroelectrics, and frequency control*, vol. 42, no. 6, pp. 1064–1075, 1995.
- [35] T. Taxt, "Restoration of medical ultrasound images using two-dimensional homomorphic deconvolution," *IEEE Transactions on ultrasonics, ferroelectrics, and frequency control*, vol. 42, no. 4, pp. 543–554, 1995.
- [36] O. V. Michailovich and D. Adam, "A novel approach to the 2-d blind deconvolution problem in medical ultrasound," *IEEE transactions on medical imaging*, vol. 24, no. 1, pp. 86–104, 2005.
- [37] M. Cloostermans and J. Thijssen, "A beam corrected estimation of the frequency dependent attenuation of biological tissues from backscattered ultrasound," *Ultrasonic Imaging*, vol. 5, no. 2, pp. 136–147, 1983.
- [38] P. Narayana, J. Ophir, and N. Maklad, "The attenuation of ultrasound in biological fluids," *The Journal of the Acoustical Society of America*, vol. 76, no. 1, pp. 1–4, 1984.
- [39] K. A. Wear, "The effects of frequency-dependent attenuation and dispersion on sound speed measurements: applications in human trabecular bone," *IEEE transactions on ultrasonics, ferroelectrics, and frequency control*, vol. 47, no. 1, pp. 265–273, 2000.

-
- [40] O. Michailovich and A. Tannenbaum, “Blind deconvolution of medical ultrasound images: A parametric inverse filtering approach,” *IEEE Transactions on Image Processing*, vol. 16, no. 12, pp. 3005–3019, 2007.
- [41] B. A. Angelsen, “Ultrasound imaging,” *Waves, signals and signal processing*, vol. 1, 2000.
- [42] P. Campisi and K. Egiazarian, *Blind image deconvolution: theory and applications*. CRC press, 2016.
- [43] A. Antoniou, *Digital signal processing*. McGraw-Hill Toronto, Canada., 2006.
- [44] S. L. Marple Jr, “Digital spectral analysis with applications,” *Englewood Cliffs, NJ, Prentice-Hall, Inc., 1987, 512 p.*, vol. 1, 1987.
- [45] S. M. Kay, “Modern spectral estimation,” *Prentice-Hall*, 1987.
- [46] R. Jirik and T. Taxt, “Two-dimensional blind bayesian deconvolution of medical ultrasound images,” *IEEE transactions on ultrasonics, ferroelectrics, and frequency control*, vol. 55, no. 10, pp. 2140–2153, 2008.
- [47] Z. Huang, J. Zhang, and C. Zhang, “Ultrasound image reconstruction by two-dimensional blind total variation deconvolution,” in *Control and Automation, 2009. ICCA 2009. IEEE International Conference on*, pp. 1801–1806, IEEE, 2009.
- [48] D. S. G. Pollock, R. C. Green, and T. Nguyen, *Handbook of time series analysis, signal processing, and dynamics*. Academic Press, 1999.
- [49] A. V. Oppenheim and R. W. Schaffer, *Discrete-time signal processing*. Pearson Higher Education, 2010.
- [50] J. A. Jensen and S. Leeman, “Nonparametric estimation of ultrasound pulses,” *IEEE Transactions on biomedical engineering*, vol. 41, no. 10, pp. 929–936, 1994.

-
- [51] T. Taxt, “Comparison of cepstrum-based methods for radial blind deconvolution of ultrasound images,” *IEEE transactions on ultrasonics, ferroelectrics, and frequency control*, vol. 44, no. 3, pp. 666–674, 1997.
- [52] T. Taxt and J. Strand, “Two-dimensional noise-robust blind deconvolution of ultrasound images,” *IEEE transactions on ultrasonics, ferroelectrics, and frequency control*, vol. 48, no. 4, pp. 861–866, 2001.
- [53] S. S. Haykin, *Blind deconvolution*. Prentice Hall, 1994.
- [54] J. A. Cadzow, “Blind deconvolution via cumulant extrema,” *IEEE signal processing magazine*, vol. 13, no. 3, pp. 24–42, 1996.
- [55] R. A. Wiggins, “Minimum entropy deconvolution,” *Geoexploration*, vol. 16, no. 1, pp. 21–35, 1978.
- [56] D. Donoho, “On minimum entropy deconvolution,” *Applied time series analysis II*, vol. 1, 1981.
- [57] A. K. Nandi, D. Mämpel, and B. Roscher, “Blind deconvolution of ultrasonic signals in nondestructive testing applications,” *IEEE transactions on signal processing*, vol. 45, no. 5, pp. 1382–1390, 1997.
- [58] J. F. Claerbout, “Parsimonious deconvolution,” 1980.
- [59] D. P. Bertsekas, *Nonlinear programming*. Athena scientific Belmont, 1999.
- [60] A. Wydra and R. G. Maev, “A novel composite material specifically developed for ultrasound bone phantoms: cortical, trabecular and skull,” *Physics in medicine and biology*, vol. 58, no. 22, p. N303, 2013.
- [61] T. L. Szabo, “Time domain wave equations for lossy media obeying a frequency power law,” *The Journal of the Acoustical Society of America*, vol. 96, no. 1, pp. 491–500, 1994.

-
- [62] MATLAB, *version 8.6.0.267246 (R2015b)*. Natick, Massachusetts: The MathWorks Inc., 2010.
- [63] Autodesk, *AutoCAD version 19.1 (2014)*. San Rafael, California: Autodesk, Inc., 2014.
- [64] R. G. Maev, A. P. Wydra, and E. Strumban, “Ultrasound bone phantom material compatible with mri,” May 27 2016. US Patent App. 15/166,404.
- [65] F. Fry and J. Barger, “Acoustical properties of the human skull,” *The Journal of the Acoustical Society of America*, vol. 63, no. 5, pp. 1576–1590, 1978.
- [66] S. Han, J. Rho, J. Medige, and I. Ziv1, “Ultrasound velocity and broadband attenuation over a wide range of bone mineral density,” *Osteoporosis International*, vol. 6, no. 4, pp. 291–296, 1996.
- [67] S. Wang, C. Chang, C. Shih, and M. Teng, “Evaluation of tibial cortical bone by ultrasound velocity in oriental females,” *The British journal of radiology*, vol. 70, no. 839, pp. 1126–1130, 1997.
- [68] R. Lakes, H. S. Yoon, and J. L. Katz, “Ultrasonic wave propagation and attenuation in wet bone,” *Journal of biomedical engineering*, vol. 8, no. 2, pp. 143–148, 1986.
- [69] R. Strelitzki, J. Evans, and A. Clarke, “The influence of porosity and pore size on the ultrasonic properties of bone investigated using a phantom material,” *Osteoporosis international*, vol. 7, no. 4, pp. 370–375, 1997.

Vita Auctoris

NAME: Mariam Luay Y. Al-Ansary

PLACE OF BIRTH: Baghdad, Iraq

YEAR OF BIRTH: 1993

EDUCATION: Vincent Massey Secondary School, Windsor, Ontario
2007-2010

University of Windsor, Windsor, Ontario
2010-2014 B. Sc. Physics

University of Windsor, Windsor, Ontario
2014-2017 M. Sc. Physics